Imaging systems in the Delft Multi-Beam Scanning Electron Microscope 1

Ren, Yan

DOI
10.4233/uuid:e25ff43d-b8ae-4b6c-9bc9-d10768c4ab11

Publication date
2017

Document Version
Final published version

Citation (APA)
Ren, Y. (2017). *Imaging systems in the Delft Multi-Beam Scanning Electron Microscope 1*. [Dissertation (TU Delft), Delft University of Technology]. https://doi.org/10.4233/uuid:e25ff43d-b8ae-4b6c-9bc9-d10768c4ab11

Imaging Systems for the Delft Multi-Beam Scanning Electron Microscope 1

The work in this dissertation was conducted at the Charged Particle Optics Group, Department of Imaging Physics, Faculty of Applied Science, Delft University of Technology

Printed by: ProefschriftMaken | ProefschriftMaken.nl

ISBN：9789462957114

An electronic version of this dissertation is available at

http://repository.tudelft.nl/

Imaging Systems for the Delft Multi-Beam Scanning Electron Microscope 1

Proefschrift

ter verkrijging van de graad van doctor
aan de Technische Universiteit Delft,
op gezag van de Rector Magnificus prof.ir. K.C.A.M. Luyben;
voorzitter van het College voor Promoties,
in het openbaar te verdedigen op
maandag 9 oktober 2017 om 12:30 uur

door

Yan REN
Master of physical electronics
Xi'an Jiaotong University, China
geboren te Qinyang, China

This dissertation has been approved by the promotor:
Prof.dr.ir. P. Kruit

Composition of the doctoral committee:

Rector Magnificus	Chairman
Prof.dr. ir. P. Kruit	Delft University of Technology

Independent members:

Prof.dr. ir. G.C.A.M. Janssen	Delft University of Technology
Prof.dr. ir. W.M.J.M Coene	Delft University of Technology/ASML
Dr. ir. B.N.G. Giepmans	University of Groningen
Dr. ir. Yongfeng Kang	Xi'an Jiaotong University
Dr. ir. C. W. Hagen	Delft University of Technology
Dr. ir. A. F. de Jong	Thermo Fisher Scientific

To my wife Ting, my daughter Niuniu and my parents

Table of Contents

Chapter 1 Introduction

This chapter states the motivation of my research, which is to design imaging systems in the Delft multi-beam scanning electron microscope (MBSEM) 1. The history of scanning electron microscopy is reviewed firstly, and then possible solutions to achieve high-throughput imaging are discussed. Later, the Delft MBSEM1 is briefly introduced. Its working principle and experimental results are summarized. Additionally, often-used imaging signals in scanning electron microscopy are evaluated. The scope of this dissertation is presented in the end.

1.1 Development of scanning electron microscopy

In scanning electron microscopy, a focused electron beam is scanned across a specimen surface. Various signals generated by the interaction of the incident electrons and the specimen provide the specimen's information, such as topography, chemical composition, and crystalline structure. Scanning electron microscopy has gradually become one of the most powerful tools in material research and life science research.

M. von Ardenne pioneered scanning electron microscopy in 1938. He built a scanning transmission electron microscope (STEM) by adding scanning coils to a transmission electron microscope (TEM). Zworykin *et al.* developed the first scanning electron microscope (SEM) with a resolution of about 50 nm in 1942 for examining a specimen surface. Since then, many techniques and improvements have been introduced to the development of scanning electron microscopy, such as the improved signal processing, a stigmator by K. C. Smith, and a new type of secondary electron detector (a scintillator with photomultiplier tube) created by Everhart and Thornley in 1960. In 1965, Cambridge Scientific Instruments combined all these improvements and released the first commercial SEM —a Mark I ''Stereoscan'', which delivered 6 nm resolution[1]. Nowadays, the architecture of even the latest models of SEMs is not far different from the architecture of the first SEM, but the resolutions of these systems are improved remarkably. For example, FEI's Verios SEM is claimed to have 0.6 nm resolution at 30 keV landing energy.

1.2 Resolution in a SEM

The resolution has been one of the most important properties to characterize the quality of a SEM. The reason to develop SEMs, or electron microscopes (EM) in general, is that scientists tried to achieve a resolution which was better than the best resolution in light microscopy (LM). They found that the resolving power of LM was not only limited by the quality of lenses but also by the wavelength of light used. An electron, when treated as a wave, has a much smaller wavelength. For example, an electron with an energy of 30 keV has a wavelength of 0.04 nm. Such short wavelength makes electrons very promising to achieve nanometer level resolution.

However, when a 30 keV electron beam is used in a Verios type SEM, the resolution is 0.6 nm, not 0.04 nm or even smaller. The discrepancy is due to the aberrations generated by the lenses in the electron optical system. In an electron optical system, the spot size of an electron beam d_p consists of the geometrical spot size d_g, the spherical aberration d_s, the chromatic aberration d_c, and the diffraction error d_d. Their FW50 (Full Width containing 50% of the current) values are expressed using the following formulas[2]:

$$d_g = Md_v \qquad (1.1)$$

$$d_s = 0.18C_s\alpha^3 \qquad (1.2)$$

$$d_c = 0.6C_c\frac{\Delta E}{E}\alpha \qquad (1.3)$$

$$d_d = 0.54\frac{\lambda}{\alpha} \qquad (1.4)$$

$$d_p = \left\{\left[d_g^{1.3} + \left(d_s^4 + d_d^4\right)^{1.3/4}\right]^{2/1.3} + d_c^2\right\}^{1/2} \qquad (1.5)$$

where M, C_s and C_c are the magnification, the spherical aberration coefficient, and the chromatic aberration coefficient of an electron optical system; d_v is the virtual size of the electron source; α is the opening angle in the image plane; E is the landing energy, and ΔE is the FW50 value of the energy spread in the electron source.

The beam current is calculated by:

$$I = B_r \pi^2 \frac{d_g^{\ 2}}{4} \alpha^2 V \qquad (1.6)$$

in which V is the electron beam potential; B_r is the reduced brightness and an intrinsic property of the electron source. B_r is a constant and not affected by the energy change of the electron beam in a SEM column.

In a SEM, a small opening angle of an electron beam makes the spherical aberration and the chromatic aberration small but results in a large diffraction error. There is an optimum opening angle to balance the aberrations and the diffraction for the best resolution. So, once the smallest resolution in a SEM is achieved, the opening angle is fixed, and so is the beam current. For example, the electron beam has 37 pA when it has the smallest probe size of 1.1 nm, as shown in FIG 1. 1.

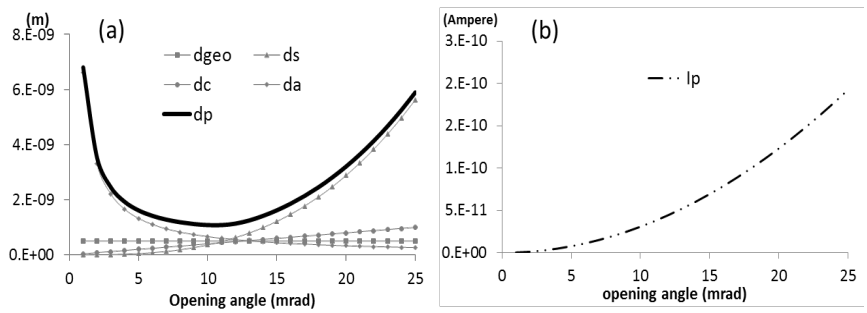

FIG 1. 1 Plot (a) and (b) show a typical SEM probe size composition. In the plots, d_g is 0.5 nm; C_s and C_c are 2 mm; Beam energy is 10 keV; B_r is 5×10^7 A/(m^{2}srV). The electron beam has 37 pA current when it has the smallest probe size 1.1nm.

There are two main approaches to reducing the probe size. The first is to reduce the coefficients of the aberrations, for instance, by optimizing lens design and developing aberration correction devices. Once the C_s and/or C_c are reduced, the probe size becomes small, and the beam current increases due to the increase of the optimum opening angle. However, it is hard to have zero spherical aberration and chromatic aberration. Let us have a look at the C_s correction. Its working principle is to create negative spherical aberration coefficients using multi-pole lenses to neutralize the positive spherical aberration coefficients generated in the rotationally symmetrical lenses. [3-7] A few SEMs are installed with such devices to

improve their imaging resolutions. The C_s discussed here is the third order aberration coefficient. Most of the aberration correctors are designed to reduce the third order aberration contribution. When the opening angle is small, the higher order aberrations contribute little and can be neglected. Once the opening angle becomes sufficiently large due to the aberration correctors, these higher order aberrations come into play too.

The second approach is to lower the energy spread of the electron source ΔE. A monochromator is developed to reduce ΔE, mostly used when the chromatic aberration dominates in the probe size. In the monochromator, electrons with different energies are separate, and a slit is used to select electrons with the desired energy and block the others.[8-10] In this process B_r is reduced, which leads to a smaller current in the probe.

1.3 Throughput

The throughput is the bottleneck of electron microscopy. Here we briefly explain the reason by taking scanning electron microscopy as an example. In a SEM, when an electron beam is used to image samples or to write patterns in lithography and electron beam induced deposition (EBID), sufficient incident electrons are required for decent signal to noise ratio (SNR) in images or to meet the dose requirement in writing. Due to the aberrations discussed previously, a SEM is not able to deliver an electron beam with high current and high resolution simultaneously. When high resolution is required in certain applications, low beam current needs a long scan dwell time to deliver sufficient electrons, resulting in a low throughput.

The low throughput of electron microscopy is not a big issue when the region of interest in a sample is small. However, it turns to be a serious problem in many fields that require high throughput imaging, especially in biological research and wafer industry. In biological research, biologists want to know every connection inside the tissue to understand how life works. Such imaging is very time-consuming. For example, Frank G.A. Faas and his colleagues in Leiden University Medical Center imaged a slide of a complete zebrafish sagittal section in a TEM at 1.6 nm pixel resolution over an area of 1.5 × 0.6 mm, yielding a net total of

281 Giga-pixel. The data collection took 4.5 days[11]. Acquiring a three-dimensional (3D) image takes a longer time. For 3D structure reconstruction, the biological sample is sliced to thin pieces whose thickness can be 30-40 nm. Table 1. 1 evaluates the total time using three EM technologies to image a size of a mouse cortical column 400 × 400 × 1000 μm. It takes at least 500 days to finish the imaging using an SEM[12].

Table 1. 1 Comparison of three technologies to image mouse cortical with 400 × 400 × 1000 μm volume.[12] These three EM technologies, ssTEMCA, SBEM, and ATUM-SEM are abbreviated for serial section transmission electron microscopy (images recorded by CCD camera array), serial block-face scanning electron microscopy and automated tape-collecting ultra-microtome scanning electron microscopy, respectively.

for 0.4mm x 0.4mm x 1mm volume	ssTEMCA	SBEM	ATUM-SEM
Typical x and y resolution (nm)	4	10	4
Typical z resolution (nm)	40	25	30
Dataset size (Gbytes)	250000	64000	333333
Total time (days)	317	818	505

If the throughput of a SEM can be increased a few hundred times, 200 times, for instance, 500 days' work will be done in 2.5 days. High throughput of a SEM will greatly accelerate the biological research, and even change the way of doing research of the biologists.

In wafer industry, scanning electron technology is much more often used than transmission electron microscopy. An electron beam is used in lithography (not in the mass production line), and in measuring critical dimension size and inspecting defects. When a 12-inches wafer is imaged with 10 nm resolution and 100 ns scanning dwell time (almost the shortest dwell time in a SEM), it takes 20,000 hours, which is unacceptable in the industry. The example roughly explains why the electron beam is not used in the mass production line. To finish a wafer in one hour, the throughput of a SEM needs to increase 20,000 times. Mapper is now developing a multi-beam tool that contains more than 500,000 electron beams for lithography.

This thesis focuses on the improvement of throughput in a SEM. Clearly, in these two applications, the throughput of a SEM matters. To increase

the throughput is one of the most important research subjects in electron optics. An aberration corrector is not a good candidate to fulfill this task. As discussed earlier, it helps to improve resolution, but not increase the beam current dramatically by using a large opening angle considering the higher order aberrations. There are three approaches to increasing the throughput of scanning electron microscopy dramatically. The first one is to use many SEMs. It is easy-thinking and doable, but too expensive. Few researchers can afford the cost of 200 SEMs and SEM operation staff.

The second approach is to develop a new type of electron source with much higher B_r so that the electron beam's current can be increased while the beam's opening angle and landing energy are kept the same, demonstrated in equation 1.6. Let us take a brief review of the development of electron source. Tungsten source is the first and most widespread source because it requires low vacuum (10^{-5} Pa) and is relatively inexpensive. Later, a field emission source is developed with better brightness, longer lifetime, and smaller energy spread, but requires high vacuum (better than 10^{-7} Pa) and a strong electrical field near the emission tip.[13] There are two types of field emission: cold field emission and Schottky field emission. A Field emission source provides higher brightness, a smaller virtual size, and lower energy spread than Tungsten and LaB_6 sources do. The field emission source makes it possible to achieve 1 nm resolution with landing energies from 1 keV to 30 keV in commercial SEMs. However, in the recent 20 years, the field emission source is improved quite slowly. It is unlikely to increase the brightness of field emission source a few hundred times in a few years.

Table 1. 2 Comparison of the performance of the widely used electron sources.[14]

Source	Reduced Brightness (A/(m^{2}srV))	Lifetime (hour)	Virtual source size	Energy spread ΔE (eV)	Beam current stability (%/hour)
Tungsten	5×10^4	40-100	30-100μm	1-3	1
LaB_6	5×10^5	200-1000	5-50μm	1-2	1
Schottky field emission	5×10^7	>1000	10-30nm	0.3-1.0	~1
Cold field emission	5×10^8	>1000	<5nm	0.3	2

Carbon nanotube (CNT) emission is a relatively new technology, regarded as a promising candidate to deliver much higher brightness. It is expected to have ten times higher brightness than Schottky field emission.[15] In N. de Jonge and coworker's experiment, they even measured almost 100 times larger brightness.[16] However, its poor stability makes it impossible to be used in the commercial SEMs in the current stage.

The third approach is to develop multiple beams technology. If a few hundreds of electrons beams work simultaneously in one SEM and each beam has the current and probe size comparable to the beam in single beam SEM, the throughput of a SEM should be increased a few hundreds of times.

There are different types of multiple beam systems: multi-source and multi-column system,[17-19] multi-source and single column system,[20-22] single source and multi-column system,[23,24] single source and single column system[25-27].In the multi-source and multi-column system, each beam has its own emitter and column. The pitch of the beams is not smaller than the size of the column. The beams are independent from each other and there are no Coulomb interactions or crosstalk between the beams. However, it is difficult to scale up the number of beams or scale down with the technology node because of the physical size of each column. The pitch of the beams on the sample is about 25mm[17-19], and the throughput is limited. Additionally it is difficult to ensure the quality of each column.

In the multi-source and single column system, multiple beams are focused on the sample separately in one column. The beam's pitch on the sample can be small, in the order of a few μm if wanted. The Coulomb interaction and off axis aberrations come to play in this system. The most important challenge is to fabricate an emitter array with high brightness, low energy spread, good stability and long lifetime. So far few such emitter-arrays have been successfully made.

In the single source and single column system, only one emitter is used. One beam is split into multiple beams by an aperture array. This system exploits the source more efficiently than a single beam system. The

column needs to be designed carefully to control the off axis aberrations, Coulomb interactions and the crosstalk. This system is the most used in the development of multi-beam scanning electron microscopy. The disadvantage is the limitation of the total current caused by the Coulomb interactions.

In the single source and multi-column design, the emitter is still efficiently exploited. Each beam has its own column after the emission unit. It is possible to implement individual control of each beam-let. However the pitch of the beam on the sample cannot be as small as a few μm. The crosstalk may need attention. The electronics and control of this system is more complicated than in the single column design, but the detection of the signals may be easier.

Depending on the specific application, one of these four is chosen. For biological research, a few hundreds of beams are sufficient, but they need to be close together, so option (c) of FIG 1.2 is a logical choice. In wafer industry, it is necessary to have an enormous amount of electron beams to achieve at least one wafer per hour throughput, but the 'specimen' is large enough to allow configuration (d) of FIG 1.2.

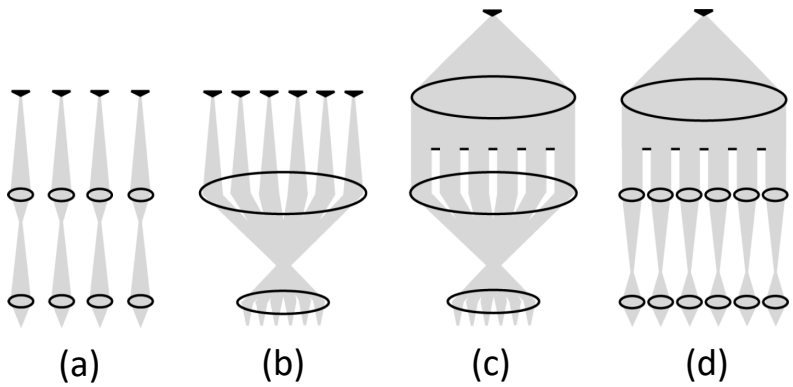

FIG 1. 2 Schematics of 4 multi-beam systems: (a) multi-source and multi-column system, (b) multi-source and single column system, (c) single source and single column system, and (d) single source and multi-column system.

1.4 The MBSEM in Delft

A MBSEM with 196 beams is built in TU Delft based on the revision of FEI Nova Nano 200 SEM.[28] It is a single source and single column

system. As there are several multibeam projects in our group, so this MBSEM is called the Delft MBSEM1.

In the Delft MBSEM1, a multi-beam source unit (MBS) that generates an array of 14 × 14 beams replaces the standard emission source in a Nova Nano 200 type SEM. In the MBS, the electron beam generated from a Schottky emitter is split into an array (14 × 14) of focused beams by the aperture lens array (ALA) which is a thin Si membrane that has an aperture array with 25 μm pitch, each aperture with a diameter of 18 μm. In the image plane of the ALA, the beams have 95 nm geometrical spot size and 70 μm pitch. The focusing effect of the ALA is formed by the electrode 1 (E1), the electrode 2 (E2) and the ALA. The ALA is uniquely designed to correct field curvature, to have a low spherical aberration, to nullify chromatic deflection error, and to avoid highly precise alignment.[28] The image plane of the ALA is positioned in or very close to the object principle plane of the acceleration (ACC) lens to avoid chromatic deflection aberration and to minimize the off-axial aberration of the ACC lens.

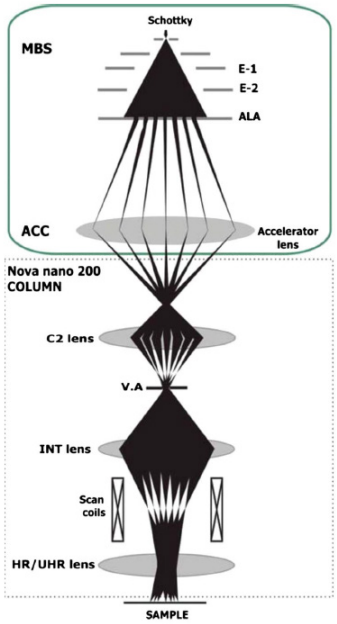

FIG 1. 3 Schematic of the MBSEM developed in Delft.[28] Multi-beam source, electrode 1, electrode 2, aperture lens array, accelerator lens, variable aperture, intermediate lens, high-resolution lens and ultra-high resolution lens are abbreviated as MBS, E-1, E-2, ALA, ACC, INT lens, HR and UHR lens, respectively.

The excitations of lenses in the column are modified to make the beams have good resolution and uniformity on a sample. The combination of the ACC lens, the C2 lens, the intermediate (INT) lens, and the high-resolution (HR)/ ultra-high-resolution (UHR) lens focuses each beam on the sample. Three common crossovers are formed. The first one is optional, sitting between the ACC lens and the C2 lens. The second one is in the plane of variable aperture (VA) that acts as a current limiting aperture. The last is in a so-called coma-free plane of the objective lens to suppress the off-axis aberrations generated by the HR/UHR lens.

The primary beams' pitch on the sample is changeable, following a fixed ratio of geometrical spot size over the pitch, 95 nm/70 μm. For example, if the emission source size is de-magnified to 5 nm, the beams' pitch is 3.7 μm. Besides, the Delft MBSEM1 is capable of correcting field curvature of the off-axis beams. Field curvature is generated because the off-axis beams cannot be focused in the same image plane with the axial beam. The field curvature can be corrected by making the focusing strengths of off-axis aperture lenses weaker gradually in the ALA, with the help of manipulation of the E1 and the E2 electrodes.

There are a few reasons to choose the single source and single column multiple beam system in this prototype. Firstly, the micro-electro-mechanical system (MEMS) technology is very mature to manufacture aperture array. It has no problem to make aperture arrays with decent uniformity and roundness, less than 100 nm error. Additionally, the outgassing property is excellent so that aperture array is capable of working in the emission region where the vacuum requirement is better than 10^{-7} Pa, even when this array suffers continuous electron bombardment. Secondly, the Schottky emission source can be used more efficiently. When a proper voltage is applied to the anode, the angular intensity distribution of the Schottky source has a flat area, which means the electrons emitted from this area have the same B_r in the SEM column, shown in FIG 1. 4. In single beam SEMs, less than 0.1% of current in this area is utilized, which is quite a waste. Multiple beams can be generated in this flat area to use the Schottky source more efficiently. Last, the existing commercial SEM column has electron optical lenses with superb quality for high resolution. Besides, all the control system,

for example, software and electronics, are ready to be used. Utilizing the current column saves an enormous amount of time and energy, but the drawback is the reduced flexibility because of the fixed positions and structures of the lenses.

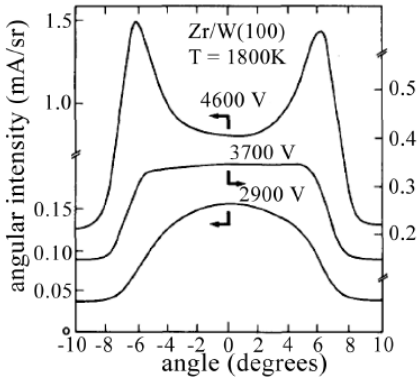

FIG 1. 4 The angular distribution of Schottky emission shows a flat area in the center. [13]

A. Mohammadi-Gheidari and P. Kruit present the electron optics design of the MBSEM system and the simulation result for a specific setting.[28] In the result, each beam has a current of 26 pA; the spot size of the axial beam is 1.2 nm while the 1.5 nm for an outermost beam; the primary beams have 360 nm pitch on the sample with a landing energy of 15 keV. They also present their experimental results using a different lens combination.[29] In their results, the current uniformity of the beams and the total current are in good agreement with the simulated result, shown in FIG 1. 5. The spot sizes of the beams are tested using a self-made sample. It is an aperture with a rod. The aperture is drilled using focused ion beam (FIB) tool, and the rod is built using EBID technology. Unfortunately, as the thin rod is fragile, the spot sizes of all the beams are only proved to be better than 20 nm.

The Delft MBSEM1 can be switched to a single beam mode. In this mode, instead of all the beams having a common crossover in the VA, the beams are separate with a pitch larger than the aperture size so that only one beam can go down to the sample. The single beam mode has better than 2nm imaging resolution and works the same way as in a standard single beam SEM. This mode can be used to get a large field of view (FOV) and to pinpoint the region of interest. Then the multi-beam mode

is switched on for high throughput imaging. The mode switch is simply done by assigning the magnetic lenses different excitations.

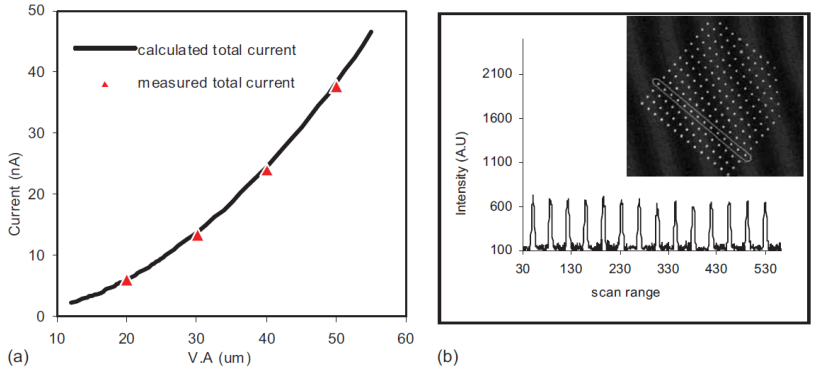

FIG 1. 5 Current measurements in the Delft MBSEM1. (a) shows the total current measurement and (b) shows the proof of uniformity of beams current.[29]

Additionally, this MBSEM is used to deposit a structure with $MeCpPtMe_3$ as a precursor gas on a W/Si_3N_4 membrane.[30] 14 ×14 Pt-containing dots are deposited. Under proper beam control, dots exposed by the beams can be grouped to form continuous lines.

As there were no imaging systems in the Delft MBSEM1 at that moment, the focusing condition of the beams could not be fully guaranteed in the EBID experiment, resulting in the size of the deposited dot about 70nm. Imaging systems for the Delft MBSEM1 are needed to make it more robust.

1.5 Imaging signals in a SEM

Imaging samples is the fundamental reason for developing electron microscopy. Looking back at the development history of scanning electron microscopy, we find that the introduction of the Everhart-Thornley (ET) detector to collect secondary electrons (SE) was a solid reason to commercialize SEMs, because it increased the amount of signal collected and therefor resulted in an improvement in signal to noise ratio. Nowadays, many types of detectors are developed to achieve different imaging quality and information from samples.

SE and backscatter electron (BSE) are widely used as the imaging signals in a SEM. They are so well known to the users of electron microscopy that only a brief introduction is given here.

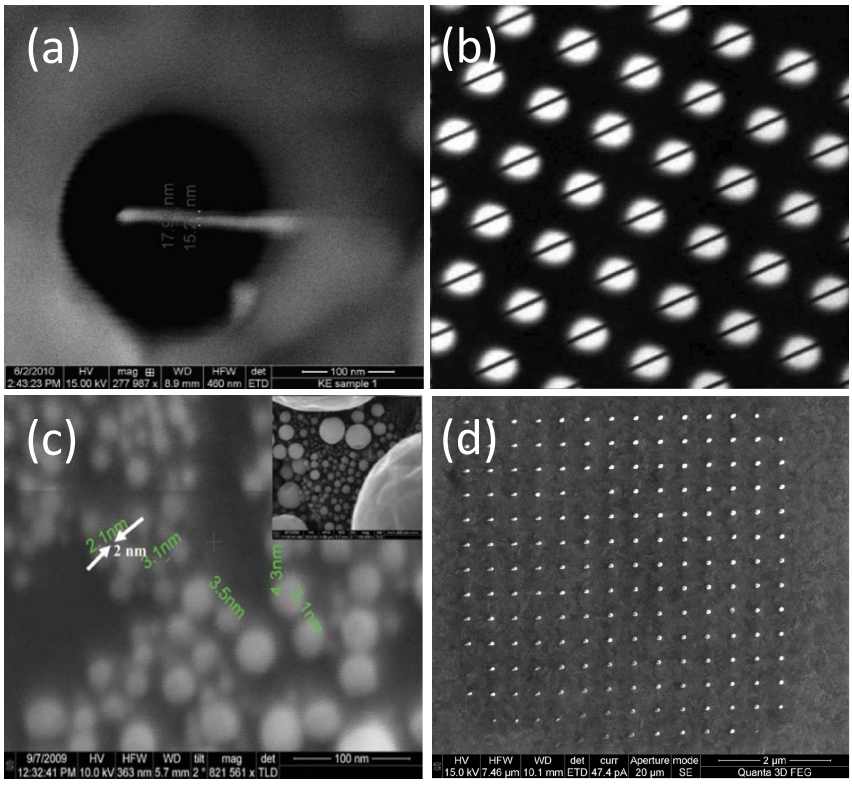

FIG 1. 6 (a) is the testing sample which contains a FIB drilled aperture with a rod. (b) is a transmission image by putting a transmission detector below the testing sample and scanning all beams over this sample in the Delft MBSEM1. (c) shows high resolution (better than 2 nm) image obtained in the single beam mode. (d) is the EBID result using the MBSEM and the precursor $MeCpPtMe_3$.[29,30]

SEs are generated from the surface of the sample. Therefore, the SE signal presents the topography information. The SE energy range is from 0 to 50 eV in conventional definition. It is easy to collect SEs by using a positively biased metal grid positioned near the sample. ET detector employs this structure. The bias voltage is about a few hundred volts, and normally set to be 200 V.[31]

BSEs are reflected or backscattered from the sample because of scattering interactions between the primary beam electrons and the specimen atoms. High atomic number elements bounce back the incident electrons more

strongly than low atomic number elements, thus, appearing brighter in the BSE image. BSE imaging mainly reflects the chemical composition information and this is the reason that biologists often prefer BSE imaging over SE imaging. The BSE energy range is from 50 eV to the primary beam's energy in the conventional definition.[31] So the ET detector cannot efficiently collect BSEs because its electrostatic collection field is too weak to attract electrons with high energies. BSE detectors are mostly mounted concentrically with the optical axis of the SEM column. A semiconductor detector is often used as the BSE detector. Scintillators and channel plates are also the suitable candidates for the BSE detection.

Besides SE and BSE imaging, biologists show more and more interest in transmission electron (TE) imaging in a SEM. The definition of TE is quite straightforward. When the primary electrons hit a thin sample, some electrons pass through the sample. This part of electrons are called transmission electrons. A TE detector is usually placed below the sample. TE detection in a SEM is referred as STEM imaging. TE generation efficiency is proportional to the atoms' scattering power in the sample. So TE imaging also reveals structural and chemical composition information.

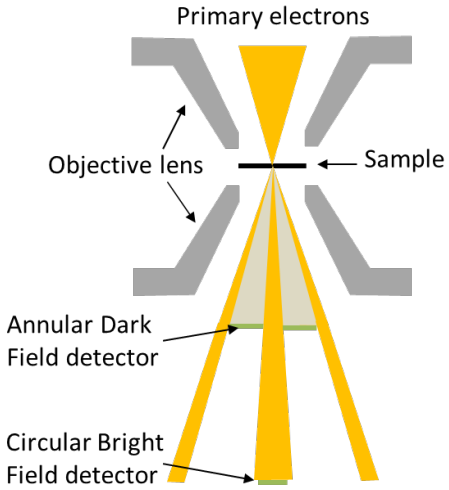

FIG 1. 7 A demonstration of bright field mode and dark field mode in a TEM.

TE imaging concept was implemented firstly in a transmission electron microscope (TEM). A parallel beam of a few hundred keV energy illuminates on a thin sample.[32] A few electron optical lenses are used to focus the TE onto a detector with a large magnification. TEM users can choose between bright field mode and dark field mode, demonstrated in FIG 1. 7. In the bright field mode, non-scattered and weakly scattered TEs are collected to form images. In the dark field mode, the strongly scattered TEs are used to construct images with diffraction contrast. Later on, the STEM concept emerged. It is common to add scanning coils in TEM to have a STEM working mode. In STEM mode, instead of a parallel beam illumination on the sample, a focused beam scans over the sample. The TE signal is collected as usual. The SE signal and BSE signal can also be detected. As the beam energy is a few hundred keV in a TEM or STEM while the elements in the biological tissue are light, the contrast of the TE imaging is poor. One solution to enhance the contrast is to stain the tissue with osmium, uranyl and lead. These elements help to improve the imaging contrast artificially but hide some intrinsic information of the tissue.

Relatively low primary beam energy also helps to enhance imaging contrast when the tissue can be sliced thin to allow electrons with low energy to pass. In such a way, the tissue may not be heavily stained and its intrinsic information may be shown clearly. As SEMs work with much lower beam energy than TEMs, so TE imaging is also widely used in SEMs. Today every SEM manufacturer offers a TE detector as optional. Semiconductor detector and scintillators are often employed as TE detectors.

1.6 Challenges of imaging system design in a MBSEM

There are two types of multi-beam systems. One is aiming for lithography. Imaging systems are not needed in a lithography tool. The other is aiming for imaging. Imaging systems are a must in the latter type.

When I started my Ph.D. project, none of MBSEMs of the type “single source single column” had imaging systems. The goal of my Ph.D. research was to design imaging systems for the Delft MBSEM1. Three

imaging systems were planned to be built: for the TE, the SE and the BSE detection, respectively. The universal challenge of the imaging systems design is that the signals from different beam-lets must be separately detected with a certain detection efficiency when the pitch of the beam-lets is small (from a few μm to tens of μm), without deteriorating the resolution of the primary beams. Below I discuss the specific challenges of these three imaging systems when I started my project.

For the TE imaging system, TU Delft was the only group developing it for a MBSEM. The sample for TE imaging needs to be thin. TEs are collected below the sample. In the Delft MBSEM1, the pitch of the primary beams is normally set to be smaller than 5 μm. So the first question to the TE imaging system design was how to enlarge the pitch of TE beams. There were two approaches for doing this. One was to use a set of electromagnetic lenses to focus TEs with a large magnification into a detection plane, so that TE beams would have a relatively large pitch in the detection plane to be separately collected. This principle was also used in TEM imaging. The other approach was to convert electrons to photons using a fluorescent material firstly and then use an optical microscope to magnify the photon beam pitch. Both these two approaches needed to be implemented inside the vacuum. Besides, the primary beams moved on the sample in the scanning. So the TE signals also moved continuously in the detection plane. Then the second question was how to collect TE signals while they were moving. Still two methods could be used. One was to use de-scan system which was synchronized with the deflection system to cancel or minimize the movement of TE signals. The TE signals would be almost still in the detection plane. Then one beam was assigned to one detector. The other was to use CCD/CMOS camera or similar pixelated detectors. In one scan step, one image containing all TE spots was generated. An image processing program was used to read out the intensity of each TE beam. Besides, there were other practical concerns, such as the alignment between the multi-beam system and new added system, the placement of the thin sample, etc.. I needed to analyze all these options and concerns, and finalize the TE imaging system in the Delft MBSEM1.

For the SE imaging system, a few groups were working on it for their own MBSEMs, for example TU Delft, Zeiss[33] and Hitachi[34]. The other

two group's design principle could be found in their patents.[33,34] Different from the TE collection, the SE collection needs to be done above the sample. The principle of SE detection in a MBSEM was to accelerate SE beams and focus them in a detection plane with a large magnification, so that the pitch of SE beams in the detection plane was large. In Zeiss and Hitachi patent, SE beams were deflected to one side of their columns by using a magnetic field or Wien Filter. An additional set of lenses were used for SE beams' focusing, demonstrated in FIG1.8. The whole system would become very complicated. I needed to find another solution which was capable of focusing SE beams with a large magnification into a detection plane, meanwhile keeping the system compact. Additionally, I still needed to find a way to collect SE signals while they were moving in a scan period.

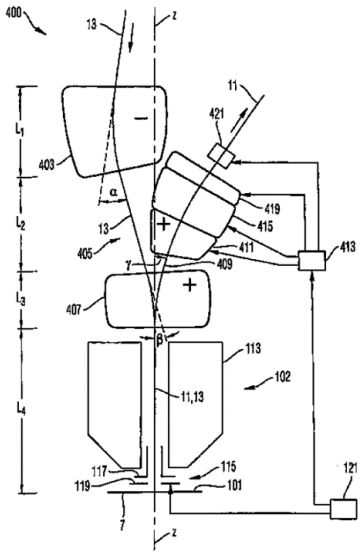

FIG 1. 8 Zeiss' strategy for SE detection in a MBSEM: primary beams and SE beams are separated by using a magnetic field and extra lenses are used to focus SE beams in a detection plane.[33]

BSE imaging system design was not in the scope of my research. Its difficulty can be estimated. In the conventional definition, BSE has an energy range from 50 eV to the primary beam's energy with a full opening angle (from 0° to 90°). Such distribution makes it very hard to separate one beam's BSE signal from its neighbors'. We were struggling to find a good solution. Even now as far as we know, no BSE detection system has yet been successfully developed for a MBSEM.

1.7 Scope of the thesis

This thesis includes the realization of TE imaging system and SE imaging system and is organized as follows.

Chapter 2 discusses the operation flexibility of this MBSEM, including the control of the pitch of the primary beams on the sample, and the control of landing energy.

Chapter 3 focuses on the realization of the TE imaging system. A thin sample is placed on a fluorescent material that converts electrons to photons. Then 196 photon beams are focused with a large magnification onto a camera via a high-quality optical microscope integrated inside the vacuum chamber. An imaging process program retrieves the strengths of 196 beams from the camera images and constructs TE images and image map. Experimental results are reported.

Chapter 4 proposes a strategy for the SE detection system. When the primary beams are focused on the sample, the SE beams are also focused in a detection plane for separate collection. An analytical model is built to prove the possibility. Electron optics simulation and ray tracing results for the SE detection are presented. The flexibility of the Delft MBSEM1 with SE imaging system is discussed.

Chapter 5 describes the experimental setup of the SE imaging system in the Delft MBSEM1. A fluorescent material is used to convert the SEs to photons, and an optical fiber imaging conduit guides the light out of vacuum meanwhile keeping the 196 photon beams separate. An optical system and an image-processing program are used to construct SE images. In the experiment, the SE beams are separated and focused in a detection plane, and the experimental results are presented.

Chapter 6 concludes the achievement of this thesis and proposes an improvement outline.

Finally, all the conclusions are summarized.

While this project was under development, in 2015 Zeiss released a commercially available MBSEM whose type is a single source single column. In its source unit, one beam is split into multiple beams (61 or

91) that are de-magnified using the macro magnetic lenses. The Zeiss MBSEM has a hexagonal arrangement of the beams whose pitch is 12 μm on the sample in the 61 beams system.[35] The hexagonal field of view has a long axis of 108 μm. Its typical landing energies are 1-3 keV, and the range of its pixel sizes is 3-50 nm. The optical resolution is 4.0 nm. The total current is 35 nA and the current of each beam-let is 570 pA. It has a SE imaging system that allows the early customers to develop ways of working with multiple beams, to find more applications, and to give feedback on the benefits and shortcoming of the first generation MBSEM. The SE beams are imaged onto a detector array with one detection unit for each electron beam. A magnetic beam splitter separates the primary beams and the SE beams. The images acquired by the Zeiss MBSEM show sufficient contrast in all sub-images and the resolution of all sub-images only varies a few percent. The crosstalk between adjacent beams is below 1%.[36] The design principle of these two MBSEMs is compared in the thesis, but not the experimental results, such as the imaging resolution and the detection efficiency. The imaging systems in the Delft MBSEM1 are still in the beginning development phase, and many factors can be optimized to improve the imaging properties. It is not the right timing to include the comparison of the imaging properties in this thesis.

1.8 References

[1]A. Bogner, P. H. Jouneau, G. Thollet, D. Basset and C. Gauthier. Micron **38**, 390 (2007).

[2]M. S. Bronsgeest, J. E. Barth, L. W. Swanson and P. Kruit. J Vac Sci Technol B **26**, 949 (2008).

[3]J. Zach and M. Haider. Nuclear Instruments and Methods in Physics Research Section A: Accelerators, Spectrometers, Detectors and Associated Equipment **363**, 316 (1995).

[4]P. W. Hawkes. Ultramicroscopy **156**, A1 (2015).

[5]T. Kawasaki, T. Nakano and K. Hirose. Microelectronic Engineering **86**, 1017 (2009).

[6]R. H. van Aken, C. W. Hagen, J. E. Barth and P. Kruit. Ultramicroscopy **93**, 321 (2002).

[7]H. H. Rose. Science and Technology of Advanced Materials **9**, 014107 (2008).

[8]A. Stamatovic and G. J. Schulz. Review of Scientific Instruments **41**, 423 (1970).

[9]A. Huber, J. Bärtle and E. Plies. Nuclear Instruments and Methods in Physics Research Section A: Accelerators, Spectrometers, Detectors and Associated Equipment **519**, 320 (2004).

[10]A. Henstra, J. Chmelik, T. Dingle, A. Mangnus and G. v. Veen. Microsc Microanal **15**, 168.

[11]F. G. Faas, M. C. Avramut, B. M. van den Berg, A. M. Mommaas, A. J. Koster and R. B. Ravelli. J Cell Biol **198**, 457 (2012).

[12]K. L. Briggman and D. D. Bock. Curr Opin Neurobiol **22**, 154 (2012).

[13]J. Orloff, *Handbook of charged particle optics* (CRC Press, 1997).

[14]J. Goldstein, Newbury, D.E., Joy, D.C., Lyman, C.E., Echlin, P., Lifshin, E., Sawyer, L., Michael, J.R., *Scanning Electron Microscopy and X-ray Microanalysis* (Springer US, 2003).

[15]P. Kruit, M. Bezuijen and J. E. Barth. Journal of Applied Physics **99**, 024315 (2006).

[16]N. de Jonge, Y. Lamy, K. Schoots and T. H. Oosterkamp. Nature **420**, 393 (2002).

[17]T. R. Groves and R. A. Kendall. J Vac Sci Technol B **16**, 3168 (1998).

[18]L. P. Muray, J. P. Spallas, C. Stebler, K. Lee, M. Mankos, Y. Hsu, M. Gmur and T. H. P. Chang. J Vac Sci Technol B **18**, 3099 (2000).

[19]T. Haraguchi, T. Sakazaki, T. Satoh, M. Nakano, S. Hamaguchi, T. Kiuchi, H. Yabara and H. Yasuda. J Vac Sci Technol B **22**, 985 (2004).

[20]E. Yin, A. D. Brodie, F. C. Tsai, G. X. Guo and N. W. Parker. J Vac Sci Technol B **18**, 3126 (2000).

[21]T. Sayaka, S. Yasuhiro, O. Masahide, O. Hiroya, S. Yasunari and S. Norio. Japanese Journal of Applied Physics **42**, 6672 (2003).

[22]S. T. Coyle, B. Shamoun, M. Yu, J. Maldonado, T. Thomas, D. Holmgren, X. Chen, M. R. Scheinfein, B. DeVore and M. Gesley. J Vac Sci Technol B **22**, 501 (2004).

[23]O. Kamimura, S. Tanimoto, H. Ohta, Y. Nakayama, M. Sakakibara, Y. Sohda, M. Muraki, S. Gotoh, M. Hosoda, Y. Someda, K. Tamamori, F. Hirose, K. Nagae, K. Kato and M. Okunuki. Journal of vacuum sciences technology B **25**, 140 (2007).

[24]M. J. Wieland, G. de Boer, G. F. ten Berge, M. van Kervinck, R. Jager, J. J. M. Peijster, E. Slot, S. W. H. K. Steenbrink, T. F. Teepen and B. J. Kampherbeek. 76370F.

[25]Y. Zhang and P. Kruit. Journal of Vacuum Science & Technology B: Microelectronics and Nanometer Structures **25**, 2239 (2007).

[26]M. Enyama, M. Sakakibara, S. Tanimoto and H. Ohta. Journal of Vacuum Science & Technology B, Nanotechnology and Microelectronics: Materials, Processing, Measurement, and Phenomena **32**, 051801 (2014).

[27]A. L. Eberle, S. Mikula, R. Schalek, J. Lichtman, M. L. K. Tate and D. Zeidler. J Microsc-Oxford **259**, 114 (2015).

[28]A. Mohammadi-Gheidari and P. Kruit. Nucl Instrum Meth A **645**, 60 (2011).

[29]A. Mohammadi-Gheidari, C. W. Hagen and P. Kruit. J Vac Sci Technol B **28**, C6g5 (2010).

[30]P. C. Post, A. Mohammadi-Gheidari, C. W. Hagen and P. Kruit. J Vac Sci Technol B **29**, 06F310 (2011).

[31]L. Reimer, *Scanning electron microscopy : physics of image formation and microanalysis* (Springer, 1998).

[32]L. Reimer, *Transmission electron microscopy : physics of image formation and microanalysis* (Springer, 1997).

[33]R. Knippelmeyer, O. Kienzle, T. Kemen, H. Mueller, S. Uhlemann, M. Haider and A. Casares. Particle-opticle systems and arrangements and particle opticle componenents for such systems and arrangements. (2009).

[34]M. Enyama, H. Ohta and O. Kamimura. Charged particle beam apparatus. (2010).

[35]Product information of the Zeiss MultiSEM 505, version 1. (2015)

[36]A.L. Eberle, S. Mikula, R.Schalek, J.W. Lichtman, M.L.Knothe Tate and D. Zeidler. High-resolution, high-throughput imaging with a multibeam scanning electron microscope. Journal of Microscopy Vol. 00, 1-7(2015)

Chapter 2 Pitch and landing energy control in the Delft MBSEM1

This chapter explores the control of the pitch and the landing energy in the Delft MBSEM1. The control of the pitch is essentially the control of the focusing magnification of the electron optical focus system in the Delft MBSEM1 because the ratio between the geometrical spot size and the pitch is a constant. The entire electron optical focusing system of the Delft MBSEM1 is divided into three parts. The pitch's flexibility introduced by each part is simulated and analyzed. Hundreds of combinations of the electromagnetic lenses in the Delft MBSEM1 are simulated using a landing energy of 15 keV. As different combinations can realize one certain pitch, two ways are introduced to evaluate these combinations. One way is to assess the current and the resolution of the beams, and the other way is to check the uniformity of the beams. The control of the landing energy focuses on the realization of the low landing energy (lower than 15 keV), which is achieved by biasing the sample stage negatively. The pitch control in low landing energy cases is also studied. The limitation of the control in the Delft MBSEM1 is discussed, and a few suggestions for the next generation MBSEM are proposed.

2.1 Introduction

2.1.1 Motivation

Since the Delft MBSEM1 with 196 beams was developed, a few experiments have been done to test its performance[1]. The total current, the uniformity and the resolution of the beams were measured. Additionally, this MBSEM was used to do electron beam induced deposition (EBID)[2]. Most experiments were done using a small pitch (about 0.4μm) of the primary beams on a sample, aiming to obtain a good resolution. However, many applications that need high-throughput have their requirements on the pitch, the resolution, and the landing energy. For example, in EBID experiments, the beams' pitch is preferred to be variable; in wafer industry, a low landing energy and a high beam current are more desired than a fine resolution. In our MBSEM, it is expected that the smaller pitch leads to the better resolution and the larger pitch leads to large beam current. A compromise among the resolution, the

beam current, and the pitch needs to be made for a specific application. So, it is useful and necessary to investigate the flexibility of the pitch and the landing energy of the primary beams in the Delft MBSEM1.

Ali Mohammadi-Gheidari started this investigation. In his doctoral dissertation, he proved the possibility of the pitch control by studying the different combinations of the lenses in the system, and the possibility of the landing energy control by adding a retarding lens between the sample and the magnetic objective lens in the Delft MBSEM1. This chapter is the extension of his work, and to refine the investigation result.

This chapter adds new analysis. Firstly, two practical considerations of this MBSEM are taken into account. The first consideration is the limitation of the acceleration (ACC) lens that is shown in FIG 2. 1. The electrode ACC1 is connected to the aperture lens array (ALA), and set to be 1500 V relative to the Schottky tip potential. The ACC2 is connected to the extractor of the Schottky tip, and set to be 5000 V relative to the tip potential; the Coulomb tube is grounded; the potential of the ACC3 is floating on the ACC1. So the minimum potential for the ACC3 is 1500 V relative to the tip potential. The second consideration is that all the apertures except the variable apertures are moved out of the MBSEM column.

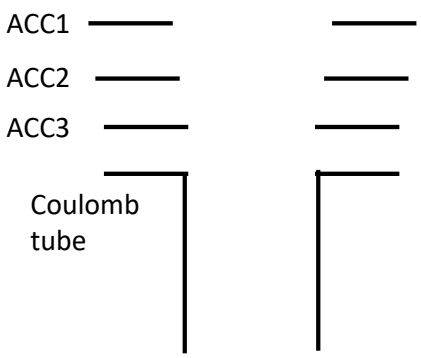

FIG 2. 1 Layout of the acceleration lens with four electrodes: ACC1, ACC2, ACC3 and Coulomb tube.

Secondly, a new index, D/d_{geo}, is introduced to evaluate the optical performance of each combination. D is the beam size. d_{geo} is the geometrical spot size. This index presents the beam formation and reflects the current information. It is possible that in one lens combination

the d_{geo} contributes little to the beam size, resulting in a tiny current in the probe. Such combination should be avoided and can be found easily using this index.

Thirdly, as different combinations are possible to generate the same pitch of the primary beams on the sample in the Delft MBSEM1, their optical performances are compared for understanding the limitation of the Delft MBSEM1.

Last but not least, based on all the analysis mentioned above, a few suggestions are made for the improvement of the next generation MBSEM.

The control of the pitch is discussed in Sec 2.2. The control of the landing energy is studied in Sec 2.3.

2.1.2 Probe composition

In this chapter, all types of spot sizes are evaluated by the FW50 which defines a spot size containing 50% of the total current.[3] The spot size of a beam in the MBSEM can be expressed by

$$D_{total} = \sqrt{{d_{axial}}^2 + {d_{off-axis}}^2} \qquad (2.1)$$

where d_{axial} is the spot size of the axial beam, defined by equation 1.5; $d_{off-axis}$ is the contribution of the total off-axis aberrations, which is calculated by[4]

$$d_{off-axis} = \sqrt{{d_{AS}}^2 + {d_{FC}}^2 + {d_{CO}}^2 + {d_{CM}}^2} \quad (2.2)$$

$$\frac{d_{AS}}{M} = \sqrt{2} h^2 \beta \sqrt{S_a^2 + s_a^2} \qquad (2.3)$$

$$\frac{d_{FC}}{M} = \sqrt{2} h^2 \beta \left| F_a + S_a \right| \qquad (2.4)$$

$$\frac{d_{CO}}{M} = h\beta^2 \sqrt{{C_a}^2 + {c_a}^2} \quad (2.5)$$

$$\frac{d_{CM}}{M} = h \frac{\Delta E_{50}}{E} \sqrt{{C_{Da}}^2 + {C_{\theta a}}^2} \qquad (2.6)$$

in which $d_{AS}, d_{FC}, d_{CO}, d_{CM}$ are the FW50 values of the astigmatism, the field curvature, the coma and the chromatic magnification error of each lens in its object plane. M is the magnification of each lens; h and β are the off-axis distance and opening angle in the object plane of each lens. S_a, s_a, F_a, C_a and c_a are the isotropic-anisotropic third order aberration coefficients of astigmatism, the field curvature, and the coma. C_{Da} and $C_{\theta a}$ are the isotropic-anisotropic first order chromatic aberration coefficients. All these coefficients are in the object plane of each lens. The subscript a means that the coefficients are dependent on the aperture plane, illustrated in FIG 2. 2. When the off-axis distance and the opening angle of a beam in the object plane are given, the position of the aperture plane can be optimized to minimize the contribution of the off-axis aberrations. The coma-free plane of the high resolution (HR)/ultra high resolution (UHR) lens is derived by optimizing the aperture plane position. In this off axis aberration calculation, the distortion is omitted because it does not cause any blur and is possible to be compensated.

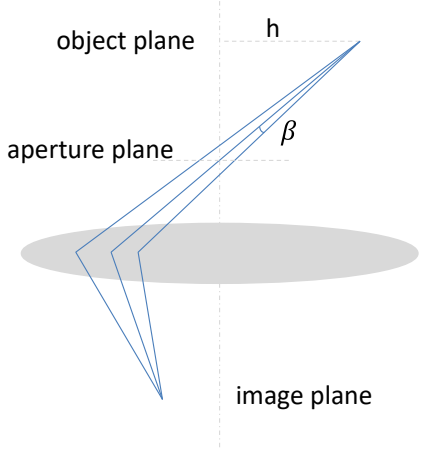

FIG 2. 2 Illustration of the aperture plane in the focusing of the off-axis beam. h and β are the off-axis distance and opening angle in the object side.

Our MBSEM can correct field curvature. When the object planes of the axial beam and the object plane of an off-axis beam coincide, the image plane of the off-axis beam slightly deviates from the image plane of the axial beam. So, the off-axis beam becomes a bit blurred in the image plane of the axial beam, causing the field curvature. For the field curvature correction, the object plane of the off-axis beam needs to be

shifted towards the lens to make its image plane coincide with the axial beam's image plane, demonstrated in FIG 2. 3. In our MBS module, the E1 and the E2 control the focal length distribution of the aperture lenses in the ALA. A proper potential combination of the E1 and the E2 electrodes can make the off-axis aperture lens weaker than the axial aperture lens so that the image planes of the off-axis beam and the axial beam coincide. Then the field curvature can be corrected,[5] demonstrated in FIG 2. 4. In this chapter, two types of spot sizes are listed, D_{total} without the field curvature correction and $D_{total-fc}$ with the correction.

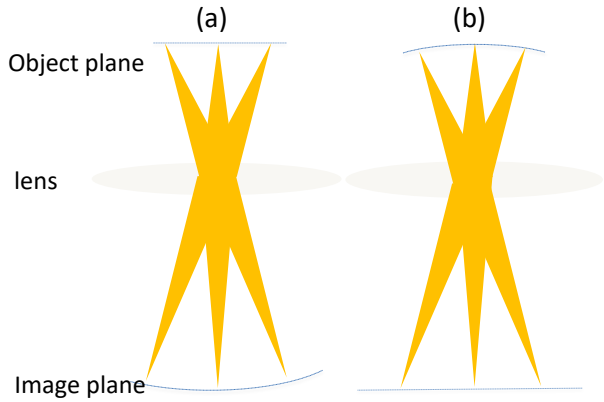

FIG 2. 3 (a) explains the generation of field curvature; (b) gives a solution to correct field curvature by shifting the object positions of the off-axis beams.

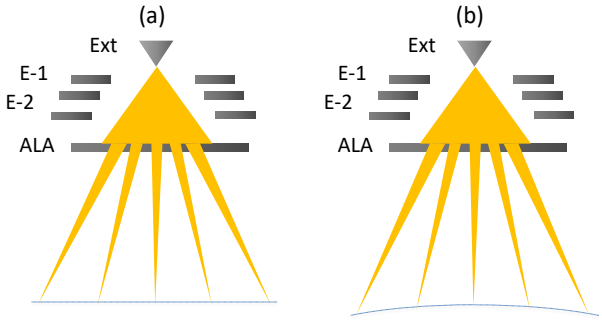

FIG 2. 4 Illustration of the capacity of the MBS module to change the image positions of the aperture lens array.

2.1.3 Method

In the chapter, two beams are simulated. One is the axial beam, which has no off-axis aberration, and the other is an outermost beam, which has the

worst off-axis aberration contribution. The spot size of the axial beam is d_{axial}, and the spot size of the outermost beam is D_{total}, or $D_{total-fc}$.

The control of the pitch is essentially the control of the magnification in the electron optical system in the Delft MBSEM1 because the ratio between the geometrical spot size and the pitch is fixed, 95nm / 70μm. So the total focusing magnification of the combination of the lenses in the Delft MBSEM1 needs to be varied to change pitch.

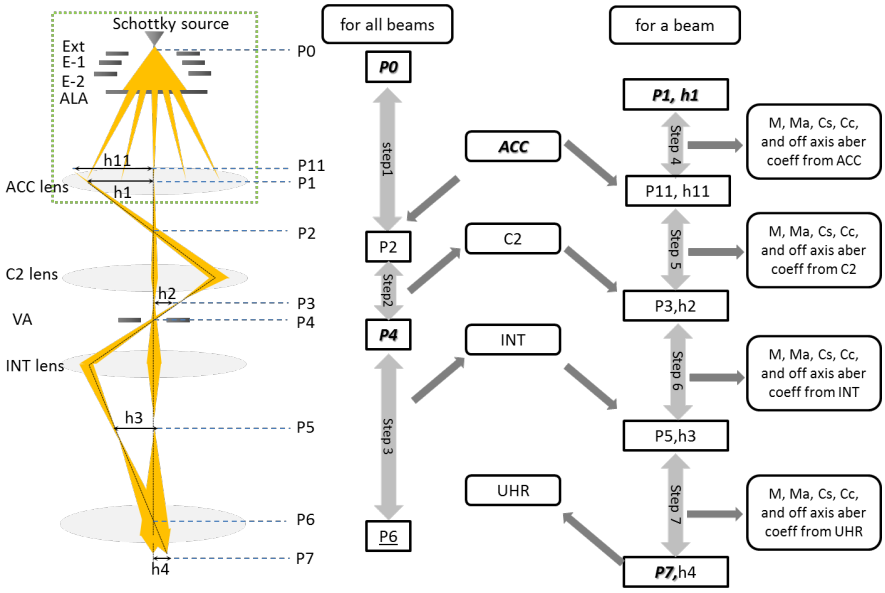

FIG 2. 5 Left is the schematic of the optical system in the Delft MBSEM1 and right is the calculation flow to simulate its optical properties using one combination of all lenses. "P0", "P1", "P4", "P7" and "h1" are input. "ACC," "C2," "INT," "UHR" mean excitations of the ACC lens, the C2 lens, the INT lens and the UHR lens respectively. P6 is determined by P5 and P7, insensitive to P5 and sensitive to P7. The correspondent opening angles in the lenses are optimized by obtaining the smallest spot size of the axial beam on a sample.

Hundreds of combinations of the lenses are simulated using the electron optical design (EOD) program.[6] The simulation flow is demonstrated in FIG 2. 5. In the simulation of each combination, the input is the positions of the emission tip, the image plane of the ALA lens and the VA, the off-axis distance of the off-axis beam in the image plane of the ALA lens, the excitation of the ACC lens and the working distance. Besides, there are a few requirements on the optical system, such as to form common crossovers in the VA plane and the coma-free plane of the objective lens.

Then all the optical properties of each lens can be calculated based on the input and the requirements, such as the magnification, the angular magnification and all types of aberration coefficients. The off-axis distances of the off-axis beam in the lenses are calculated using the magnifications of the lenses. The opening angles in the lenses are optimized to achieve the smallest probe size for the axial beam on the sample.

At least seven focusing subsystems need to be simulated, and more than 70 values are required to be recorded to complete the simulation of one combination. All such operations can only be done manually in the EOD. It takes much effort and time to finish the simulation of one combination. So in this chapter, only hundreds of the combinations are simulated to demonstrate the flexibility of the Delft MBSEM1.

2.2 Pitch control

The electron optical system in the Delft MBSEM1 can be divided into three parts. The lenses above the VA are the first part, including the ACC lens and the C2 lens. The lenses below the VA are the second part, including the intermediate(INT) lens, the HR/UHR lens. The third part is the working distance (WD). The reason for such division is that the primary beams have a common crossover in the VA plane, which is then imaged by the INT lens to the coma-free plane of the HR/UHR lens to reduce the off-axis aberrations. The apertures in the VA are used to select the beams' current. These three parts are analyzed separately. When one part is discussed, the other two have fixed working conditions. Then they are combined to check the pitch control flexibility in the Delft MBSEM1.

2.2.1 Combination of the ACC lens and the C2 lens

In this section, the UHR lens is activated as the objective lens; the WD and the landing energy are set at 5 mm and 15 keV. Such working condition is used widely in scanning electron microscopy for high-resolution imaging.

This combination creates a common crossover in the VA plane. It is optional to have an extra common crossover between the ACC lens and the C2 lens. FIG 2. 6 shows two possible ways to create the common crossover in the VA.

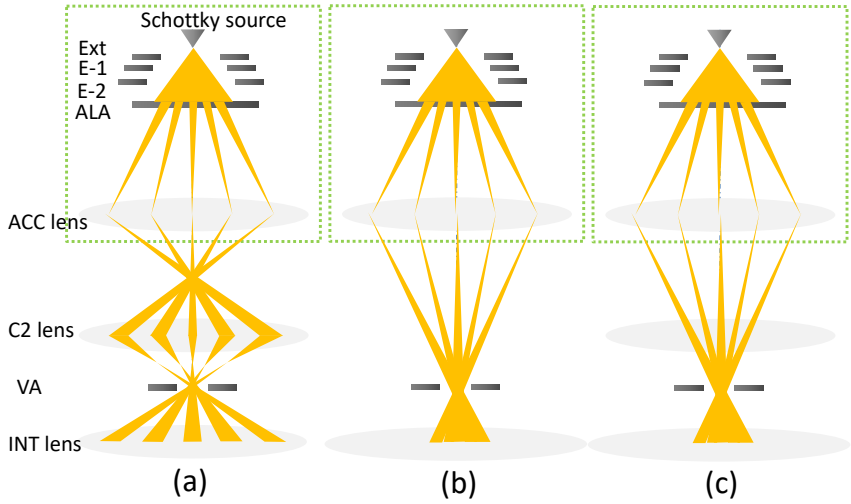

FIG 2. 6 (a) show the case with an extra crossover between the ACC lens and the C2 lens. (b) and (c) show the cases without an extra crossover. (b) shows only the ACC lens activated to form the crossover in the VA plane; (c) shows the combination of the weak ACC lens and the weak C2 lens to form the crossover.

In the ACC lens, the lowest voltage of the ACC3 is 1500 V. When the voltage on the ACC3 is increased to 7500V, the focusing strength of the ACC lens turns weak. When the voltage on the ACC3 is about 5300 V, the ACC lens makes a crossover inside the C2 lens, and this makes the C2 barely possible to generate the crossover in the VA. When the voltage on the ACC3 is 6340.7 V, the ACC lens forms the crossover in the VA without any help from the C2 lens. If the voltage on the ACC3 is larger than 6340.7 V, the C2 lens needs to be turned on to make the crossover in the VA. So when there is the extra crossover, the voltage on the ACC3 is limited from 1500 V to 5300 V. When there is no extra crossover, the voltage on the ACC3 is from 6340.7V to 7500 V.

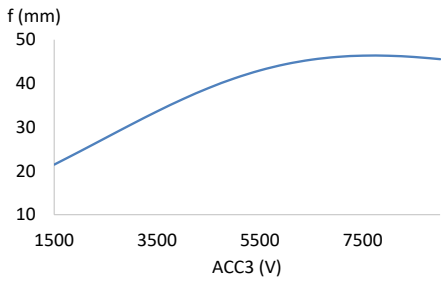

FIG 2. 7 The plot of the focal length of the ACC lens with the change of the ACC3 when the ACC1, the ACC2, and the Coulomb tube are set 1.5 kV, 5 kV, and 15 kV, respectively.

FIG 2. 8 presents the EOD simulation result. The opening angle in each combination is optimized to get the smallest spot size of the axial beam on the sample.

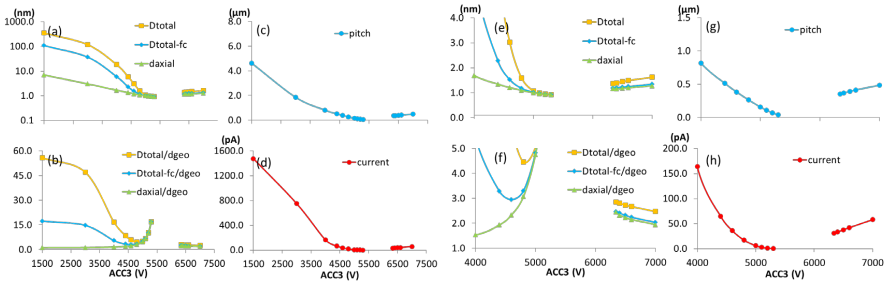

FIG 2. 8 The pitch control using the different combinations of the ACC lens and the C2 lens. The ACC3 varies from 1500V to 7000V in (a)-(d), and varies from 4000V to 7000V in (e)-(h). (a) and (e) give the spot sizes; (b) and (f) plot the ratios of the spot sizes over d_{geo}; (c) and (g) the pitch on the sample, and (d) and (h) the current. Curves are broken because this combination cannot make a crossover in the VA when the ACC3 is from 5300 V to 6340.7V. In each combination, the opening angle is optimized to get the smallest axial beam spot size. The reduced brightness B_r used here is 5×107 A/(m^{2}srV).

When there is the extra crossover, the pitch of the primary beams on the sample changes from 4.6 μm to 0.04 μm. The beam current changes from 1475 pA to 0.4 pA. D_{total} change from 349.7 nm to 0.9 nm. Although this way provides the possibilities to achieve a relatively large pitch or a small spot size, it is not good to be used. When the large pitch is achieved, the uniformity of the beams is poor, and the off-axis aberrations dominate the outermost beam. For example, when the pitch is 4.6 μm (the ACC3 1500 V), d_{axial}/d_{geo} is 1.1 but D_{total}/d_{geo} is 55 and $D_{total-fc}/d_{geo}$ is 17.3. The D_{total} is about 49 times of the d_{axial}. When the small D_{total} is achieved (the ACC3 5300 V), 0.9 nm, the uniformity of the beams is good, d_{axial}/d_{geo} almost equals D_{total}/d_{geo}. However, the geometrical spot size counts too little in the axial spot size: d_{axial}/d_{geo} is 17, resulting in only 0.4 pA current after the optimization of the opening angle. In this combination, the diffraction error and the spherical aberration dominate the spot size of the axial beam. The optical properties of the electron beams in this solution are not favored in the electron optics design.

When there is no extra crossover, the beam's pitch on the sample changes from 0.4 μm to 0.5 μm; the beam current from 30.7 pA to 57.9 pA; D_{total} from 1.4 nm to 1.6 nm. In these combinations, the uniformity of the beams is decent. D_{total} / d_{axial} is not larger than 1.1. The geometrical spot size contributes properly in the beams' spot sizes. D_{total} / d_{geo} is not greater than 2.5.

FIG 2. 9 shows the composition of the outermost beam on the sample, in terms of lenses and aberrations, by listing the ratios of all kinds of spot sizes over the corresponding d_{geo}. In the plots, the voltage on the ACC3 varies from 4400V to 7000V. When the voltage on the ACC3 is from 1500V to 4400V, the off-axis aberrations are too large to be practically useful.

The ACC lens and the INT lens are the two primary contributors to the off-axis aberrations, shown in FIG 2. 9(a). In our MBSEM system, the off-axis distances in the ACC lens and the INT lens are usually the largest. The off-axis distance of the outermost beam in the ACC lens is 0.64 mm. The ACC lens needs to focus each beam as weakly as possible on having the small off-axis aberration coefficients. The ideal condition is to coincide the image plane of the ALA with the object principle plane of the ACC lens so that the ACC lens contributes no focusing effect to the beamlets. When there is any deviation, the ACC lens starts to contribute, and thus the off-axis aberrations from this lens appear.

When there is no crossover between the ACC lens and the C2 lens, the ratio of the off-axis contribution from the ACC lens over d_{geo} is around 0.4. The C2 lens almost contributes nothing. The ratio of the off-axis contribution from the INT lens over d_{geo} is around 1.2. As the strength of the INT lens is determined by the focusing from the VA to the coma-free plane, the off-axis distance in the INT lens and the opening angle of each beam after the optimization need to be reduced to suppress the INT lens' contribution.

The curvature of field is always the largest off-axis aberration. So the field curvature correction can significantly improve the uniformity of the beams.

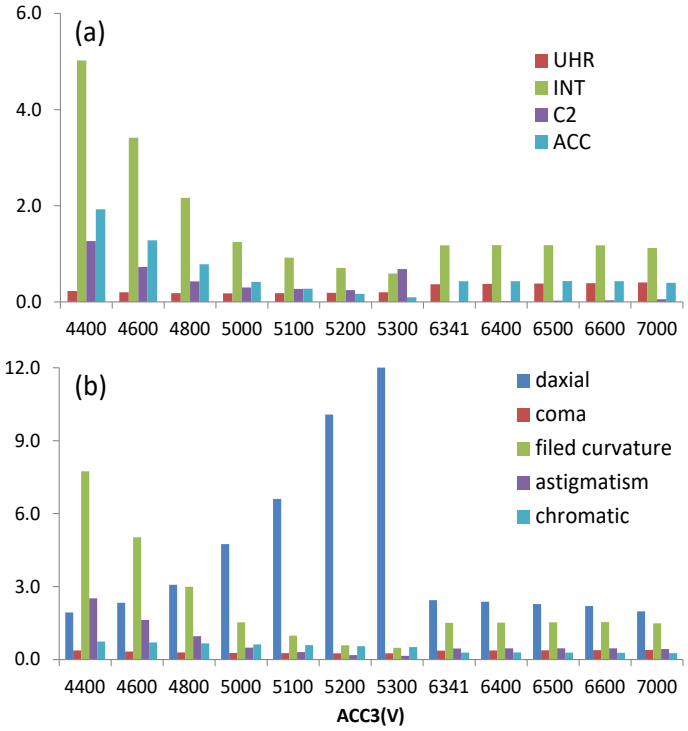

FIG 2. 9 The composition of the outermost beam in the analysis of the different combinations of the ACC lens and the C2 lens, in terms of lenses and aberrations. The plots show the ratios of all the contributors over d_{geo}. (a) presents the off-axis aberrations contributed from the lenses; (b) presents all types of aberrations in total.

To sum up the discussion in this section,

- The extra crossover between the ACC lens and the C2 lens does not benefit the system. It makes either the uniformity of the beams bad when the pitch is large or the current of the beams tiny when the pitch is small.
- In the case of no extra crossover, the off-axis aberrations are well controlled, but the pitch on the sample is limited, from 0.4 µm to 0.5 µm in this configuration of the INT lens and the objective lens.

2.2.2 Combination of the INT lens and the HR/UHR lens

In this section, the analysis is carried out for the ACC3= 7000 V, the LE=15 keV and WD = 5 mm. The reason to choose ACC3 7000 V is that

it gives the best uniformity (D_{total} / d_{geo} is 2.0 and d_{axial} / d_{geo} is 1.9), and the largest pitch (0.5 μm) in section 2.2.1.

In a Nova Nano type SEM, there are two magnetic objective lenses, a high-resolution (HR) lens with enclosed magnetic field, and an ultra-high-resolution (UHR) lens, which is the immersion magnetic lens and sits below the HR lens, illustrated in FIG 2. 10. In the standard Nova Nano SEM operation, each time only one of these two lenses is activated. In the Delft MBSEM1, if only the UHR lens is activated, the estimated magnification is around 0.04 for a typical object distance 120 mm and a working distance 5 mm; if only the HR lens is used, the magnification is about 0.55. The combination of the HR lens and the UHR lens can provide a magnification from 0.04 to 0.55, gaining more flexibility in the pitch control.

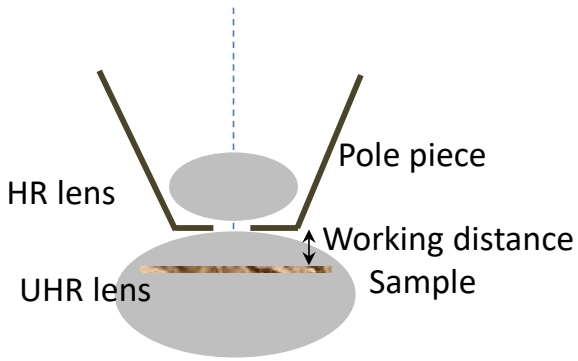

FIG 2. 10 The demonstration of the HR lens and the UHR lens in the Nova Nano SEM column.

As the objective lens is usually the strongest lens in a SEM, the INT lens is required to create a common crossover in the coma-free plane of the objective lens to minimize the off-axis aberration coefficients of the objective lens. For a different HR/UHR combination, the position of the coma-free plane is different, resulting in a different strength of the INT lens.

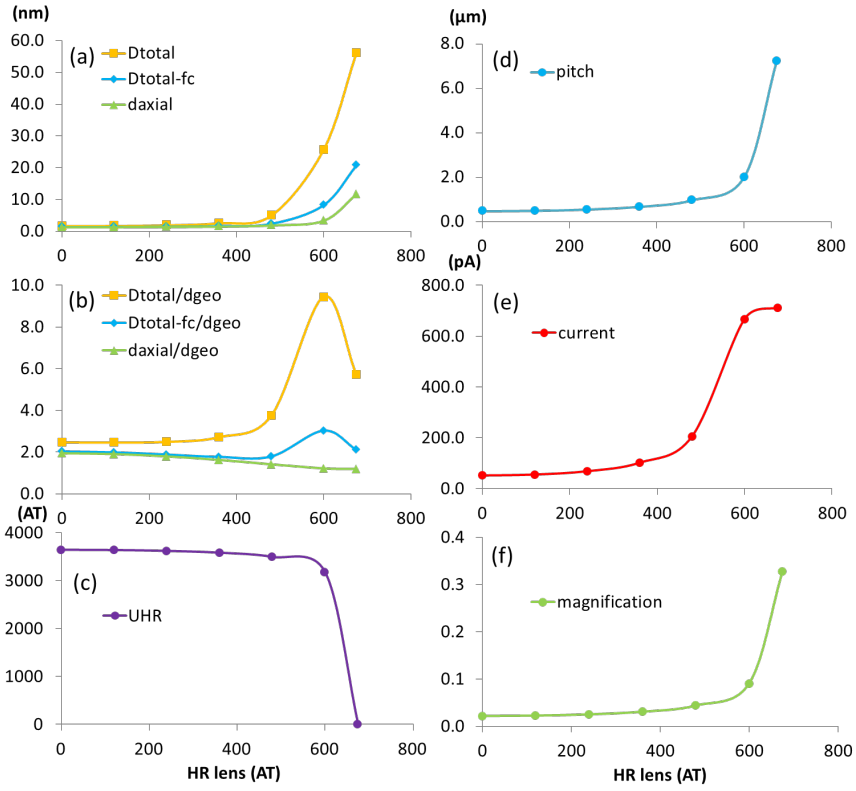

FIG 2. 11 The pitch control using the various combinations of the INT lens and the HR/UHR lens. (a) gives the spot sizes; (b) the ratios of the spot sizes over d_{geo}; (c) the strength of the UHR lens; (d) the pitch on the sample; (e) the current and (f) the focusing magnification of the whole system. In each combination, the opening angle is optimized to get the smallest axial beam spot. The reduced brightness B_r used here is 5×10^7 A/(m²srV).

When the excitation of the HR lens varies from 0 AT (using the pure UHR lens) to 675.08 AT (using the pure HR lens), the pitch grows from 0.5 μm to 7.2 μm, shown in FIG 2. 11. The current increases from 51 pA to 712 pA, and d_{axial}/d_{geo} smoothly drops from 1.9 to 1.2. When the excitation of the HR lens is weaker than 360 AT, D_{total}/d_{geo} and $D_{total-fc}/d_{geo}$ change gently. When the excitation of the HR lens is stronger than 360 AT, D_{total}/d_{geo} and $D_{total-fc}/d_{geo}$ climb to 9.5 and 3.03 (HR 600 AT), and then drop to 5.7 and 2.1 (HR 675.08 AT).

The aberration contribution plots in FIG 2. 12 show that the INT lens usually contributes the most, and its contribution grows along with the

HR lens' strength. The phenomenon can be explained. Firstly, due to the coma-free plane shifting upwards when the HR lens becomes stronger, the INT lens becomes stronger and generates larger off-axis aberrations' coefficients a bit, less than 10% in average from the excitation of the HR 0 AT to 675.08 AT. This reason is minor. Secondly, the optimized opening angle of the beam passing through the INT lens becomes larger when the HR lens becomes stronger in the combination. The second reason is the major contribution. Table 2. 1 lists a few combinations. As mentioned before, the opening angle of the beam on the sample is optimized to achieve the smallest spot size of the axial beam. The opening angle of the beam in the INT lens when the HR lens is 675.08AT is 2.63 times bigger than when the HR lens is 360AT. The second reason also explains the growth of the off-axis aberrations from the ACC even its strength is fixed.

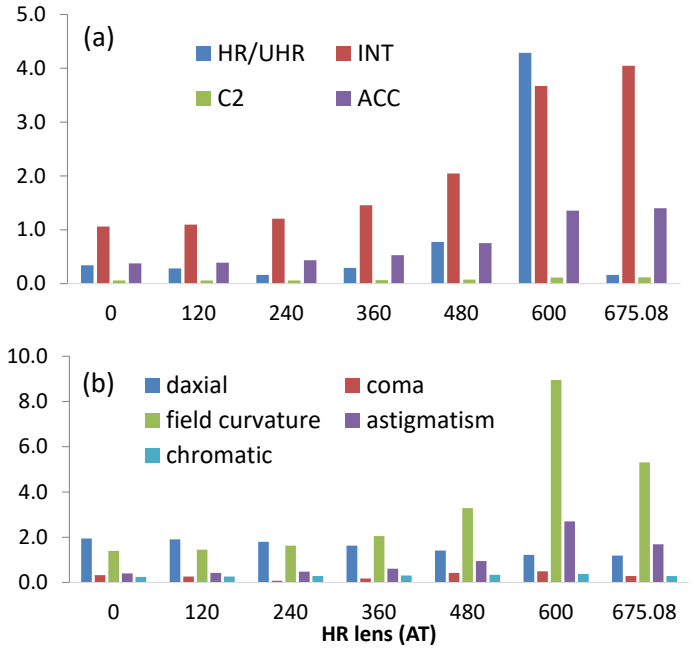

FIG 2. 12 The composition of the outermost beam in the analysis of the different combinations of the INT lens and the HR/UHR lens, in terms of lenses and aberrations. The plots show the ratios of all the contributors over d_{geo}.

Table 2. 1 The properties of the axial beam in the four HR/UHR combinations. Suffix '$-\min$' means data is calculated when the smallest probe size for the axial beam is obtained.

HR lens in the combination	360	480	600	675.08
Properties of HR/UHR:				
Magnification	-0.03	-0.05	-0.10	-0.39
Angular magnification	-28.80	-20.24	-9.81	-2.55
C_s(mm)	5.43	5.38	6.64	547.49
C_c(mm)	3.10	3.34	5.47	55.20
Opening angle in object side (mrad)	**0.30**	**0.42**	**0.71**	**0.79**
Axial beam on the sample:				
C_s(mm)	5.46	5.52	9.09	967.85
C_c(mm)	3.30	3.76	7.23	78.68
$d_{axial\text{-}min}$(nm)	0.9	1.9	3.3	11.7
$I_{axial\text{-}min}$(pA)	101.5	205.4	667.1	711.9
$Alpha_{\text{-}min}$(mrad)	8.5	8.5	7	2

The case of the HR lens with 600 AT is an exception where the HR/UHR lens combination contributes the largest off-axis aberrations. In this case, the focusing strengths of the HR lens and the UHR lens are both strong, 600 AT and 3171 AT, respectively, shown in FIG 2. 11. When one lens is activated as the objective lens, the HR lens needs 675.1 AT, and the UHR lens needs 3639 AT. Plus, two principle rays r_a and r_b in this combination are not small in either magnetic field of HR/UHR lens, shown in FIG 2. 13. These two factors make the aberration coefficients significant because such coefficients depend on the strength of the magnetic field and two principle rays r_a and r_b. The spherical aberration coefficient does not increase too much, leading to the optimized opening angle (7 mrad) still comparable to the combinations in which the HR lens is relatively weak (8.5 mrad), shown in Table 2. 1. However, the off-axis aberration coefficients grow much. The large off-axis aberration coefficients and large opening angle make the HR/UHR lens contributes the largest off-axis aberrations in this case.

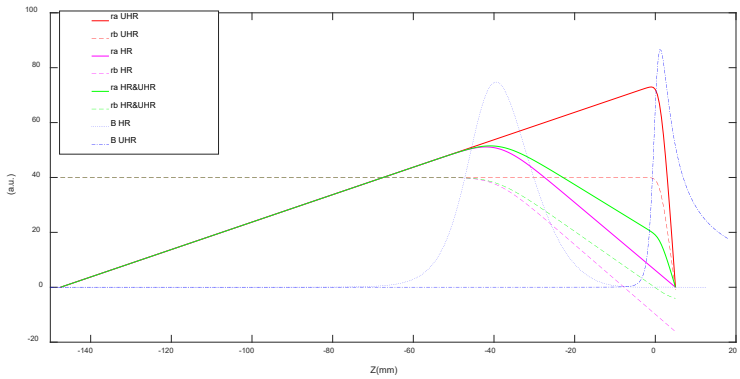

FIG 2. 13 The behavior of principle rays r_a and r_b for different combinations of magnetic objective lenses. The magnetic field distribution of the HR lens and the UHR are also shown in the plot.

The field curvature is still the largest contribution in the off-axis aberrations. After the correction by the MBS unit, the outermost beam spot size and uniformity of beams are much improved when the focusing strengths of the HR lens are strong, shown in FIG 2. 11. For example, if it is desired to have D_{total} / d_{axial} smaller than 1.3, the excitation of the HR lens cannot be stronger than 120 AT without the field curvature correction. The pitch of the beams on the sample is 0.5 μm, and the axial beam has a resolution of 1.3 nm and a current of 55 pA. After the field curvature correction, the excitation of the HR lens can be set to 480 AT, the pitch increases to 1.0 μm, and the axial beam has 1.9 nm resolution and 205 pA current. The second largest off-axis aberration is astigmatism. For its correction, each beam needs its stigmator in the SEM column. The Delft MBSEM1 does not have individual stigmators and thus cannot correct astigmatism. Implementing the individual stigmators in the column is difficult. Firstly we need to disassemble and modify the current SEM column. Secondly, the placement of the multiple stigmators and the alignment between the stigmators and the ALA will be difficult. Thirdly, hundreds of electronics devices and wirings are needed to support the multiple stigmators. So far, we have no plan for the astigmatism correction. So, to minimize the astigmatism contribution, the INT lens that is the largest contributor of the off-axis aberrations needs to be optimized. As the opening angle is expected to be big for the consideration of the beam current, a proper combination of the ACC lens

and the C2 lens is needed to generate a small off-axis distance in the INT lens to reduce astigmatism.

To sum up the discussion in this section:

- The pitch on the sample can be adjusted in a relatively broad range, especially after the field curvature correction;
- The contribution of the off-axis aberrations to the outermost beam becomes more when the HR lens turns stronger in the combination; in most cases, the INT lens contributes the largest off-axis aberration, and the field curvature is the biggest off-axis aberration.

2.2.3 Working distance (WD)

This method is quite straightforward. Here the analysis is done using the ACC3 = 7000V, LE = 15 keV and the HR lens excitation= 480 AT in the HR/UHR lens combination. The reason to choose the ACC3 is already explained. The HR lens setting of 480 AT in the combination is because in section 2.2.2 this setting gives a large pitch with proper uniformity after the field curvature correction. When the WD changes, the coma-free plane of the objective lens shifts and the INT lens changes correspondingly.

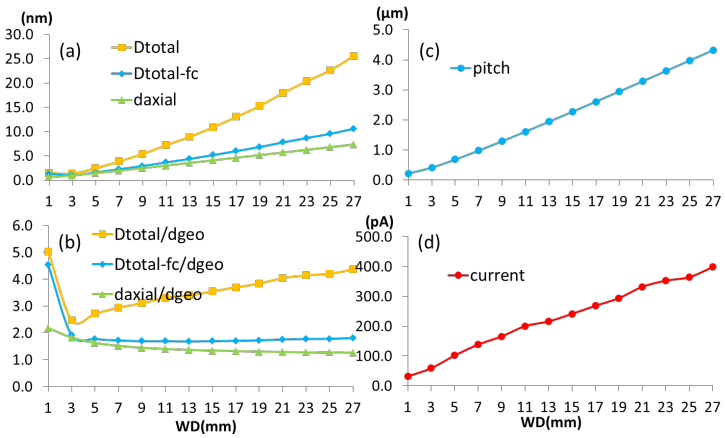

FIG 2. 14 The pitch control using the different working distances. (a) gives the spot sizes, (b) the ratios of the spot sizes over d_{geo}, (c) the pitch on the sample and (d) the current. In each combination, the opening angle is optimized to get the smallest axial beam spot. The reduced brightness B_r used here is 5×10^7 A/(m^{2}srV).

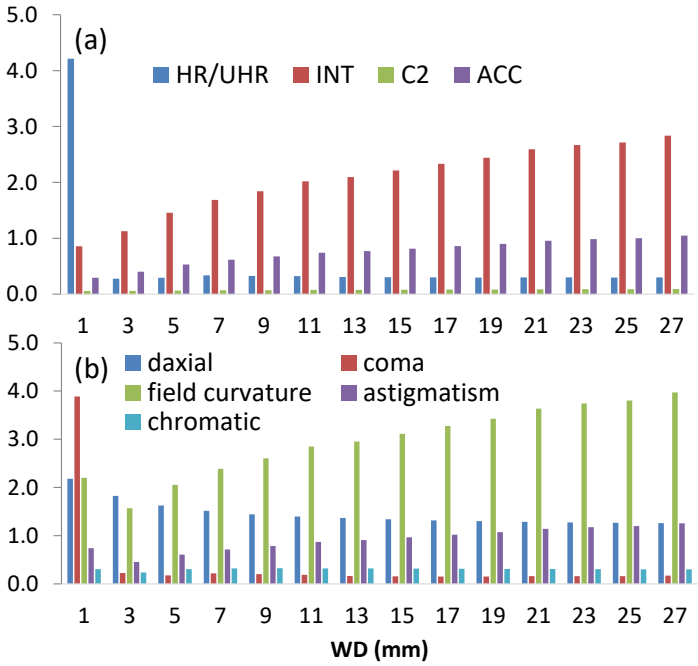

FIG 2. 15 The composition of the outermost beam in the analysis of the different working distances, in terms of lenses and aberrations. The plots show the ratios of all the contributors over d_{geo}.

When the WD varies from 1 mm to 27 mm, the pitch increases from 0.2 μm to 4.2 μm and the current from 31 pA to 398 pA. The axial beam spot size grows slowly from 0.6 nm to 7.4 nm, meanwhile, d_{axial} / d_{geo} improves from 2.2 to 1.3. The outermost beam's spot size becomes large for a large working distance. D_{total} / d_{geo} drops at working distance 3 mm firstly and then rises. Such behavior is different with the traditional impression that smaller WD gives the better optical performance. The off-axis aberrations are the reason. When the WD is 1mm, the UHR lens needs to be strong, 2.4 times stronger than when the WD is 3 mm, resulting in large off-axis aberration coefficients. When the WD is from 3 mm to 27 mm, D_{total} / d_{geo} changes from 2.5 to 4.4, $D_{total-fc} / d_{geo}$ from 1.9 to 1.8, and d_{axial} / d_{geo} from 1.8 to 1.3.

Except for the case of working distance 1 mm, the INT lens contributes the most off-axis aberrations, and the field curvature is the dominant off-

axis aberration. With the field curvature correction, $D_{total-fc} / d_{axial}$ is from 1.1 to 1.4 when the WD changes from 3 mm to 27 mm.

2.2.4 Evaluation of the different combinations

The combination of these three approaches surely produces more possibilities than any single approach does. Therefore, various combinations of the lenses can realize a certain pitch on the sample. For example, there are already three ways of getting a pitch of 500 nm on the sample, shown in the previous results. If the results of all the possible combinations are listed, certainly there will be more than three ways. How should these results be properly evaluated? Here provide two methods. One is to assess the current and the resolution, and the other is to check the uniformity of the beams.

Besides, these combinations obtain a large pitch range, from 0.1 μm to 7.2 μm. The probe size increases along with the pitch. When the pitch is 5 and 7.2 μm, the smallest $D_{total-fc}$ in these combinations is 14.8 nm and 20.7 nm correspondingly. It is possible to optimize the lenses' combination to improve $D_{total-fc}$ a little on any pitch. However, we do not do it because it is time-consuming. We recommend using a pitch smaller than smaller than 5 μm in the Delft MBSEM1. The analysis done below uses the combinations that generate the pitch from 0.5 μm to 4 μm.

a. Resolution and current

Many applications demand a combination of resolution and current, not only resolution. For instance, in the semiconductor field, since the critical dimension is still larger than 10 nm, an electron beam with a spot size of 10 nm is sufficient but expected to have a high current for throughput.

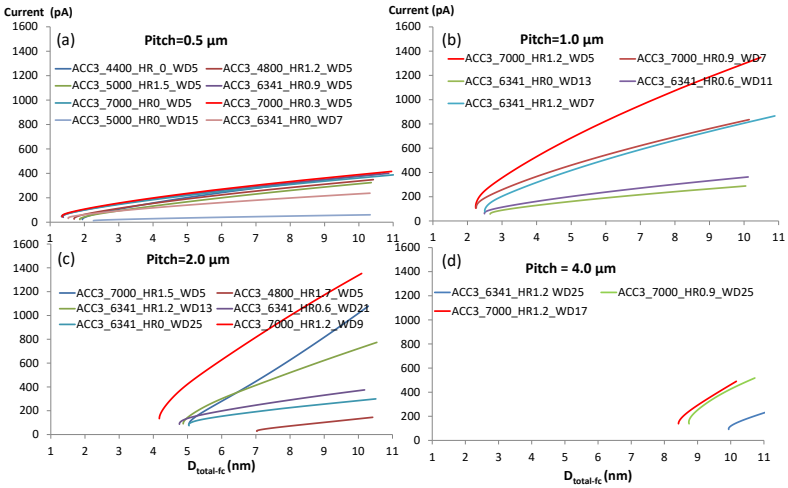

FIG 2. 16 A certain pitch of the primary beams on a sample can be realized by different lens combinations. Plot (a) to (d) shows the curves of the spot size versus the beam current with the pitch 0.5, 1.0, 2.0, and 4.0 µm. X axis is $D_{total-fc}$; Y axis is the beam current. Each curve is plotted by varying the opening angle of the beams.

The curves in FIG 2. 16 show the spot size ($D_{total-fc}$) versus the current for different pitches. They are selected from the finished simulations. Among these curves, we can find the best combination which delivers the best resolution and the largest current for one certain pitch. In such combinations, the whole system's spherical aberration coefficient C_s and chromatic aberration coefficient C_c are the smallest. For example, in the combinations of having 1.0 µm pitch, the combination "ACC3 7000 HR1p2 WD5" has the smallest C_s and C_c, 5.5 mm and 3.8 mm, respectively; the combination "ACC3 6341 UHR only WD13" has C_s and C_c, 64.6 mm and 10.6 mm, respectively. When $D_{total-fc}$ is 2.65 nm, the beam current is 290 pA in the former combination and 57 pA in the latter combination.

FIG 2. 17 collects all these good combinations. It shows that this MBSEM is capable of delivering electron beams with good resolution at different pitches. For example, the outermost beam has 4.2 nm probe size with 2 µm pitch and 8.4 nm probe size with 4 µm pitch when the landing energy is 15 keV. However, the large pitch does not always deliver the high current when one spot size is chosen. It is out of our expectation.

The curves showing 0.5 µm pitch and 1.0 µm pitch match the expectation, but the others not. To achieve 10 nm resolution, the combination of 1.5 µm pitch delivers the largest current 1.4 nA, while the combination with the largest pitch 4 µm, delivers 0.5 nA. The fact is due to the aberration contribution and is because the Delft MBSEM1 column is not designed for MBSEM purpose. If the lenses are designed perfectly for MBSEM, this issue will be improved.

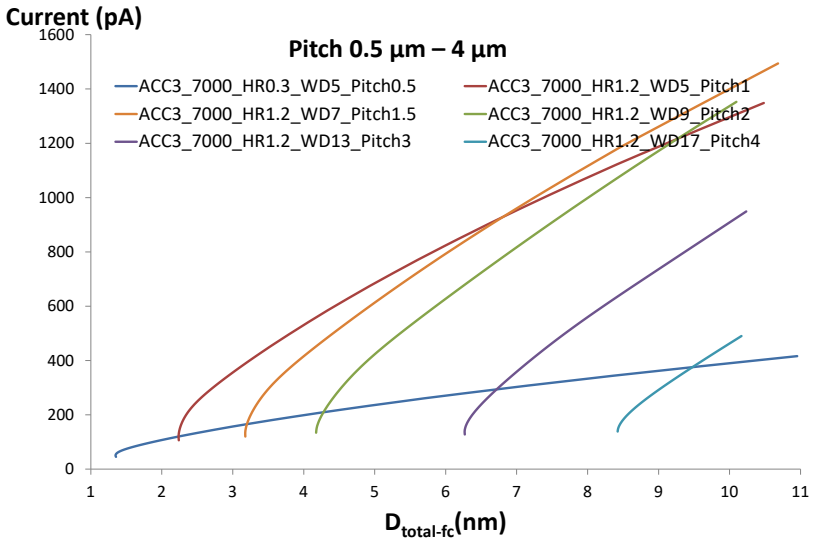

FIG 2. 17 Picking out the best curve in each pitch and putting together. X axis is $D_{total-fc}$; Y axis is the current I_p . Each curve is plotted by varying the opening angle of the beams.

b. Uniformity

Uniformity is a crucial specification of MBSEM. Here factors d_r and d_{r-fc} are introduced to assess it.

$$d_r = D_{total} / d_{axial} \qquad (2.7)$$

$$d_{r-fc} = D_{total-fc} / d_{axial} \qquad (2.8)$$

When the off-axis aberration is well controlled, d_r and/or d_{r-fc} are quite stable with the increase of the opening angle, shown in the plots (a) -(c) in FIG 2. 18. The largest d_r 1.32 happens when smallest axial spot size (1.3 nm) is achieved. The phenomenon is because the axial beam's spot

size has a minimum while the off-axis aberrations always grow big with the increase of the opening angle. After the field curvature correction, the largest d_{r-fc} is only 1.05. d_r and d_{r-fc} get improved when the opening angle becomes larger because the spherical aberration increases faster than the off-axis aberrations. The spherical aberration is proportional to the third power of the opening angle, while the off-axis aberrations, at most, are proportional to the second power of the opening angle. FIG 2. 18 (d)-(f) show the case in which the off-axis aberrations are not well controlled. When the axial beam has the smallest size, d_{r-fc} is around 1.5, which means the off-axis aberrations' contribution to the outermost beam is already larger than the axial beam size. So, it is important to control the outermost beam's off-axis aberrations when the axial beam has the smallest probe size.

FIG 2. 19 contains different combinations that generate the pitches from 0.5 μm to 4 μm. Plot (a) and (b) are the combinations picked out for the best uniformity. The combinations in this selection have lower currents than the combinations chosen for the resolution and the current. To get good uniformity when the axial beam has the smallest probe size, the C_s and the C_c need to be large to compensate the off-axis aberrations, resulting in a small opening angle and a low current in the beams. Under the same reasoning, the combinations with good resolution and current have bad uniformity, shown in the plot (c) of FIG 2. 19.

To conclude, the good uniformity in the Delft MBSEM1 can be achieved in a large pitch range with the compromise of the resolution and the current. Reducing the off-axis aberrations is the efficient solution to this issue. However, using the existing column can improve it little.

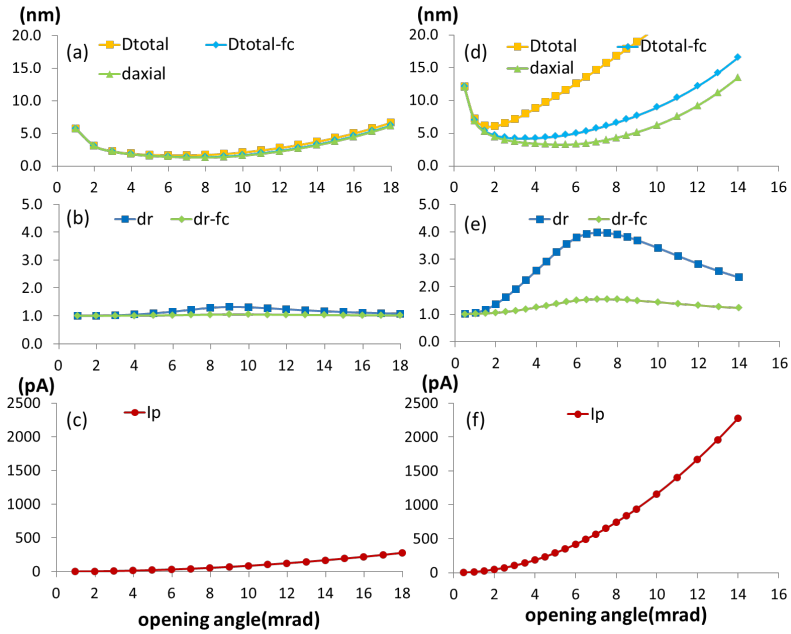

FIG 2. 18 (a), (b) and (c) plots present the result from the combination (ACC3 7000V HR0.3 WD5mm) with 0.5 μm pitch. (d), (e) and (f) plots present the result from the combination (ACC3 7000V HR1.2 WD9mm) with 2.0 μm pitch.

2.3 Landing energy control

There are two ways to change the landing energy in our MBSEM. One is to keep the sample ground and bias the electron source appropriately. The way is easy and often-used. However, it has a big drawback when we need low landing energies in the Delft MBSEM1. In the column, all the parts below the ACC lens are grounded so that the beams keep a constant energy from the ACC lens to the objective lens, a distance of about 400 mm. For example, when the landing energy is 1 keV, the beams need to travel 400 mm with 1 keV energy. Such electron optical system is not desired because it easily brings large aberrations and probably has trouble from Coulomb interaction.

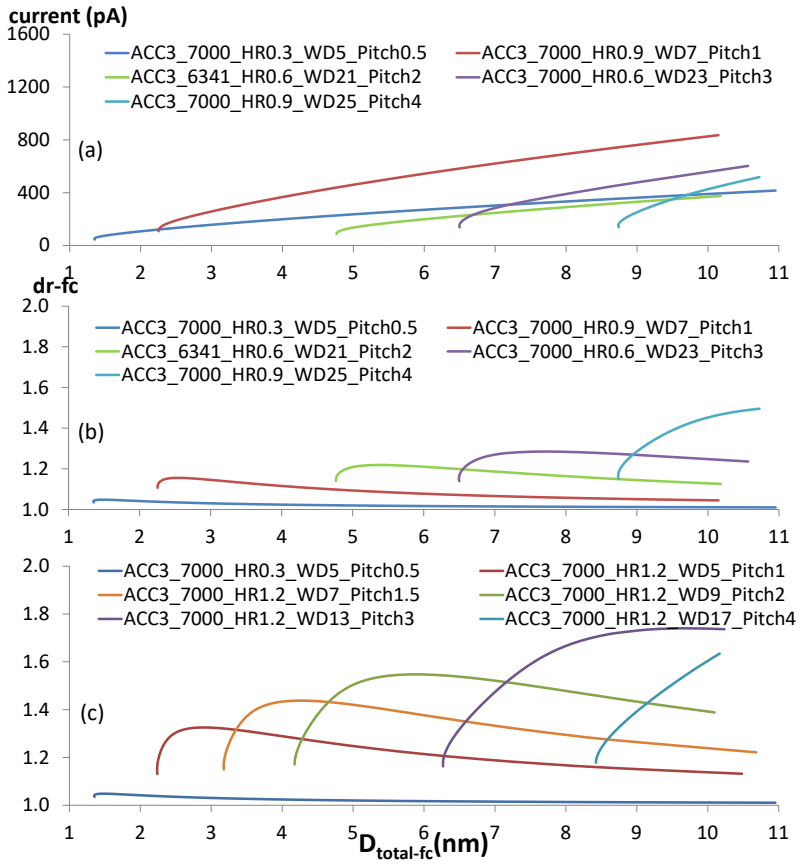

FIG 2. 19 (a) and (b) show the combinations to get good uniformity of beams; (c) presents the combinations used in FIG 2. 17, which have large currents but compromise the uniformity of the beams. Each curve is plotted by varying the opening angle of the beams.

The other way is to bias the sample negatively. In this way, the beams travel with high energy in the column and are decelerated to the target energy on the sample. In the analysis, when the landing energy is lower than 15 keV, we prefer to use the biased sample strategy. As Section 2.2 already describes the high landing energy (15 keV) performance, only low landing energy cases are studied here.

Table 2. 2 presents the electron optical properties of the Delft MBSEM1 when the landing energies are 1, 2.5, 5, and 10 keV. In the MBSEM, the sample is biased negatively, and the primary beams energy before the sample is 15 keV. These calculations are done with the voltage on the ACC3 7000 V, only the UHR lens activated and the working distance of

5 mm. Section 2.2 proves that such condition is easy to have high-resolution beams.

Table 2. 2 The main electron optical parameters of the MBSEM using the different landing energies of 1, 2.5, 5 and 10 keV. The opening angle α is determined by getting smallest axial beams' probe size.

Parameter LE (eV)	10k	5k	2.5k	1k
Main optical parameters				
D_{total} (nm)	1.7	2.0	2.4	2.9
$D_{total-fc}$ (nm)	1.5	1.7	2.0	2.6
$d_{axial-\min}$ (nm)	1.4	1.7	2.0	2.5
$I_{p-\min}$ (pA)	45.3	42	35.4	25.7
$\alpha_{-\min}$ (mrad)	8.6	10.5	12.4	15.1
Pitch (nm)	520	579	637	705
WD(mm)	5.0	5.0	5.0	5.0
Contribution to the probe(nm)				
geometrical	0.7	0.8	0.9	1.0
spherical aberration	0.5	0.5	0.5	0.3
chromatic aberration	0.6	0.8	1.1	1.6
diffraction	0.8	0.9	1.1	1.4
$d_{offaxis}$	1.0	1.2	1.3	1.4
$d_{offaxis-fc}$	0.4	0.4	0.4	0.6

When the landing energy is low, the optimized opening angle is large, due to the low axial aberration coefficients generated from the combination of a magnetic immersion lens and a strong electrostatic lens. The large opening angle eases the diffraction error of the beam with low energy. However, the current still decreases because of low beam energy and the conserved reduced brightness of electron source.

The pitch control in different landing energies can be simulated by repeating the three approaches in section 2.2. Here only the third approach (varying working distance) is used. The voltage on the ACC 3 electrode is 7000 V, and the UHR lens is activated as the magnetic objective lens.

FIG 2. 20 shows that, after the field curvature correction, the resolution of the outermost beam is well under control except in the case of 1 mm working distance. The beams have proper currents, $D_{total-fc} / d_{geo}$ always about 2. The beams are quite uniform and d_{r-fc} is always around 1.1 in all these landing energies. The smallest spot size in the case of the 1 keV landing energy is 1.8 nm with 14.6 pA using the working distance of 3 mm. In the plots, the opening angle is optimized for the smallest spot size of the axial beam.

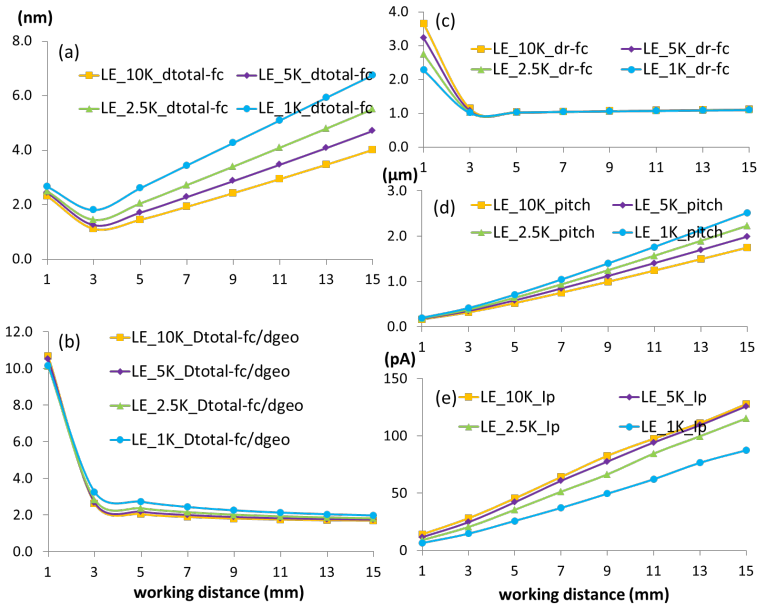

FIG 2. 20 The pitch control of different landing energies by varying the working distance from 1 mm to 15 mm. The result is got using ACC3 is 7000V, UHR lens only, initial beam energy 15 keV and the sample biased to get the right landing energies. (a) shows $D_{total-fc}$; (b) the ratio $D_{total-fc}$ over d_{geo}; (c) presents d_{r-fc}, or $D_{total-fc} / d_{axial}$; (d) the pitch on the sample and (e) the current. In each case, the opening angle is optimized for the smallest axial beam spot size.

FIG 2. 21 plots the probe size versus the beam current for different landing energies. Similar to the result in FIG 2. 17, the large pitch does not always deliver the large current.

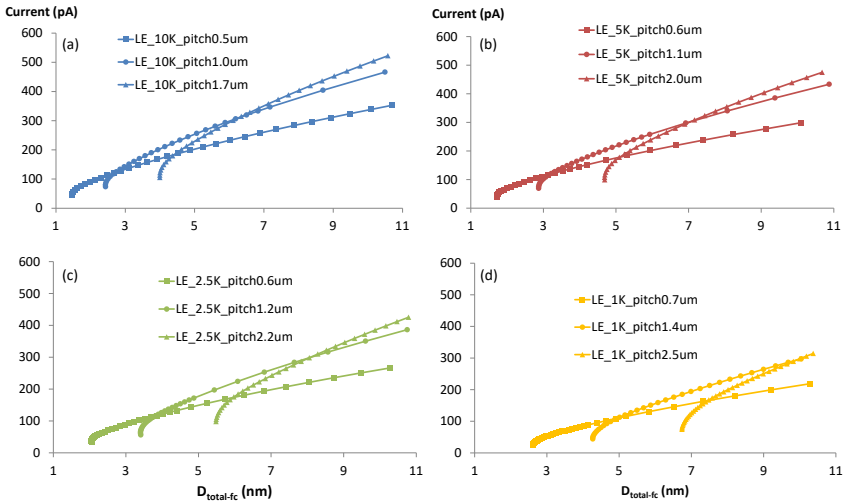

FIG 2. 21 $D_{total-fc}$ versus the current plots for various pitches on the sample using different landing energies.

2.4 Conclusion and outlook

2.4.1 Conclusion

In this chapter, the pitch control and the landing energy control in the Delft MBSEM1 are analyzed. The control of the pitch is discussed by analyzing the contribution of the different lenses when the landing energy is 15 keV. The entire system is divided into three parts. The first part is the combination of the ACC lens and the C2 lens; the second is the combination of the INT lens and the HR/UHR lens; the third part is the working distance. In the analysis, when one part is discussed, the other two parts are set to a fixed condition. The aberration contributions from the lenses and the different types of aberrations are compared. Later, the combination of these three parts is evaluated. The pitch control under different landing energies is also analyzed. The landing energy can be set freely in this MBSEM. When the landing energy is lower than 15 keV, it is preferred to bias the sample to achieve the target energy.

We prove that this MBSEM can work well when the pitch of the primary beams on the sample is large and when the landing energy is low. We recommend using the pitch smaller than 5 μm. The outermost beam with 15 keV landing energy can have 4.2 nm spot size when the pitch is 2 μm, and 8.4 nm probe size when the pitch is 4 μm. When the landing energy is 1 keV, the outermost beam has a spot size of 1.8 nm with a current of 14.6 pA.

As one pitch can be achieved by using different combinations of the lenses in the MBSEM, two ways are introduced to evaluate these combinations. One is to assess the current and the resolution. The other is to check the uniformity of the beams. We expected that the lens combination generating large pitch would deliver the large resolution and the large current. However, it is only true when the pitch is smaller than 1 μm, due to the contribution of the axial aberrations and the off-axis aberrations. The good uniformity of the beams can be achieved in a large pitch range with the compromise of the beam current. The combination of the lenses usually cannot satisfy both requirements at the same time.

2.4.2 Outlook

After the analysis, a few suggestions are made for the Delft MBSEM1.

Firstly, The C2 lens should be left out if the VA is used to select currents. The ACC lens is capable of forming a common crossover in the VA plane where the aperture strip is used to select currents. There is no benefit to using the C2 lens for the pitch control, even though it seems like that it delivers a large pitch range. When the C2 lens is switched on to form an extra crossover between the ACC lens and the C2 lens, either the off-axis aberration contribute too much to the off-axis beams, or the beams have too little current.

When it is not obligatory to have a common crossover in the VA plane, a new version of MBSEM is proposed, shown in FIG 2. 22. The ACC lens forms a common crossover in the center of the C2 lens. The C2 lens focuses each beamlet to the principle plane of the INT lens. The INT lens forms another common crossover in the coma-free plane of the HR/UHR lens. The HR/UHR lens focuses each beamlet on the sample. This configuration makes the ACC lens, C2 lens, and INT lens generate almost

zero off-axis aberrations. An example is simulated using such configuration with a landing energy of 15keV, a working distance of 5 mm and only the UHR lens activated as the magnetic objective lens. Its result is compared to the best result of the existing configuration which generates the same pitch on the sample, shown in FIG 2. 23. Clearly, the modified version MBSEM has finer probe size and higher beam current.

Secondly, the ACC lens can be optimized. The precise positioning and voltage setting of ACC lens are required to make the image plane of the aperture lens coincide with the object principle plane of ACC lens. Using extra power supply for the ACC2 electrode is helpful to shift the principle plane in a small range. The angular magnification from the emission tip to the common crossover should be small to let the outermost beams have the small off-axis distance in the INT lens. Thirdly, the INT lens needs optimization as it always contributes the most off-axis contribution to the outermost beams.

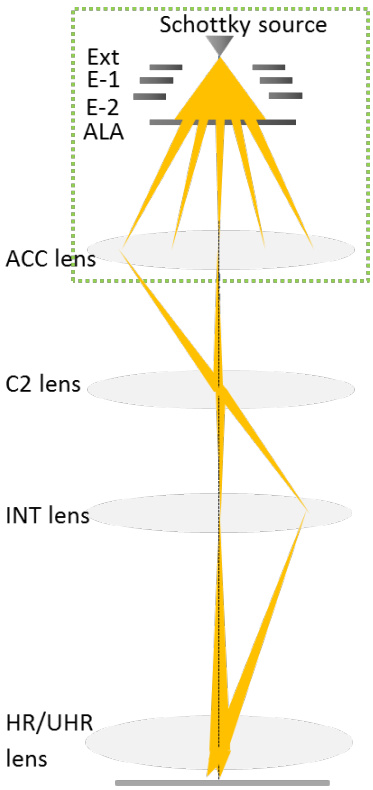

FIG 2. 22 A modified version of MBSEM based on the current SEM column.

Last but not least, the magnetic objective lens should be optimized for the pitch control. In the present structure, the combination of the HR lens and the UHR lens working as the magnetic objective lens is helpful to achieve large pitch range on the sample. However, when the pitch is large, the spherical aberration coefficient and the chromatic aberration coefficient become significant, leading to the small beam current. A novel design for the magnetic objective lens is needed to have good axial and off-axis aberration performance when the pitch on the sample is large.

Such suggestions give just an outline, the detailed lens structure and the optics design need to be done in the EOD or a similar electron optics simulator.

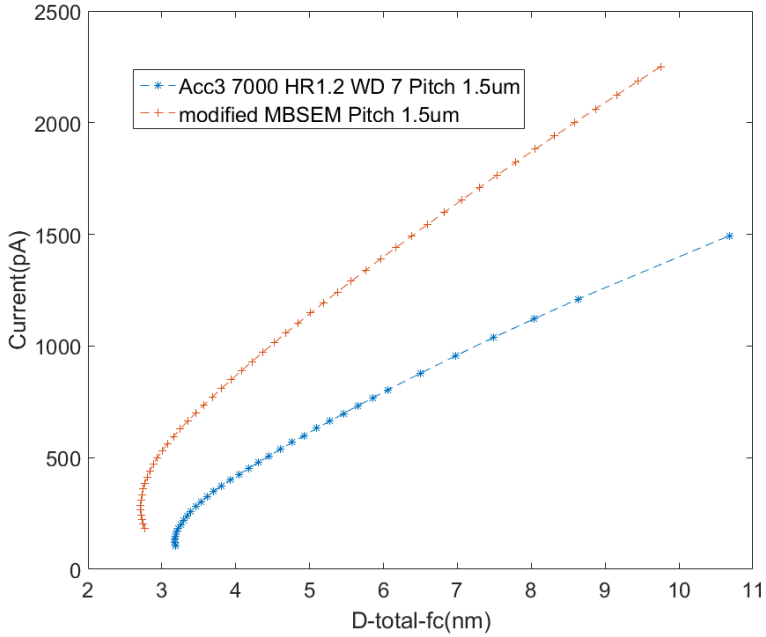

FIG 2. 23 Comparison between the proposed MBSEM with the current MBSEM when a pitch of 1.5 µm is achieved, showing that the proposed version has better optical performance.

2.5 References

[1]A. Mohammadi-Gheidari, C. W. Hagen and P. Kruit. J Vac Sci Technol B **28**, C6g5 (2010).

[2]P. C. Post, A. Mohammadi-Gheidari, C. W. Hagen and P. Kruit. J Vac Sci Technol B **29**, 06F310 (2011).

[3]P. Kruit, M. Bezuijen and J. E. Barth. Journal of Applied Physics **99**, 024315 (2006).

[4]A. Mohammadi-Gheidari and P. Kruit. Nucl Instrum Meth A **645**, 60 (2011).

[5]Y. Zhang. *A 100-electron-beam source from a high brightness Schottky emitter for fast patterning applications*, (2008).

[6]Casino v. v2.48 (2011).

Chapter 3 Transmission electron imaging in the Delft MBSEM1

This chapter proposes a solution to achieve transmission electron imaging in the Delft MBSEM1. In this imaging system, the 196 TE beams are converted to 196 photon beams whose intensities are recorded via an optical microscope. An off line image processing program retrieves each beam's transmission signal and constructs images. Experimental results prove the working principle of transmission electron imaging and show that details of 10-20 nm in images of biological specimen are visible. Problems encountered in the experiments are discussed and plans for future improvements are suggested.

3.1 Introduction

Commercial SEMs usually provide SE imaging system and BSE imaging system. To biologists, the BSE imaging is more attractive because it mainly provides sample's component information which is their interest, than the SE imaging which primarily provides topography information and very weakly reflects the component information by so-called SE2's which are generated by BSE in the interaction volume,[1,2] shown in FIG 3. 1. However, BSE imaging encounters problem when biological tissues are sliced very thin. For good 3D structure reconstruction, the slice needs to be about 30-40 nm thin.[3] The BSE generation is low in such thin slices, as it is linearly proportional to the thickness of tissue,[1] as in:

$$\eta(t) = c(E)NZ^2\rho t \qquad (3.1)$$

where η is the BSE generation coefficient, c is a constant for one incident beam energy, N is the number of electrons per unit volume, Z is the atomic number, ρ is the atomic density and t is the thickness of the tissue. BSE imaging needs a long dwell time to obtain a decent image with such thin samples. Our imaging experience tells us that the dwell time needs 10 μs for landing energy 5 keV using the concentric backscatter detector in FEI Verios SEM when the tissue is not heavily stained. This long dwell time makes BSE imaging even less often used by biologists than SE imaging.

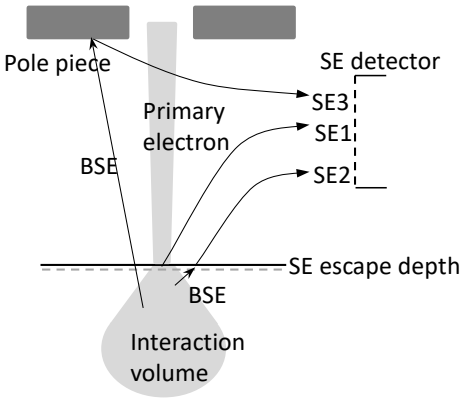

FIG 3. 1 Illustration of different types of secondary electrons, SE1, SE2 and SE3.

Transmission electron (TE) imaging offers another possibility to produce good contrast imaging, because the transmission signal, similar to the BSE signal, also carries the composition and mass density information. For very thin tissues, the TE generation coefficient can be estimated as

$$\gamma = 1 - \eta \qquad (3.2)$$

where γ is the TE generation coefficient. When the sample is very thin, γ is usually much larger than η except when the primary beam's landing energy is so low that most primary electrons are absorbed in the sample. For 10 keV landing energy and a 50 nm biological tissue slice, γ is even > 99 %.[4] So it is easier to detect TE than to detect BSE for thin tissue. This does not mean, however, that the TE signal provides better imaging contrast or signal to noise ratio (SNR). This is as complicated as comparing bright field imaging to dark field imaging, and is beyond the scope of this thesis.

Some researchers have already shown good quality TE imaging results using biological specimens.[4,5] J. Kuipers *et al.* even proved that TE imaging quality was as good as, or even better than BSE imaging quality in their research.[6] Besides, since the invention of the transmission electron microscope (TEM), biologists have used mainly bright field transmission imaging for their low- to-medium resolution images. Such results have motivated us to develop a TE imaging system in our MBSEM.

In this chapter, the optical system in the Delft MBSEM1 is briefly explained. The design principle of TE imaging system in the Delft MBSEM1 is discussed in detail. Our first, low throughput experimental results using off line image processing program are presented. Problems encountered in the experiments are discussed and plans for future improvements are suggested. It is possible to apply the technology used for the TE imaging in the Delft MBSEM1 to other types of MBSEMs.

3.2 Optical system in the Delft MBSEM1

FIG 3. 2 shows a schematic overview of the electron optical system in the Delft MBSEM1, which is based on a regular FEI Nova-Nano 200 SEM, but equipped with a multi-electron beam source (MBS) module. It uses one ZrO/W Schottky source to generate a 14 × 14 array of focused beams with a resolution and current per beam comparable to a state of the art single beam SEM.[7] So this MBSEM should have 196 times higher throughput than a single beam SEM if we can make the detection as efficient.

Determined by the MBS unit, the ratio of geometrical spot size of beams over the pitch on the sample is fixed, 95 nm/70 μm. The beams' pitch on the sample is adjustable, but preferably smaller than 5 μm, otherwise the off axis aberrations make the spot size of the outermost off axis beam much larger than the spot size of the axial beam when the opening angle is optimized to get the smallest spot size of the axial beam on the sample, in the simulation using the electron optical design (EOD)[8] package.

A single beam working mode is also available in the Delft MBSEM1.[9] In this mode, instead of all the beams having a crossover in the variable aperture [(VA), shown in FIG 3. 2], the beams are separate with a pitch larger than the aperture size so that only one beam can go down to scan the sample. The single beam mode works the same way as in the standard single beam SEM. It can be used to get a large field of view (FOV) and to pinpoint the region of interest. Then the multi-beam mode is switched on for high throughput imaging. The mode switch is simply done by assigning the magnetic lenses in the column with different strengths.

Three imaging systems are planned to be built in this MBSEM: for TE, SE and BSE detection respectively.

For the SE detection in a MBSEM, a new detection strategy should be developed. It is impossible to use the traditional SE detection method employed in single beam SEM, because all SE beams are mixed and there is no way to separately collect one beam's SE signal. Generally speaking, in MBSEM the SE beams generated in a sample need to be accelerated into the SEM column, and to be focused with a large magnification in a chosen detection plane to make SE beams' pitch larger than SE beams' spot size so that SE beams can be separately collected. Meanwhile, the primary beams' focusing will be modified but should not be disturbed by the SE beams' focusing and detection. In the Delft MBSEM1, it is preferable to place the SE detector in a plane (such as the VA plane) where the primary beams have a common crossover in order to make the SE detection bring as little disturbance as possible to the primary beams and to keep the whole system compact. An electrostatic lens is introduced to generate proper energy difference between the primary beams and the SE beams, the difference which makes it possible to use the same lenses to focus the primary beams on the sample and to focus the SE beams in the detection plane. Some mechanical modification has to be done to achieve the SE detection. The methods used in the Delft MBSEM1 will be reported in Chapter 4.

The BSE detection in MBSEM is more difficult than the SE detection. In the conventional definition, BSE has an energy range from 50 eV to the primary beam's energy with a full opening angle (from 0^o to 90^o). Such distribution makes it very hard to separate one beam's BSE signal from its neighbors'. We are struggling to find a good solution and as far as we know, no BSE detection system has yet been successfully developed for MBSEM.

TE imaging does not need any modification to the primary beams' focusing setup. This advantage makes it possible to apply the TE imaging system to every MBSEM. This chapter focuses on the realization of TE imaging in the Delft MBSEM1.

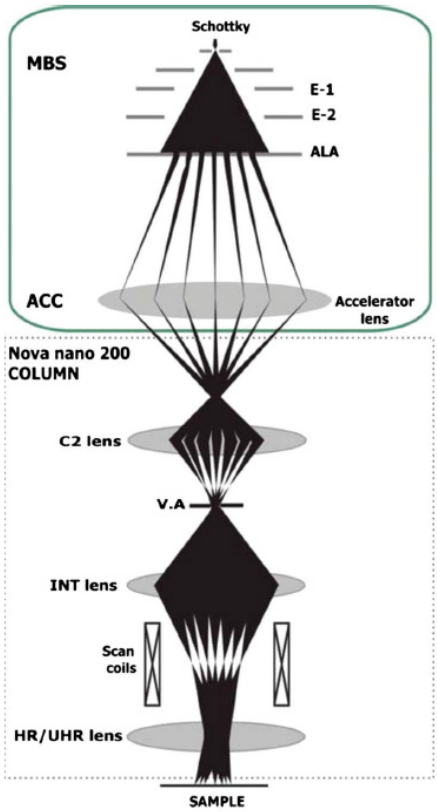

FIG 3. 2 Optics schematic of the Delft MBSEM1. Multi-beam source, electrode 1, electrode 2, aperture lens array, accelerator lens, variable aperture, intermediate lens, high resolution lens and ultra-high resolution lens are abbreviated as MBS, E-1, E-2, ALA, ACC, INT lens, HR and UHR lens respectively.

3.3 TE imaging system design in the Delft MBSEM1

The first challenge of the TE detection is to separately collect the TE signals because they have the same small pitch as the primary beams have on the sample, smaller than 5 μm, even smaller than 1 μm for 1.2 nm imaging resolution.[7]

There are at least two ways to do this. The first way is to introduce an additional electron optical system to focus the TE beams with a large magnification onto a detector where the TE beams will be focused with a small spot size and large pitch (at least larger than the largest spot size of focused TE beams). TEM uses this strategy.[10] In TEM there is no problem getting good focusing with large magnification and one is free to

choose between the bright field mode and the dark field mode for different contrast. However, the disadvantage of utilizing this strategy in the MBSEM is that new electron optical lenses need to be added. Firstly, the sample chamber has a finite volume so that it is not easy to insert new electron optical parts, including all the lenses, cables and connections. Secondly, the magnetic immersion objective lens, which is used to get the best resolution for the primary beams focusing, would interfere with the new add-on lenses. Such an objective lens usually needs strong excitation and its field distribution has a very long tail.[11] A little change of objective lens excitation may spoil the add-on electron optical system. The combination of these two issues makes it difficult to implement this strategy in this MBSEM.

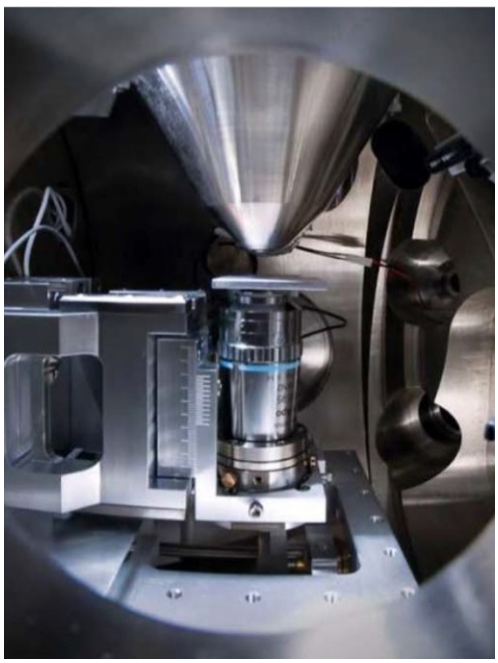

FIG 3. 3 View of integrated optical microscope in a SEM chamber.

The other way circumvents the interference issue by converting electrons to photons using fluorescent material. When the TE beam's pitch is larger than the photon generation volume size in the fluorescent material, the 196 separate TE beams create 196 separate light sources. An optical microscope is then used to image these light sources with a large magnification onto a camera. This optical microscope should be capable

of working inside the vacuum, providing better resolution than the beams' pitch, providing large numerical aperture (NA) for high collection efficiency, and having good alignment with the SEM column. The difficulty of this strategy is in adding such an optical microscope into the SEM's sample chamber. In our group we had just developed such a platform for correlative light-electron microscopy, the "SECOM platform"[12], further commercialized by Delmic, a spinoff company in the Netherlands. This platform places the optical microscope inside the vacuum chamber, shown in FIG 3. 3. An optical objective lens with high magnification and high NA is placed under the thin sample; A mirror and an vacuum glass window are used to to transit light between the air environment and the vacuum chamber. A tube lens sitting in the air forms an image onto a camera. It is designed for biological research. Here we employ this SECOM platform for TE imaging, as schematically shown in FIG 3. 4.

This strategy has limitations. One limitation is the resolution of optical microscopy. Due to the diffraction limitation, sub micrometer resolution is difficult to achieve unless we use liquid immersion lenses. This strategy probably will fail when the primary beams' pitch on the sample is smaller than 1 μm. In terms of resolution, a larger than 1 μm pitch on the sample leads to no better than 3 nm optical imaging resolution of the Delft MBSEM1, because the ratio of geometrical spot size of beams over pitch on the sample is fixed, 95 nm/ 70 μm.

Another limitation is that the sample should be closely placed on the fluorescent material. When there is a 1 mm gap between the sample and the fluorescent material, if we assume that TE beams have a similar opening angle as the primary beams, typically 10 mrad, a TE beam grows to be a spot of 20 μm, much larger than the pitch. Neighboring TE beams will mix together in the fluorescent material. So it is recommended that thin tissue should be directly placed on fluorescence material to restrain TE beams' spread. The consequence of this placement is that there is no bright field mode and dark field mode anymore in this TE imaging system because all of the transmitted electrons from a primary beam have been collected. Additionally, it will be difficult to remove thin tissues from the fluorescent material without damage.

After the comparison of these two options, the latter is chosen, that of using the SECOM platform.

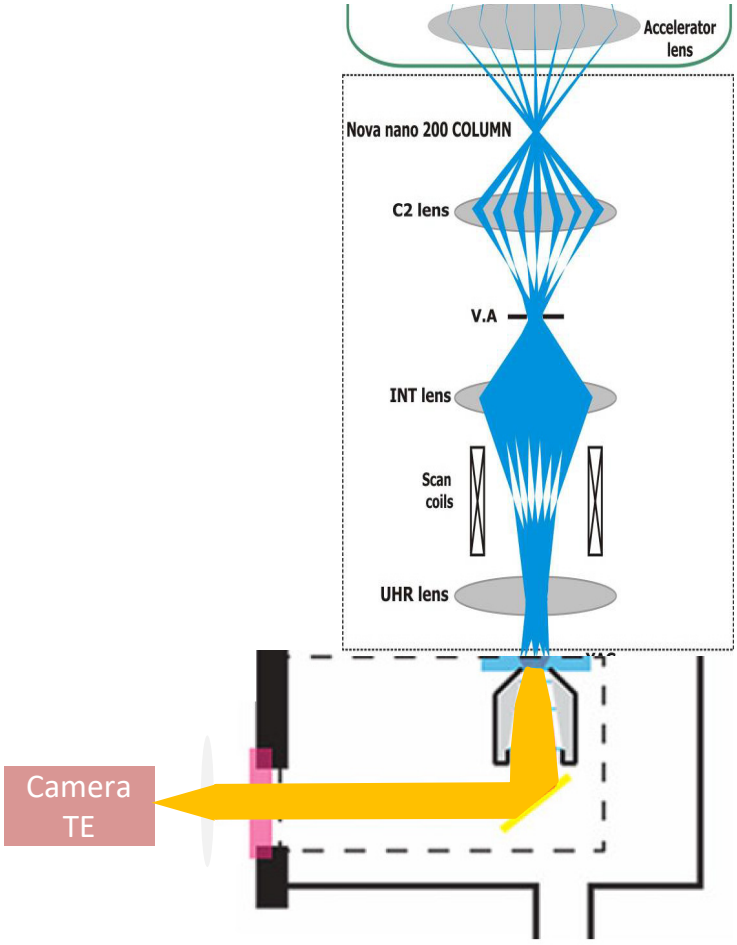

FIG 3. 4 Combination of the Delft MBSEM1 and the SECOM platform.

The remaining challenge is to detect the intensities of the TE beams. We want to read each beam's TE signal out in each scan step for live imaging. One possible way is to use a detector array, one detector for one beam. This concept is employed in the Zeiss' MBSEM for SE detection, and is quite a straightforward method. In the scanning, one beam's signal should always fall into its own detector. Considering that the scanning

FOV is usually equal to, or a bit larger than the beam's pitch, it is necessary to have de-scan system which is synchronized with the primary beam deflectors to compensate the TE signal shift on the detector.

It is also possible to use a CCD or CMOS camera and fast image processing technology to detect the intensities. A camera image of the 196 light sources (or the 196 TE beams) is generated in each scan step, an example of which is shown in FIG 3. 5. These 196 beams' intensities can be retrieved from such an image and assigned to corresponding beams using an image processing program. For live imaging, these two steps need to done in one scan dwell time.

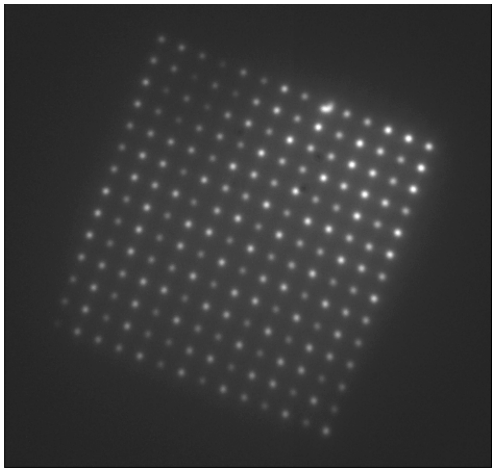

FIG 3. 5 Image of 196 beams with pitch 4 μm onto an Yttrium Aluminum Garnet (YAG, Y3Al5O12) screen and recorded by a camera.

The advantage of the first option is that each sub-detector is similar to a normal detector, so it is easy to process detected signals. The disadvantages are that we need to add a de-scan system, and that thousands of electronics cables and controls need to be used for detector array. Plenty of modifications have to be made to the SEM column for this option to be viable.

The advantage of the second option is that it is easy to start because all parts are commercially available for the concept proof test, and the whole detection unit is compact. A disadvantage is that it is very demanding for the camera and the image processing program. If 100 ns dwell time is used - the dwell time which is normally used in single beam SEMs for

fast scanning - the camera needs to have 10×10^6 frames per second (FPS) rate and very good sensitivity. If one TE spot needs 10×10 camera pixels to record, then there should be more than 19600 pixels in one camera image. The first problem is that such a camera is both rare and expensive. The second problem is that of transferring and processing 196 GByte data in one second when each pixel has 8 bit depth.

It is hard to tell which one is better, or easier for the TE detection in the Delft MBSEM1. We have chosen an easy start: the combination of a camera and fast image processing technology to prove the working principle of the TE detection system. It is not necessary to use a 10 M FPS camera in the beginning stage because it is expensive and complicated to transfer data and process the images so rapidly. We divide the TE imaging system development into three steps. In the first step, off-line image processing with the low throughput imaging method is employed to prove this imaging concept. The camera "Prosilica GE680" from Allied Vision Tech is utilized. It has 7.4 μm pixel size and 205 frames per second at resolution 640 × 480. A Nikon 40× objective lens is used in the optical microscope to have a 40 times magnification. A Labview program saves one camera image with 196 TE beams information into a computer in each scan step during a scan period. Then the off-line image processing program, which I wrote in Matlab, is used to calculate each beam's intensity and position in each scan step and then use all the intensities in a scan period to construct its TE image and the whole TE image map. The experimental results shown in Sec 3.4 of this chapter were obtained using this off-line method.

In the second step, a slow real time imaging program based on field programmable gate arrays (FPGA) technology is developed.[13] A FPGA stands between the camera and the computer. The camera continuously sends images via a camera link to the FPGA where an image processing algorithm is written to calculate each beam's intensity in each scan step. The algorithm builds a beams' mask based on one TE beam's image before real time imaging starts. In the real time imaging, the mask shifts, synchronized with the beams' scan step, and is used to calculate the beams intensities quickly in each scan step and to assign intensities to the 196 beams. Then the FPGA sends these intensities' information to the computer where a Labview program is used to construct TE images. The

goal of this step is to achieve a slow real time imaging at a camera rate of several thousand frames per second. In the final step, the fast real time imaging will be realized by utilizing a very fast camera (such as the 10M FPS camera).

To sum up, the TE imaging system of the Delft MBSEM1 adopts a SECOM platform with fluorescent material to convert electrons to photons, a camera and fast image processing technology. Section 3.4 presents experimental results from off-line processing.

3.4 Experimental results

In the experiment, yttrium aluminum garnet (YAG, $Y_3Al_5O_{12}$) is chosen to convert electrons to photons, because it has very high conversion efficiency (about 21 photons/keV/electron for low beam energy) and short decay time (70 ns, which is short enough for our current experiments), in addition to being commercially available in different sizes and thicknesses. Our YAG with a thickness of 20 µm and also the source of the YAG data are supplied by the company "Crytur".

3.4.1 Sample information

In the experiments, two types of samples are used. One is a calibration sample, shown in FIG 3. 6. These patterns are made by depositing tungsten on top of YAG. The line patterns have 1 µm pitch and 0.5 µm line width and the hole patterns have 0.6 µm pitch and 0.4 µm diameter. The reason to use this calibration sample is that in the Delft MBSEM1, though using the original FEI column, the focusing condition and the lens combinations are different than in the original FEI setup. Thus scan FOV and magnification shown in FEI user interface are not correct. This sample can be used to calibrate scan FOV.

FIG 3. 6 Calibration sample; the color part is electron transparent area and the white is tungsten. Lines: 0.5 µm wide, 1 µm pitch; Holes: 0.4 µm diameter, 0.6 µm pitch.

The other type is rat pancreas tissue provided by UMCG Groningen (Giepmans group) in the Netherlands. The heavily stained sample has a

thickness of 100 nm. These samples are directly placed on top of a YAG disk which has 50 nm aluminum coating for conduction and for reflecting all photons to the optical microscope. Although in principle TE imaging is capable of getting good contrast images with little or no stained sample, here the heavily stained sample is used in the experiments. The reason is that the detection chain in the TE imaging system in the Delft MBSEM1 is still in its first development phase and many factors have influence on the TE imaging detection efficiency and the imaging contrast, for example, the choices of camera and fluorescent material, and even the way we prepare the tissues on YAG. Now we are struggling to find the proper way to place thin tissues on the YAG. So it is better to start from the sample which is heavily stained and can easily give good contrast images in order to prove the working principle.

3.4.2 Imaging results

All the experiments in this section are done using a landing energy of 15 keV in the Delft MBSEM1.

a. Single beam mode imaging

In the operation, it is preferable to use single beam mode to have an overview of the sample and then to select the region of interest, demonstrated in FIG 3. 7.

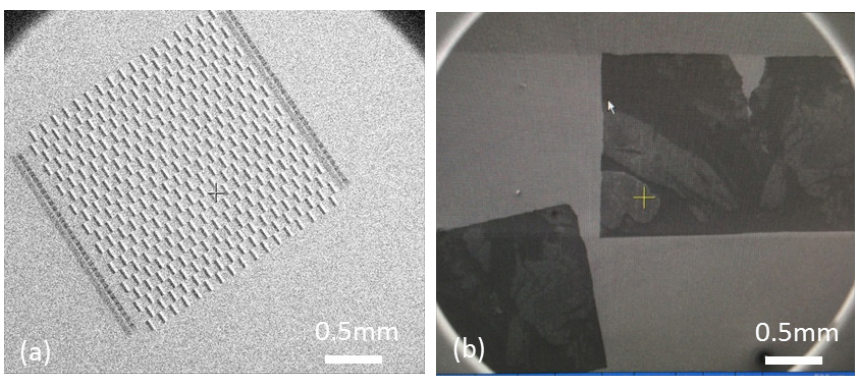

FIG 3. 7 Overview of the samples using single beam mode in order to select region of interest quickly. (a): the calibration sample; (b): the biological sample.

b. Multi beam mode imaging

The 196 beams are labelled by using four quadrants, shown in FIG 3. 8. Beams from different locations in the E-beam grid give similar performance using the calibration sample, shown in FIG 3. 9. These images are used to calibrate the scan FOV and scan magnification. The current of each beam-let in these experiments is around 30pA.

FIG 3. 10 and FIG 3. 11 show TE images of the rat pancreas tissue sample. The beams, regardless of whether from the center or from the edge of the E-beam grid, give quite an even imaging quality.

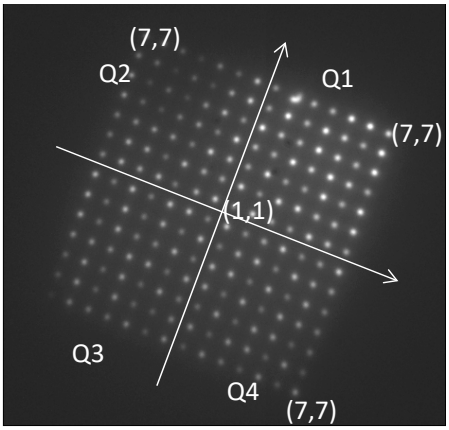

FIG 3. 8 Beams are labelled by four quadrants in the grid.

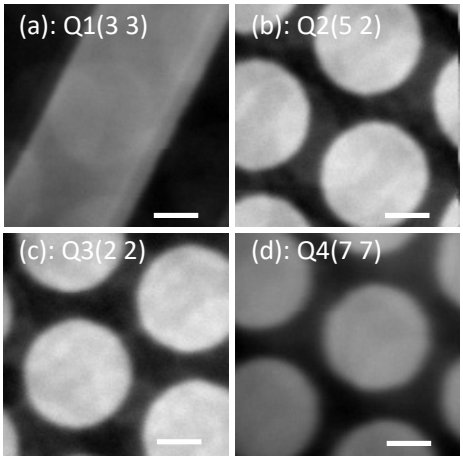

FIG 3. 9 Different beams' TE image using calibration sample. They are captured simultaneously and their FOV of images is 1.0 μm. Scale bars 200 nm.

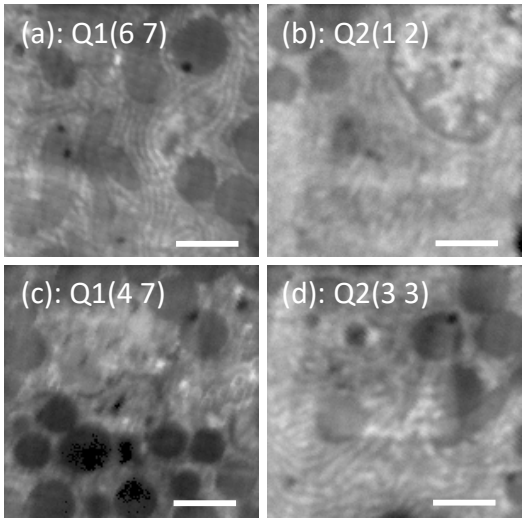

FIG 3. 10 Different beams' TE images using pancreas tissue captured simultaneously; they have FOV 4.0 μm with 20 nm pixel size. Scale bars 1 μm.

The image map is constructed by stitching the 196 TE images. In this process, beams' scan direction needs to be parallel with one side of E-beam grid. In principle, the scan FOV can be equal to the pitch of the E-beam grid on the sample so that no stitching program is needed afterwards, which is our goal. Then beam scan direction and scan FOV need to be accurately set. This can be done after several attempts on a certain working condition, and will easily be done when real time imaging is available. Currently, however, it takes too much time because off-line image processing is used. In this stage it is not necessary because we just intend to prove the working concept, not to deliver the perfect image map which is the goal of our imaging system in the future. Now we align the scan direction with the E-beam grid coarsely and set scan FOV to 10%-20% larger than the pitch of the E-beams on the sample, and then construct an image map using a stitching software called "TrakEM2" [14]. In this way, the beams' images may show slight rotation with respect to the beam array in the image map because the scan direction is not accurately aligned with one side of the E-beam grid on the sample. This is demonstrated in FIG 3. 12 and FIG 3. 13 which show image maps with 25 μm and 50 μm FOV, acquired by using different E-beam grid pitches on the sample. No stitching is applied in these two figures. This scan direction misalignment shows more clearly in the image map after stitching. In the stitching, the sub image overlap is set and the linear

blending fusion method embedded in the 'TrackEM2' is applied. The image map seems tilted at a small angle, leaving some dark area near the boundary of image map frame, as in FIG 3. 14 and FIG 3. 15 which show image maps biological tissue after stitching, with FOV 50 μm with 2600 × 2500 pixels. FIG 3. 14 has more misalignment between beams scan direction and one side of the E-beam grid so its image map has a larger dark area near the frame boundary.

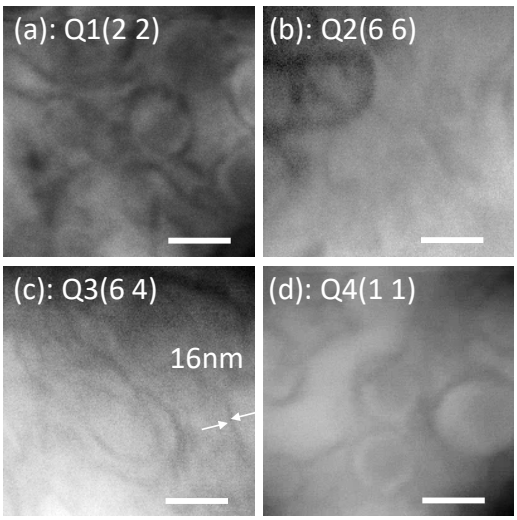

FIG 3. 11 Different beams' TE images using pancreas tissue re captured simultaneously; they have FOV 0.8 μm with 4 nm pixel size; details of 10-20 nm are visible in these images. Scale bars 200 nm.

3.5 Discussion

3.5.1 Present imaging speed and image size

In this chapter these results are used to demonstrate the principle of TE imaging. It now takes us about 20 min to finish one TE image map. The image maps with FOV 50 μm have 2600 × 2500 pixels. The pixel size in the image maps is around 20 nm. Clearly this is not yet high resolution and high throughput imaging. The following paragraphs explain briefly why we cannot achieve high resolution and high throughput imaging yet in our MBSEM.

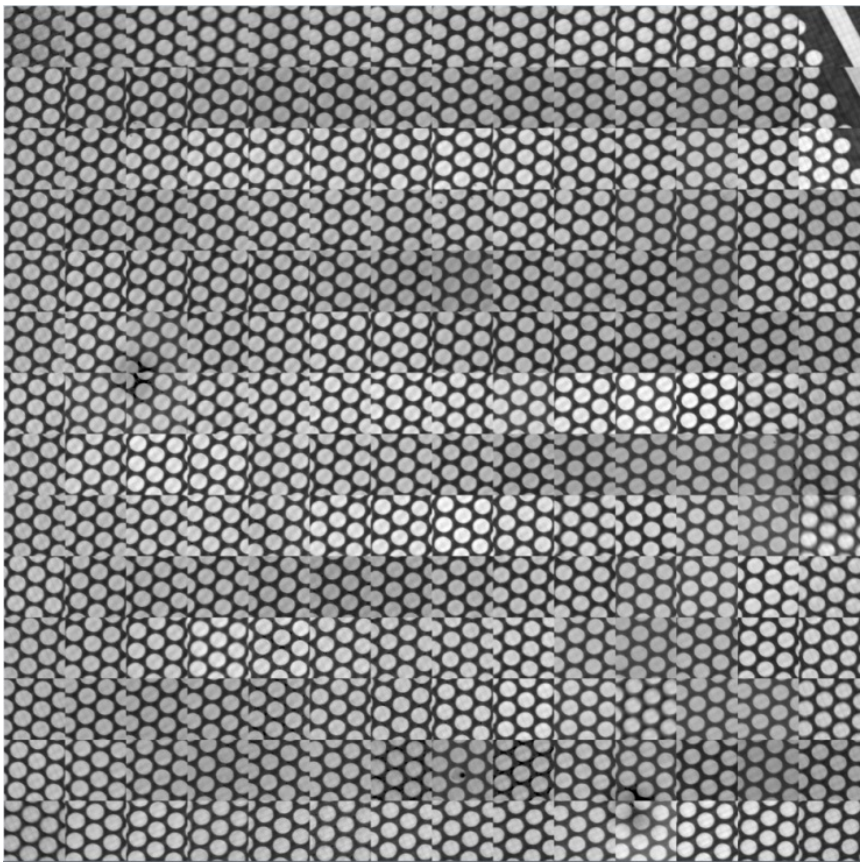

FIG 3. 12 TE image map of calibration sample formed by 14 × 14 sub-images using Delft MBSEM1, without stitching, FOV 25 μm with 2800 × 2800 pixels.

The GE680 camera is not very fast, just 240 FPS when the camera delivers an image of 400 × 400 pixels. When the beams' scan resolution is 200 × 200, it takes this camera 3 min. The image processing program takes about 17 min to analyze camera images and to construct TE images. These make the imaging speed low in the TE imaging system in the Delft MBSEM1, unsurprising considering that the off-line processing mode is used.

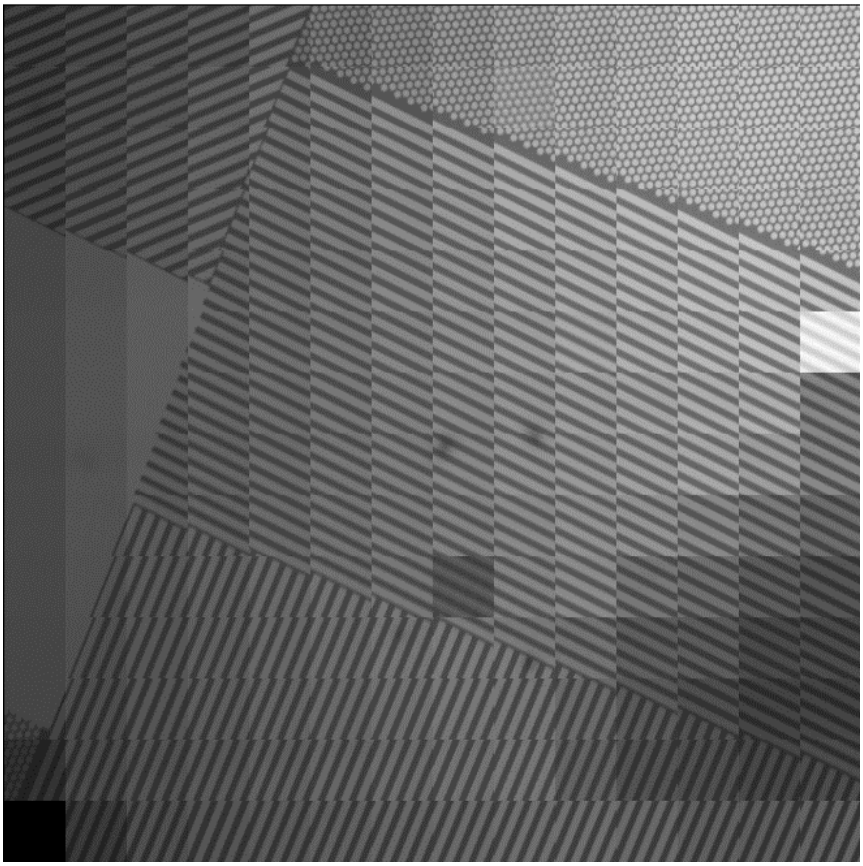

FIG 3. 13 TE image of calibration sample formed by 14 × 14 sub-images using Delft MBSEM1, without stitching, FOV 50 μm with 2100 × 2100 pixels.

In each scan step, the useful information that we really want is the 196 beams' intensities and positions. It is 588 Byte if each parameter takes 1 byte to record. However, in the off-line processing mode, the camera sends an image with 400 × 400 pixels with 8 bit depth to the computer. This is 160 kByte, 271 times more than what we need. If the beams' scan resolution is 200 × 200, the camera will generate 6.4 GByte data in one scan period although the useful information is just 23.5 Mbyte. Our current test program, based on LabVIEW, is capable of handling no more than 8 GByte data in one scan period. So the scan resolution cannot be set to be 500 × 500 if a camera image still has 400 × 400 pixels. This limited scan resolution makes large pixel size or scan step size in TE images even larger than the primary beam's spot size on the sample. For example, when a beam's scan FOV is 4 μm, each scan step is 20 nm using 200 ×

200 scan resolution, while the expected primary beam resolution is about 12 nm calculated in the simulation. The camera and the test program limit the size and imaging resolution in the image maps.

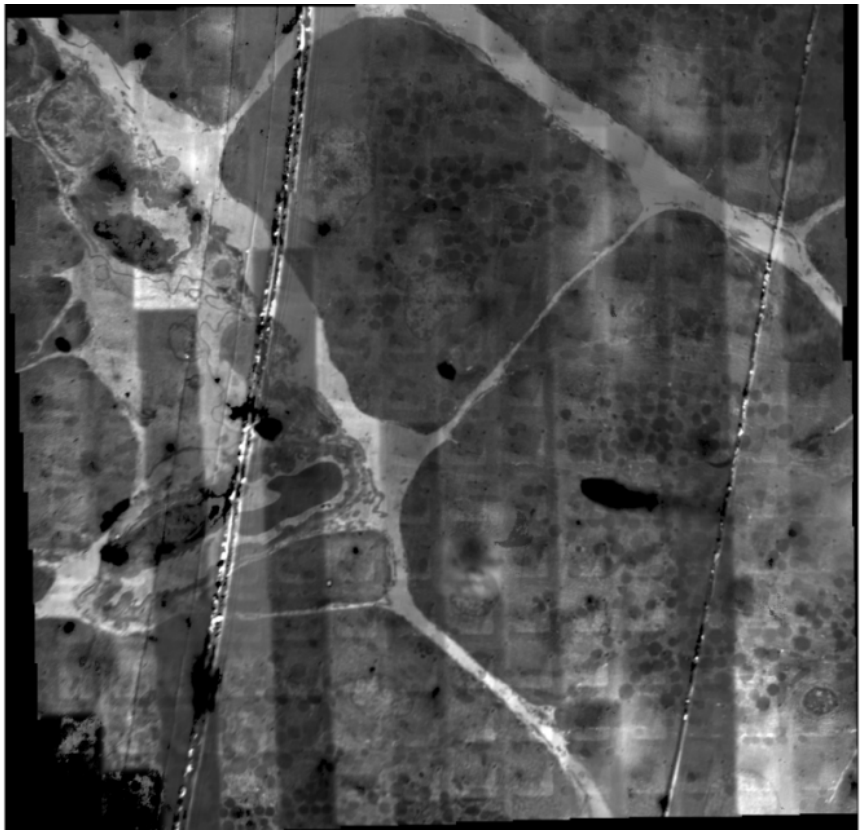

FIG 3. 14 TE image map 1 of pancreas tissue formed by 14 × 14 sub-images using our MBSEM, FOV 50 μm with 2600 × 2500 pixels. Sub-images are stitched using the software TrakEM2.

This low imaging throughput and small image size will be improved in the planned TE imaging system development. For example, in the second step, a faster camera, the Optronis CL600×2 CMOS, is used, which has 2000 FPS when each camera image has 512 × 512 pixels. Additionally, FPGA is used to process images much more rapidly. It is able to send 5.4 Gbyte per second from the CL600×2 camera to the frame grabber with on board FPGA (NI PCIe-1473R) via the FPGA camera link. The FPGA processes the camera images to generate the 196 beams' intensities and positions, and sends this useful information to a computer where TE images are constructed. Then it will take about 20 s - instead of 20 min -

to finish the image maps we had now, 60 times faster. The imaging throughput in the Delft MBSEM1 will then be higher than that of a single beam SEM, but still lower than that of the commercial MBSEM. However, it will allow a scan step smaller than the expected size of the primary beams so that the resolution can be measured and optimized. After the third development step, the fast real time imaging will be available and the Delft MBSEM1 should deliver the high resolution and high throughput TE imaging.

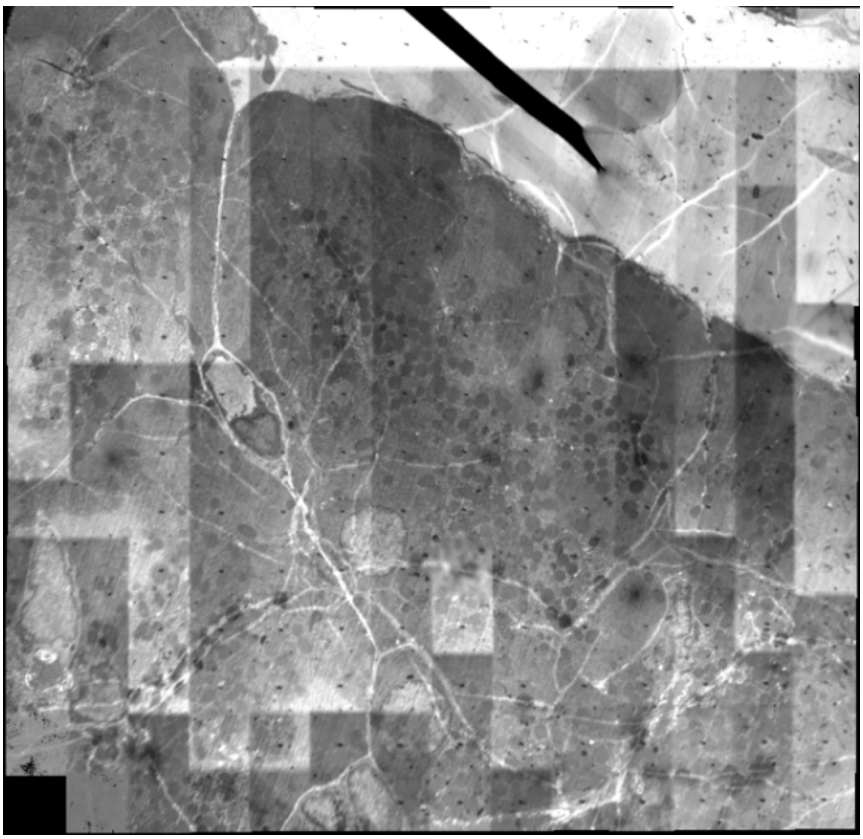

FIG 3. 15 TE image map 2 of pancreas tissue formed by 14 × 14 sub-images using our MBSEM, FOV 50 μm with 2600 × 2500 pixels. Sub-images are stitched using the software TrakEM2.

Although such limitations exist in our current imaging system, this test Labview program is already able to check fine features of the samples by setting a small FOV (smaller than the TE beams pitch on the sample). FIG 3. 11 shows four TE images with FOV 0.8 μm and examples of 400 × 400 scan resolution while the pitch of E-beam grid on the sample is 1.8

μm. The details of 10-20 nm size can be seen in these images. It would be premature at this time to state our MBSEM's imaging resolution because biological tissue itself and these images are not suitable for evaluating imaging resolution. Although we tried to deposit gold particles (the mixture of 5 nm gold particles, 15 nm gold particles and 50 nm gold particles) on a YAG disk to test resolution, the gold particles clustered together and it was not possible to test resolution at all. A special resolution test sample is needed to test resolution in this TE imaging system, for example, line or dots patterns with size of a few nanometers deposited on YAG using electron beam induced deposition (EBID) or similar microelectromechanical systems (MEMS) technology.

3.5.2 Intensity differences in image map

There are quite clear intensity differences among neighboring sub-images in the image maps. The possible causes of this non-uniformity are as follows:

- Different beams' currents due to contamination in the aperture lens array which splits the original beam into multiple beams. This would not be surprising after five years of using the same aperture plate.
- Misalignment in the MBSEM column, resulting in different beams being differently aligned on the variable aperture, thus selecting different currents.
- Some imperfection in the detection chain and the image processing

The first cause has already been proved by checking a sample without any pattern, such as pure YAG. When all primary beams come down to that sample without using any aperture in the column, quite a few beams' profiles are not round any more, but with irregular shapes. This tells us that some apertures of the ALA in the MBS are contaminated. This contamination needs to be verified by using a standard SEM. However, in order to take the aperture array out, the whole MBS needs to be disassembled. The MBSEM needs to be shut down at least for one month.

This verification is subsequently postponed until when the emission tip needs to be replaced.

The primary beams have a common crossover in the variable aperture plane so that apertures here are used to choose different currents. Because of the spherical aberration in the acceleration (ACC) lens (in this chapter, only the ACC lens is used to form the common crossover and the C2 lens is off), the off axis beams are shifted a bit away from the axis. After the variable aperture, the central portion of the axial beam is selected, but a different portion of the off axis beams is selected. Once the electron optics is fixed, these selections really depend on the position of the variable aperture. The misalignment, together with contamination in the aperture array, makes the current selection for off axis beams a bit unpredictable.

The optical microscope may make the off axis beams lose more photons than the axial beam. The uniformity of the camera pixels' output and the image processing program may also introduce some intensity difference even when the electron optical side is perfect. So an intensity match program is needed to eliminate or greatly reduce this non-uniform intensity inside the image map in the future.

3.5.3 Crosstalk influence

FIG 3. 16 shows the line profiles in two E-beam grids. It is obvious that there is crosstalk among neighboring beams even at 4 μm pitch. However, we cannot see the crosstalk effect contribution in sub-beam images. So in this chapter, we neglect the crosstalk influence, but we believe that when the e-beam grid pitch becomes close to the size of one beam inside the YAG, this influence will be problematic.

This crosstalk effect can be measured. For example, a single beam SEM and the Delft MBSEM1 image the same area in a sample using the same detection system. The single beam SEM image has the real sample information. The MBSEM image has the real sample information plus the crosstalk influence. Each pixel's intensity in the MBSEM image minus the corresponding pixel's intensity in single beam SEM image reveals the crosstalk influence. The deterioration of the imaging quality due to the crosstalk effect should be analyzed based on specific application.

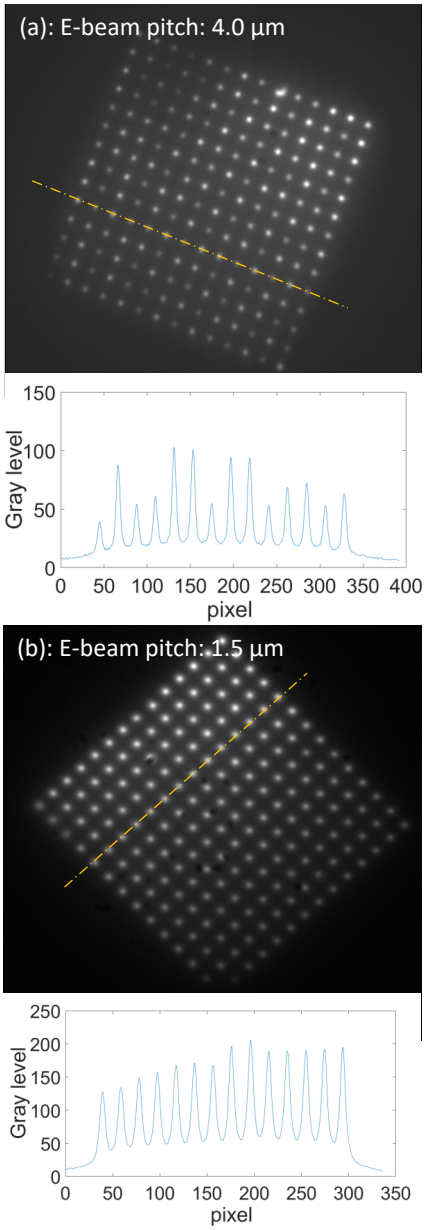

FIG 3. 16 Line profiles in E-beam grid with 4 µm pitch and 1.5 µm pitch. In (a), there are patterns on the YAG; in (b) there is no pattern on the YAG.

3.5.4 Sub-image boundary in image map

Some sub images' boundaries are apparent in the image maps, as can be seen in FIG 3. 14 and FIG 3. 15, even after different diffusion methods (such as linear blending, average, median, max intensity etc.) are tried in the TrakEM2. This is a common but very tough challenge in the stitching. So far it is popular to use automatic stitching with the help of manual stitching in the construction of image maps. However, as there are 196 sub-images generated in this MBSEM in one scan period, it is hardly possible to do manual stitching. A good automatic stitching program is expected to take a long calculation time. Meanwhile, we can make improvements by aligning the scan direction well with the e-beam grid direction and matching the scan FOV well with E-beam grid pitch.

3.6 Conclusion and outlook

This chapter provides one solution to achieve TE imaging in the Delft MBSEM1. In this image system, a YAG disk is adopted to convert the 196 TE beams to 196 photon beams; an optical microscope with high NA and good alignment with the electron optical axis is used inside the sample chamber to focus the 196 photon beams on to a camera with large magnification. An off line image processing program is used to retrieve each beam's transmission signal and construct images. A calibration sample and biological tissues are imaged to prove the working principle of this method.

Limited by the camera and the test Labview program, the imaging throughput is low, approximately 20 min to finish images of one scan period with low scan resolution (200 × 200). Our second step of TE imaging system development is underway and should deliver relatively fast (a few thousand scan steps per second) real time imaging with a faster CMOS camera "Optronis CL600×2" and a FPGA based image processing program. Our ultimate goal is to achieve rapid (100 ns scan dwell time) real time imaging using a super-fast camera (at least with 10 M FPS).

In the second and third development steps, the whole detection chain also needs to be optimized, such as the choices of the camera and the fluorescent material, the way to prepare the sample in the TE imaging

system in the Delft MBSEM1, etc.. The study of the imaging properties, including the image contrast, the detection quantum efficiency and the optimum imaging throughput, need to be carried on when the real time imaging is available.

The imaging resolution of TE images from the Delft MBSEM1 has not yet been measured because the proper resolution test sample needs to be prepared, preferably having a few nanometer scale patterns on a fluorescent material, but the details of 10-20nm in images of biological specimen are visible in the TE images. The intensity difference in the image maps is clearly shown in the image maps. In the future, elements such as the aperture array, the electron optics alignment, and image processing program need to be checked for correction. The crosstalk among neighboring beams in the E-beam grid is found in the experiments but is not clearly shown in the TE images. When the pitch of E-beam grid on the sample is close to the size of one beam in the YAG, it will give problems. Its influence in TE images should be analyzed in the future. A good stitching program and/or good control of the beam scan direction and scan FOV will be helpful in eliminating the sub-images' boundary in the image map.

3.7 Acknowledgements

The author acknowledge dr. Jacob Hoogenboom for advice on biological imaging, dr. Kees Hagen for discussions, Christiaan Zonnevylle for help with the SECOM platform and discussion on TE imaging system buildup, Ben Giepmans' group for biological tissue preparation, and Thomas Verduin, Paul Keijzer, Wilco Zuidema and Lennard Voortman for assistance with the image processing program.

3.8 References

[1]L. Reimer, *Scanning electron microscopy : physics of image formation and microanalysis* (Springer, 1998).

[2]J. Cazaux. Journal of Microscopy-Oxford **214**, 341 (2004).

[3]K. L. Briggman and D. D. Bock. Curr Opin Neurobiol **22**, 154 (2012).

[4]A. Takaoka and T. Hasegawa. J Electron Microsc **55**, 157 (2006).

[5]P. G. Merli and V. Morandi. Microsc Microanal **11**, 97 (2005).

[6]J. Kuipers, P. de Boer and B. N. G. Giepmans. Exp Cell Res **337**, 202 (2015).

[7]A. Mohammadi-Gheidari and P. Kruit. Nucl Instrum Meth A **645**, 60 (2011).

[8]Electron Optical Design v. E3.069.

[9]A. Mohammadi-Gheidari, C. W. Hagen and P. Kruit. J Vac Sci Technol B **28**, C6g5 (2010).

[10]L. Reimer, *Transmission electron microscopy : physics of image formation and microanalysis* (Springer, 1997).

[11]J. Orloff, *Handbook of charged particle optics* (CRC Press, 1997).

[12]A. C. Zonnevylle, R. F. C. Van Tol, N. Liv, A. C. Narvaez, A. P. J. Effting, P. Kruit and J. P. Hoogenboom. J Microsc-Oxford **252**, 58 (2013).

[13]S. Rahangdale, P. Keijzer and P. Kruit. in *2016 International Conference on Systems, Signals and Image Processing (IWSSIP)*. 1.

[14]Track EM2 v. 1.0c (2014) (Albert Cardona, Stephan Saalfeld;, ImageJ, 2014).

Chapter 4 Electron optics of secondary electron detection in the Delft MBSEM1

This chapter proposes a secondary electron (SE) detection system for the Delft MBSEM1. In this system, the SE beams are focused on a detection plane for separate collection, and the primary beams are focused on a sample simultaneously by the same electromagnetic lenses. An analytical model is built to prove the possibility of this SE detection system. One example is simulated in electron optical design (EOD) simulator, showing that the primary beams are focused on the sample and the SE beams are focused on the variable aperture plane with good separation. The flexibility in the control of the landing energy and the primary beams' pitch on the sample in the MBSEM with the SE detection system is analyzed. SE collection efficiency and crosstalk among the SE beams on the detection plane are discussed.

4.1 Introduction

In the course of the last 30 years many MBSEM systems have been proposed, most for maskless electron beam lithography [1-13], but only a few for imaging. Enyama *et al.* reported on building an MBSEM system with an imaging system [14], and Zeidler *et al.* introduced a 61 beam SEM with secondary electron (SE) detection.[15] However, the details of the SE detection optics were not presented. In this chapter, we discuss the electron optics design of the SE imaging system in the Delft MBSEM1, including some general features and limitations of SE imaging in a MBSEM.

There are two difficulties to build an SE imaging system in MBSEM. Firstly, the pitch of the SE beams in the sample, or the pitch of the primary beams on the sample, is usually small. The pitch is preferable to be smaller than 5 μm in the Delft MBSEM1; otherwise, the off-axis aberrations would deteriorate the uniformity and/or the current of the beams as shown in the simulation using the electron optical design (EOD)[16] package in Chapter 2. Secondly, the energy distribution and angular distribution of SEs are wide, from 0 eV to 50 eV in the

conventional definition, and from 0° to 90°[17,18] respectively. These two challenges need to be overcome to collect each SE beam separately.

This chapter introduces a solution to SE detection in MBSEM. Here we demonstrate it in the Delft MBSEM1, but this design principle can apply to any MBSEM. Theoretical analysis is done for the first order analysis. One example is simulated using the EOD package to prove the working principle. The flexibility of this SE detection strategy is obtained through variation of working distance (WD), the initial energy of the primary beams, and the combination of magnetic objective lenses. The SE detection efficiency in the Delft MBSEM1 is discussed, and an improvement plan is suggested.

As the Delft MBSEM1 is capable of correcting the field curvature, the off-axis beams have two types of the spot sizes in this chapter, one including the field curvature and the other not. The method of simulating the off-axis aberrations is the same as in Chapter 2.

4.2 Design principle

The SE imaging system in the Delft MBSEM1 should be able to collect each SE beam's signal separately and meanwhile to maintain good imaging resolution of the primary beams on a sample. The SE beams should be focused on a detection plane with a large pitch. The detection plane is preferable to be the variable aperture (VA) plane where the primary beams have a common crossover, shown in FIG 4. 1. There are two reasons. Firstly, the primary beams and the SE beams do not overlap in this plane so that the SE detection will bring little disturbance to the primary beams. Secondly, it is easy to insert a detector considering the mechanical structure of the SEM column. In the SE detection system, an electrostatic lens is needed to accelerate SEs generated on the sample and unavoidably to decelerate the primary beams. This electrostatic lens is called retarding lens and can be realized by biasing the sample stage negatively, forming a lens effect between the bottom pole piece of the magnetic objective lens and the sample stage. The retarding lens works with the magnetic objective lens to form an electrostatic-magnetic objective lens. The electrostatic lens can generate a proper energy difference between the primary beams and the SE beams so that one set

of electron optical lenses can focus the primary beams on the sample and focus the SE beams on the detection plane simultaneously. Such working strategy makes the Delft MBSEM1 compact.

The focusing of the SE beams can be treated like multi-beam emission microscopy[19-21] but with a worse resolution. The aberrations from the SE beams focusing will be significant because we intend to collect all SEs with 0 - 50 eV energy spread and 0 - 90˚ opening angle. The aberrations make the spot sizes of the SE beams big on the detection plane.

4.3 The first order analysis

4.3.1 Two subsystems

The Delft MBSEM1 with the SE detection system can be divided into two sub-systems, one for the focusing of the primary beams and the other for the focusing of the SE beams, shown in FIG 4. 1. The former subsystem is to focus the axial primary beam on the sample, done by the combination of the ACC lens, the C2 lens, the INT lens, the magnetic objective lens and the retarding lens. The latter subsystem is to focus the axial SE beam in the detection plane using the INT lens, the UHR lens, and the retarding lens. These two subsystems share the INT lens, the magnetic objective lens, and the retarding lens. The INT lens is to make the primary beams have a common crossover in the coma-free plane of the objective lens.[22]

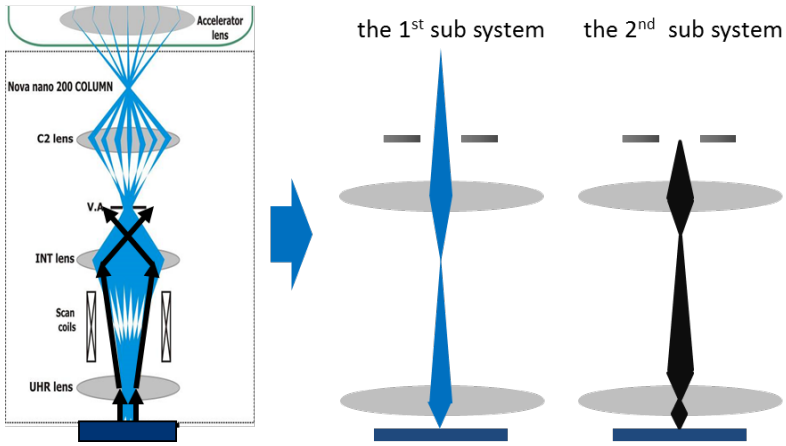

FIG 4. 1 The MBSEM with SE detection can be divided into two sub-systems. The first subsystem shows the focusing of the axial primary beam and the second subsystem indicates the focusing of the axial SE beam.

There are a number of variables, such as the primary beam energy before going through the retarding lens (PE energy), the working distance (WD), the potential of the sample stage, and the strength of the magnetic objective lens. The landing energy (LE) is calculated by the PE energy and the potential of the sample stage.

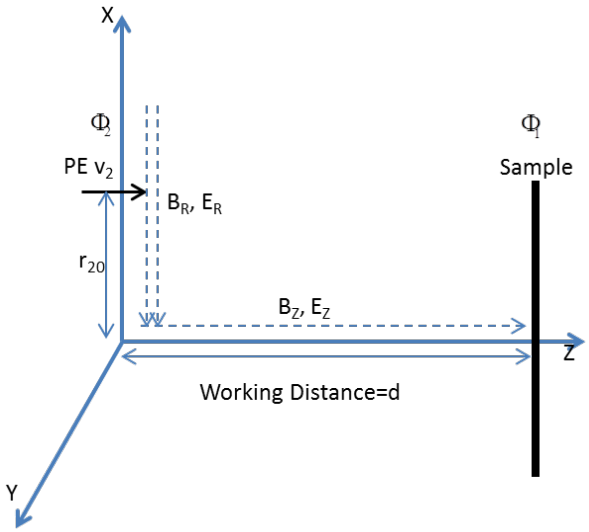

FIG 4. 2 The field distribution of objective lens on the sample in the first sub-system. B and E are the magnetic field and the electrostatic field of the electromagnetic objective lens, d the working distance; Φ_1 the potential in the pole piece; Φ_2 the potential on the sample.

We make a few assumptions to simplify the analysis. Firstly, the magnetic field and electrostatic field of the objective lens above the sample are block fields. Secondly, the coma-free plane of the objective lens coincides with the sample plane, because the working distance (a few mm) is negligible compared to the distance from the INT lens to the coma-free plane (200 mm). Thirdly, the SEs' initial velocity on the sample is zero because SEs' initial energies are very low compared to the energy gained from the retarding lens (a few keV). The axial primary beam and the axial SE beam are analyzed. Only the result is presented here, and the derivation can be found in Appendix A.

The first subsystem is elaborated in FIG 4. 2. Here we assume that the axial primary beam comes down parallel to the optical axis with a velocity of v_2 before entering the objective lens, considering that the

object distance is much larger than the focal length in the focusing contributed by the objective lens. So the INT lens can be omitted. The primary beam's velocity on the sample is v_1. Then, we get equation 4.1.

$$\pi - \frac{B_Z(v_2 - v_1)}{2E_Z} = \arctan(\frac{v_2 B_Z}{E_Z}) \qquad (4.1)$$

E_z can be represented by:

$$E_Z = \frac{(\Phi_2 - \Phi_1)}{d} = \frac{m}{2ed}(v_2^2 - v_1^2) \qquad (4.2)$$

where e and m are the charge and mass of electron; d is the working distance.

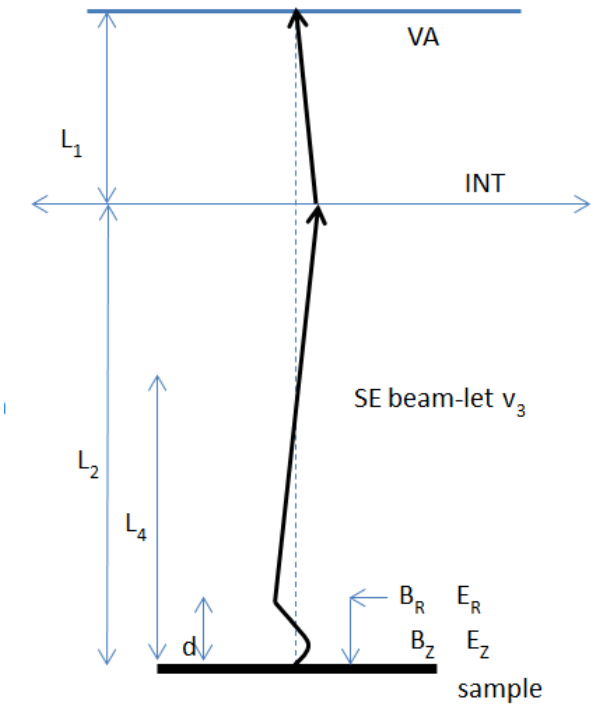

FIG 4. 3 The focusing of the axial SE beam from the sample to the VA plane in the second sub-system. L_1 is the distance from the VA plane to the INT lens, L_2 is the distance from the INT lens to the sample and L_4 the distance from the second crossover plane to the sample.

The second subsystem is elaborated in FIG 4. 3. In this subsystem, the SE beam has a velocity of zero on the sample and a velocity of v_3 after

passing the retarding lens; the SE beam has three times focusing from the sample to the detection plane. Then, we get equation 4.3.

$$\arctan\left(\frac{eE_Z[(L_2-d)(L_1-f_s)-L_1f_s]+2mv_3^2(L_1-f_s)}{ev_3B_Z[(L_2-d)(L_1-f_s)-L_1f_s]}\right)=\frac{B_Zv_3}{2E_Z}-\frac{3\pi}{2} \quad (4.3)$$

in which f_s is the focal length of the INT lens for SE beam's focusing and is a function of v_1 and v_3.

4.3.2 Discussion

These two equations can be used to check the SE detection concept. For example, we set the UHR lens and the sample stage's potential as variables, and all other parameters assigned, such as the PE energy and the working distance to be 15 keV and 3 mm. When the landing energy is 9470 eV, both the axial primary beams and the axial SE beam are focused, demonstrated in FIG 4. 4.

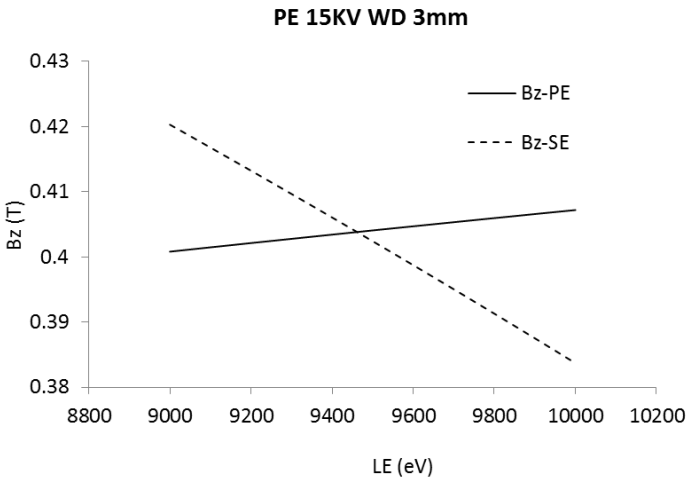

FIG 4. 4 A solution to focus the axial primary beam on the sample and to focus the axial SE beams in the detection plane simultaneously by solving the two equations derived from two sub-systems.

The first order analysis is helpful to understand the physical process and to prove the possibility that the primary beams and the SE beams can be focused simultaneously. However, it cannot give accurate solutions due to the assumptions to simplify the complicated system. Additionally, this analysis cannot show whether SE beams are separate on the detection plane. Simulation in the EOD gives the accurate solution.

4.4 Simulation

In this section, simulations are done to verify the working principle of the SE detection in the Delft MBSEM1. Section 4.4.1 uses an example to prove that the SE beams can be focused and separated in the VA plane while the PE beams have a good resolution on the sample. Section 4.4.2 shows the flexibility of the MBSEM with this SE detection system.

4.4.1 Simultaneous PE and SE focusing

In the example, the C2 lens is off, and the ACC lens makes the primary beams have a crossover in the VA plane. The INT lens makes the primary beams have another crossover on the coma-free plane of the objective lens. The UHR lens is the magnetic objective lens. The PE energy is 15 keV, and the WD is 5 mm. The VA plane is chosen as the SE detection plane. Such working condition should give a good optical performance, proved in Chapter 2. The UHR lens and the retarding lens are variables to make the primary beams, and the SE beams focused simultaneously. A paraxial approximation simulation is carried out firstly. Then, ray tracing for the SE beams' focusing is performed to check the separation of the SE beams in the VA plane.

a. Paraxial approximation simulation of the PE and SE focusing

In this simulation, the initial SE energy is assigned 5 eV on the sample. The UHR lens and the sample stage potential need to be set at 3442.34 ampere turns(AT) and 4243 V to achieve the primary beams' focusing and the SE beams' focusing simultaneously. Table 4. 1 presents the result in detail. The primary beams have a pitch of 0.37 μm on the sample and a landing energy of 10757 eV. The SE beams have a pitch of 87 μm in the detection plane. The spot size of the outermost primary beam is 1.48 nm. After the field curvature correction, it is reduced to 1.29 nm, just 0.04nm larger than the axial beam size. The opening angle is optimized to achieve the smallest spot size of the axial beam.

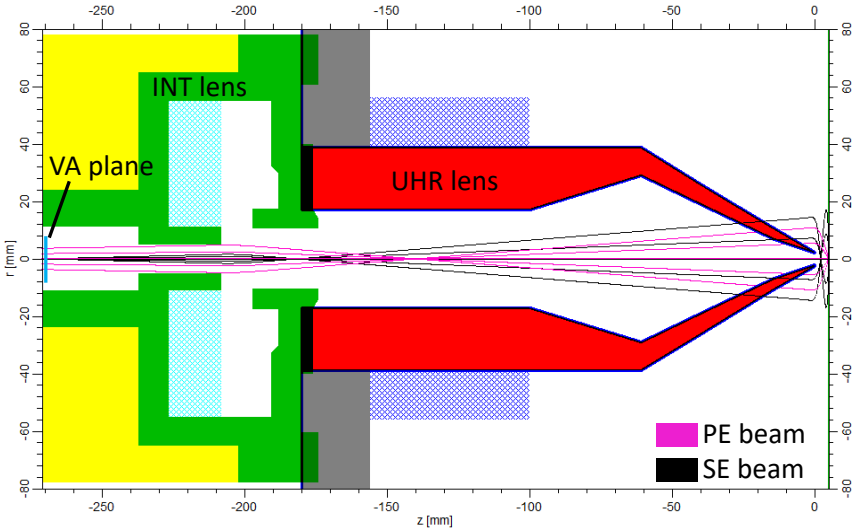

FIG 4. 5 Illustration of the axial PE beam focused on the sample and the axial SE beam focused on the VA plane. The PE energy is 15 keV, the C2 lens off, the UHR lens activated as the magnetic objective lens and the sample stage potential 4243 V. The SE beam has 5 eV initial energy and 10 mrad opening angle on the sample. Trajectories are scaled in the plot using the EOD.

Table 4. 1 The optical performance of the MBSEM in the example. The opening angle is chosen to have the smallest spot size of the axial primary beam.

*: the outermost PE beam's spot size after the field curvature correction

MBSEM with SE imaging	
PE beam focusing performance:	
PE energy (eV)	15000
Landing energy(eV)	10757
spot size (nm)	1.48
spot size_fc* (nm)	1.29
axial beam size (nm)	1.25
Probe current (pA)	27.66
PE pitch on sample (μm)	0.37
SE focusing performance:	
SE energy(eV)	4248
SE magnification	233
SE pitch(μm)	87.1

b. Ray tracing of SE focusing

The ray tracing for SE particles is done to check whether this 87 µm pitch is sufficient to separate the adjacent SE beams. Here 10,000 SE particles are used, shown in FIG 4. 6. They are generated based on the SE distribution described by H. Seiler.18 In this distribution, the SEs with 1 eV energy have the largest number. So the strengths of the lenses are re-calculated for an initial SE energy of 1eV in EOD. The sample stage potential changes to 4367 V and the UHR lens to 3435.92 AT. The VA plane is the check plane. A virtual square-cell grid with 5 µm cell size is used to display the SE distribution by counting SE numbers falling into each cell. A virtual ring detector (shown in FIG 4. 7) is used to describe the SE distribution in the VA plane.

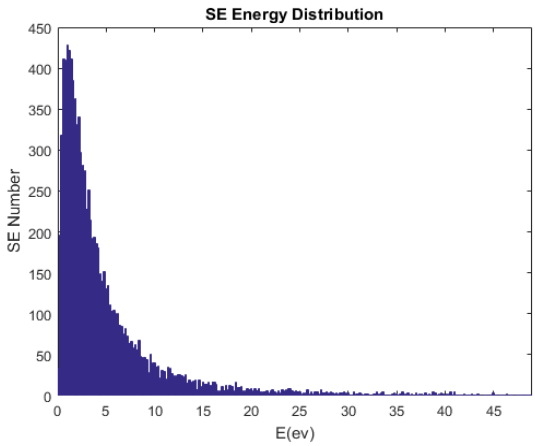

FIG 4. 6 The energy distributions of 10,000 SE particles on the sample.

Test 1: to simulate the axial SE beams with 10,000 particles. FIG 4. 7 shows that the SE distribution in the VA plane has a sharp peak and a very long tail. Different methods are used to evaluate this distribution. FW50 (Full Width containing 50% current) gives a spot size of 670 µm containing 5000 particles. It does not reflect what we observe in the plot (a) and (b). FWHM (Full Width Half Maxima) gives a spot size of 10 µm containing 233 particles. FW10%M (Full Width 10% Maxima) produces a spot size of 20 µm containing 419 particles. A virtual detector with a size of one pitch (87 µm) collects 1287 particles. This 13% SE collection efficiency is comparable to Everhart-Thornley detector collection efficiency.[23]

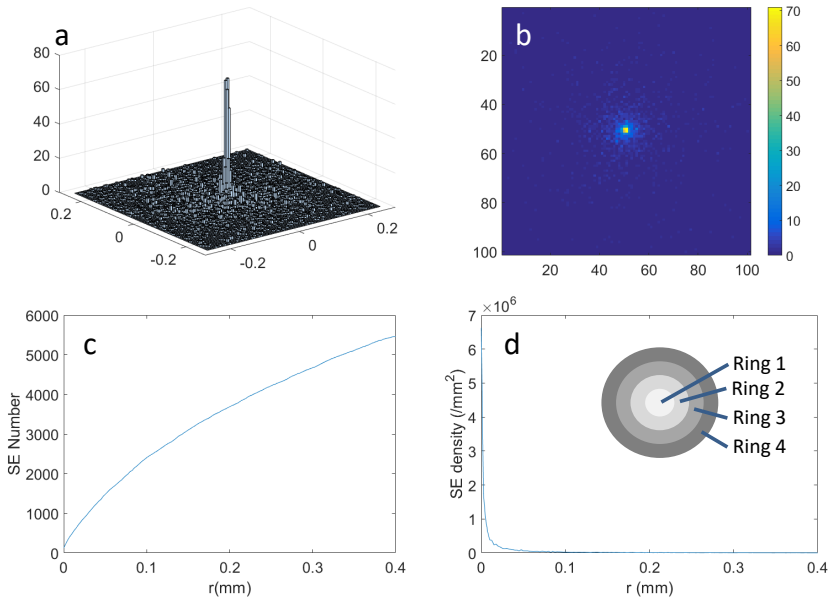

FIG 4. 7 Plot (a) and plot (b) display the SE distribution in the VA plane with the cell size of 5 μm. X and Y axis in the plot (a) give the real location positions; X and Y axis in the plot (b) show the indexes of the cells. The intensity scale in the plot (b) shows electron numbers in one cell; plot (c) shows the total SE numbers along with the r distance; plot (d) shows the SE density in each ring along with the r distance, using 2.5 μm ring step size.

HWHM and FW10%M results are much influenced by choice of ring step size, demonstrated in Table 4. 2. FW10%M defines a spot size of 2 μm when the ring step size is 0.2 μm while a spot size of 20 μm when the ring step size is 2.5 μm. This difference should come from the insufficient number of SE particles used. Small step size should be preferred when sufficient particles are used. As it already takes the EOD program 4 hours to simulate 10,000 particles, we do not use more particles in our simulation.

Table 4. 2 The spot size of the SE beam in the VA plane D_p varies with the ring step size and the evaluation methods. 'SE No.' means the number of SEs contained in the correspondent spot size.

Ring_step	2.5(μm)		1(μm)		0.5(μm)		0.2(μm)	
	Dp(μm)	SE No.	Dp(μm)	SE No.	Dp(μm)	SE No.	Dp(μm)	SE No.
FW50	675	4999	678	4999	680	5000	680	5000
FWHM	10	248	4	119	2	67	0.8	26
FW10%M	20	419	8	200	5	141	2	67
Pitch	87	1314	87	1314	87	1295	87	1287

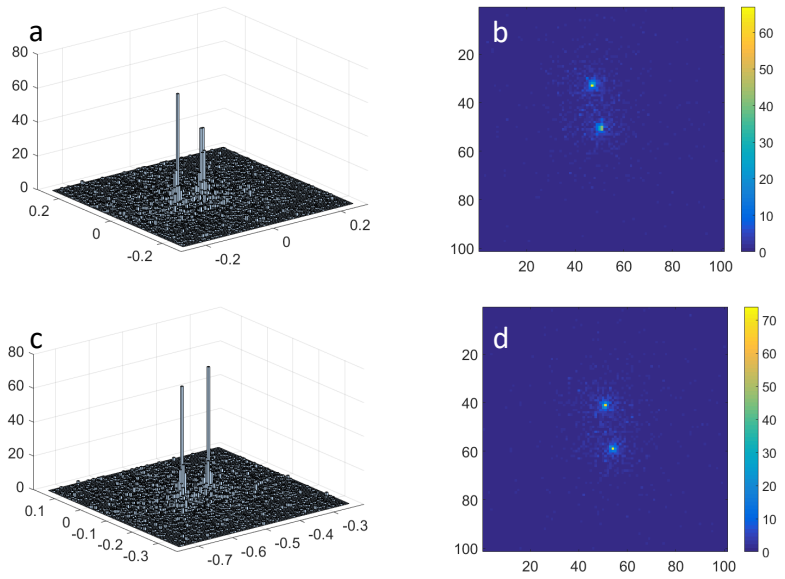

FIG 4. 8 Plot (a) and plot (b) show the distribution in the VA plane of two SE beams with the cell size 5 µm, the axial beam and a beam which is one pitch away. In the plot (b), the lower beam is the axial SE beam; plot (c) and plot (d) show the distribution in the VA plane of two SE beams with the cell size 5 µm; the outermost beam and a beam that is one pitch inside. In the plot (d), the upper beam is the outermost SE beam. X and Y axis in the plot (a) and plot (c) give real location positions; X and Y axis in the plot (b) and plot (d) show indexes of the cells.

Test 2: to simulate two SE beams. The plots (a) and (b) In FIG 4. 8 show two SE beams, the axial SE beam and the other from one pitch (0.37 µm) away. Each beam has 5000 particles. The peaks of these two SE beams are separate in the VA plane. Their peak-to-peak distance is measured to be about 91 µm, which fits the simulation result (87 µm) well. The plots (c) and (d) show another two SE beams; one is an outermost beam, 2.4 µm off axis, and the other is from one pitch inside. Each has 5000 particles. Peaks of these two SE beams are still separated in the VA plane. The peak-to-peak distance is measured to be 91µm. It can be concluded from these two cases that the peaks of all SE beams will be separate in the VA plane. Crosstalk among the SE beams in the VA plane might be an issue for the SE imaging. Test 1 clearly shows that the distribution of the axial SE beam in the VA plane has a sharp peak with very long tail and that one-pitch-size detector collects 13% of SEs emitted from the sample. The other SEs spread out to a large area. When the axial SE beam and four closest neighboring SE beams (one pitch away) are counted, there are 384 particles collected in the axial SE

beam's one pitch size detector, 30% more. We are not sure about how bad this will contribute to final SE images. The influence depends on the degree of the crosstalk, and may also depend on the specific application. In this chapter, the crosstalk will be discussed but its influence not.

Test 3: to simulate 196 SE beams, using one particle for one beam to check the distortion contribution. FIG 4. 9 shows the distribution of these 196 particles in the VA plane. We do not see obvious distortion. The pitch is measured to be 91 μm.

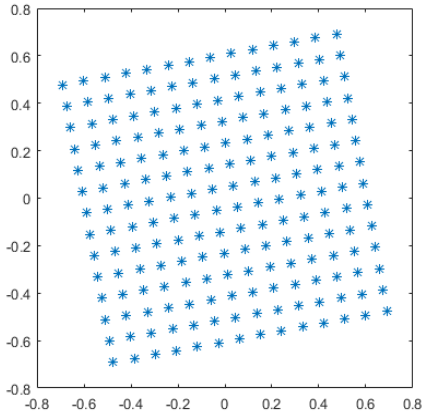

FIG 4. 9 196 SE beams in the VA plane, one particle in each SE beam.

c. Discussion

The spot size of a SE beam in the VA plane is composed of all types of aberrations and the geometrical spot size of the SE beam. The following paragraphs explore how much the aberrations and the SE geometrical source size contribute in the spot size in this example.

The SE geometrical source size in the VA plane is calculated by multiplying the SE virtual source size by the magnification of the SE focusing. So firstly the virtual SE beam size needs to be found. The SE particles with the different energies and the opening angles are accelerated and focused by the electron optical lenses after emitted out of the sample. If the trajectories of these particles are traced back when only acceleration field effect is considered, a virtual SE source size can be found. [19-21]

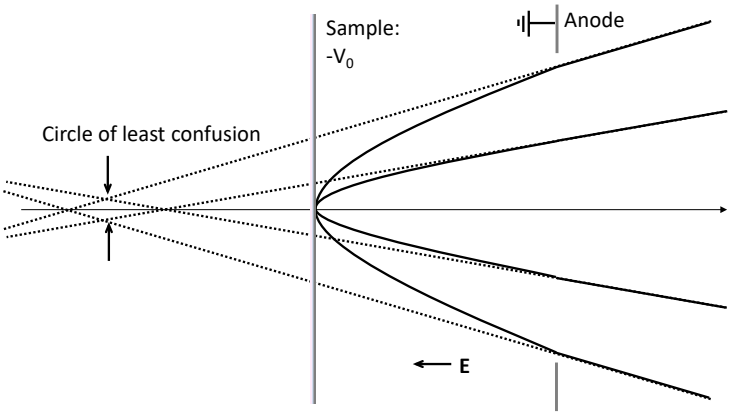

FIG 4. 10 Illustration of getting the virtual source size of the SE beams.

As all SEs arrive at the VA plane, this analysis uses 10,000 SE particles with the same energy distribution shown in FIG 4. 6. A virtual ring detector is used to analyze the distribution in the virtual source plane, shown in FIG 4. 11. The radius' increment is 2 nm.

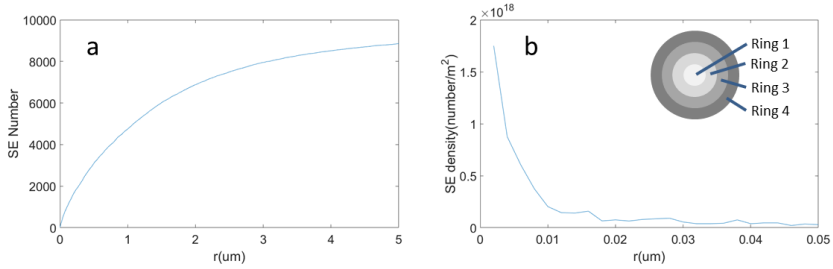

FIG 4. 11 Plot (a) is the total SE number along with r distance; plot (b) is the SE density distribution along with r distance. The radius' increment of rings is 2 nm.

FIG 4. 12 shows the formation of the SE beam's spot size in the VA plane. When FW50 is used, the effective SE virtual size is a 2 μm diameter spot in the sample. It results in a 466 μm spot in the VA plane due to the SE focusing magnification of 233 times. The total aberrations contribute about 28.5% in the outermost SE beam spot in the VA plane. FW25 (Full Width containing 25% current) gives the effective SE virtual size of 0.74 μm and a spot of 172 μm in the VA plane; the total aberrations contribute about 25.8%. When FW13 (Full Width containing 13% current) is used, the total aberrations contribute about 25.0%. So, in

the example, the SE virtual source size is dominant in the spot size of the outermost SE beam in the VA plane.

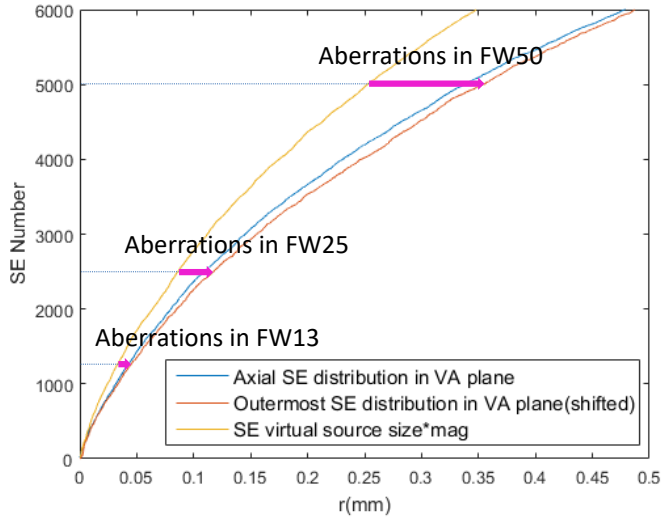

FIG 4. 12 The analysis of the spot size of the SE beams in the detection plane. The plot shows the spot size curves of the virtual source of the SE beams, the axial SE beam, and the outermost SE beam. The pink arrows show the aberration contributions in different evaluation methods.

FW50 and FW25 or even FW13 are not proper to describe the simulation result shown in FIG 4. 8 where the two SE beams seem clearly separated. However, the discussion here is important when the crosstalk effect is concerned. When zero crosstalk is desired, the SE beam's pitch in the sample or the primary beams' pitch on the sample should be larger than the SE virtual source size defined by FW100 (Full Width containing 100% current). In this example, the pitch of the SE beams in the sample is 0.37 μm, smaller than the FW100 value of the virtual source size which is larger than 0.4 mm. Such fact means that the crosstalk among the SE beams already exists inside the sample and cannot be reduced and will be enhanced in the following SE focusing system due to the aberrations.
Table 4. 3 shows the contribution of the SE virtual source size to the spot size of the axial SE beam in the detection plane using FWHM and FW10%M. We can get the same conclusion: in this example, it is the geometrical spot size that dominates the spot size of the axial SE beam in the VA plane, not the aberrations.

Table 4. 3 The contribution of the virtual source to the spot size of the SE beam in the detection plane using FWHM and FW10%M. The virtual ring detector's step size in VA plane is 0.5 μm, and the step size in the SE virtual source size plane is 2nm. This result shows that the virtual source size dominates the spot size of the SE beam in the VA plane.

	SE spot in the VA plane		Caused by virtual SE source	
	Size (μm)	SE Number	Size (μm)	SE Number
FWHM	2	67	1.86	48
FW10%M	5	141	4.5	115

To sum up the simulation results of the example:

- The SE beams are focused with a pitch of 87 μm in the VA plane; meanwhile, the primary beams are focused well on the sample with a resolution of 1.48 nm for the outermost beam and a pitch of 0.37 μm on the sample.
- The axial SE beam distribution in the VA plane has a sharp peak and very long tail. FW10%M gives a spot size of 20 μm with 419 particles. A round detector with one pitch size collects 13% of all particles. The spot sizes of the SE beams in the detection plane are dominated by the SE geometrical spot size, not by the aberrations in this example.
- The peaks of the 196 SE beams in the detection plane are separated with a measured pitch of 91μm.
- No clear distortion of SE beams observed on the detection plane.

4.4.2 The flexibility in the MBSEM with SE detection

As the SE beams are required to be focused, this SE detection strategy in the Delft MBSEM1 has less freedom than the SE detection in a single beam SEM where the landing energy and the working distance are chosen freely and separately. This section is to explore the flexibility of the control of the landing energy and the control of the primary beams' pitch on the sample in the Delft MBSEM1 with the SE detection. The analysis is done via three variables, the WD, the PE energy and the different magnetic objective lenses. In the analysis, the ACC lens is used to form a common crossover in the VA plane, and the C2 lens is off.

a. Working distance

Here the PE energy is fixed at 15 keV, and the UHR lens is activated as the magnetic objective lens. The INT lens used to form a crossover in the coma-free plane of the objective lens. Such working condition can deliver a good resolution, proved in Chapter 2. When the WD is different, the coma-free plane changes and so does the strength of the INT lens.

In FIG 4. 13, when the WD varies from 1 mm to 15 mm, the landing energy needs to be set from 8100 eV to 12300 eV. The pitch of the primary beams on the sample changes from 0.12 μm to 1.22 μm, and the pitch of the SE beams in the detection plane from 34 μm to 201 μm. The spot size of the axial primary beam changes from 0.6 nm to 2.9 nm. The spot size of the outermost beam after the field curvature correction is close to the spot size of the axial beam, except when the WD is 1mm. This exception can be explained as follows. As the UHR lens is the immersion lens that has low efficiency, its excitation is strong when the WD is 1mm, 3.5 times stronger than the excitation when the WD is 5mm. Such strong lens field leads to large off-axis aberrations. For example, the coma is 1.46 nm, 2.5 times of the spot size of the axial beam's spot size, even though the coma-free plane concept is used to minimize it.

When the WD is 3 mm, the landing energy is 9870 eV, which is not much different with the energy 9470 eV obtained in Sec 4.3. This simulation result proves that our analytical model works well.

FIG 4. 13 shows that the smaller the WD is, the lower the landing energy is and the smaller the pitch of the SE beams in the detection plane is. So, it is nearly impossible to achieve a landing energy lower than 8100 eV in this way. Even though the WD can be smaller than 1 mm, bringing a little lower landing energy, it will be difficult to separate the SE beams because the pitch of SE beams in the detection plane decreases.

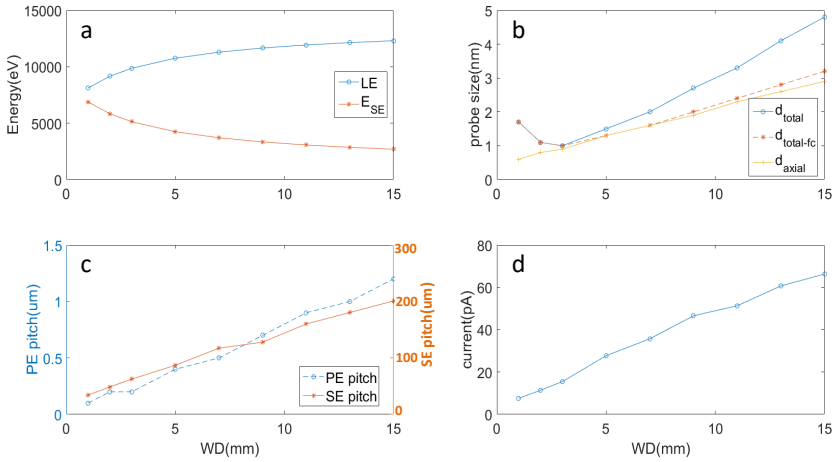

FIG 4. 13 The properties of the MBSEM under the different working distances when primary beam energy is 15KeV, and the UHR lens activated as the magnetic objective lens. Plot (a) to (d) show the change of the energies, the spot size, the pitches, and the beam current (the opening angles are optimized to have the smallest axial probe sizes). B_r is 5×10^7 A/(m^{2}srV) in the current calculation.

b. Primary beam energy

In this part, we set the UHR lens as the magnetic objective lens and the WD 3mm.

FIG 4. 14 plots the results. When the PE energy varies from 3 keV to 15 keV, the landing energy changes from 2030 eV to 9870 eV. The pitch of the primary beams on the sample changes from 0.33 μm to 0.23 μm, and the pitch of the SE beams in the detection plane from 98.8 μm to 62.5 μm. The spot size of the outermost beam without the field curvature correction is close to the spot size of the axial beam, from 2.7 nm to 1.0 nm. Coulomb interaction is not taken into account in the simulation.

It is quite straightforward that the low PE energy brings the low landing energy. A few hundred electron-volt landing energy may require lower than 1 keV PE energy. Such working condition will not be preferred in any SEM because the primary electron beam needs to travel in the SEM column (about 400 mm long) with this low energy. Besides, the low PE energy leads to a low SE energy in the detector. For example, when the PE energy is 3 keV, the SE energy is only 970 eV, which limits the options of the SE detector and may reduce the detection efficiency of the SE imaging system.

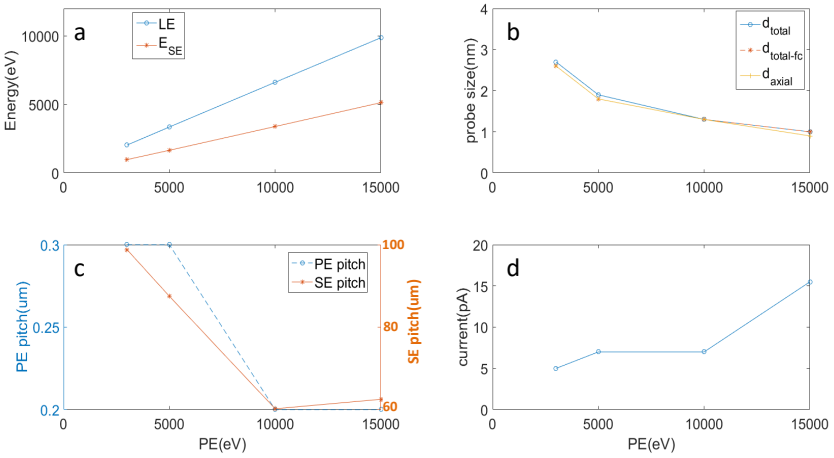

FIG 4. 14 The properties of the MBSEM under the different primary beam energies when the UHR lens activated as the objective lens and working distance 3mm. Plot (a) to (d) show the change of the energies, the spot size, the pitches, and the beam current (the opening angles are optimized to have the smallest axial probe sizes).

c. Combination of the HR lens and the UHR lens

In the Delft MBSEM1's column, there are two magnetic objective lenses, the HR lens, and UHR lens. The HR lens has enclosed magnetic field, and the UHR lens produces an immersion field. Only one lens out of these two is activated in the normal SEM operation. Here the combination of the HR lens and the UHR lens is used as the magnetic objective lens to gain more flexibility. In this section, the PE energy is15 keV, and the WD is 3mm. When the combination of the HR lens and the UHR lens changes, the coma-free plane shifts. So the INT lens changes correspondingly.

In FIG 4. 15, the excitation of the HR lens is chosen as the X axis, although both of the lenses are working in the most cases. The excitation of the HR lens is 672 Ampere-Turn (AT) when the UHR lens is off. When the HR lens turns strong, the primary beams' pitch on the sample increases a bit, while the SE beams' pitch in the detection plane drops dramatically. For example, the SE beams' pitch in the detection plane is 62.6 μm when the excitation of the HR lens is 0, while the SE beams' pitch drops to 24.5 μm when the excitation of the HR lens is 330AT. The phenomenon can be explained as follows. The magnetic field of the HR lens sits between the INT lens and the UHR lens. After the SEs have a

crossover inside the UHR lens and travel away from the optical axis, the HR lens pushes the SEs back to the optical axis and therefore limits the SE magnification in the detection plane. The SE beams' pitch in some combination is even worse than in the case of only the HR lens activation. Additionally, the strong HR lens in the combination brings large off-axis aberrations and decreases the uniformity of the primary beams.

To sum up, the Delft MBSEM1 with the SE detection has limited capability to control the landing energy and the pitch of the primary beams on the sample. Although the control is not as flexible as in a single beam SEM, it is already good enough for us to start experiments in the Delft MBSEM1.

One notice is that the limited control of the landing energy is only valid when the SE detection is activated in the Delft MBSEM1. In the transmission electron (TE) imaging mode, the landing energy can be set freely by biasing the sample stage negatively.

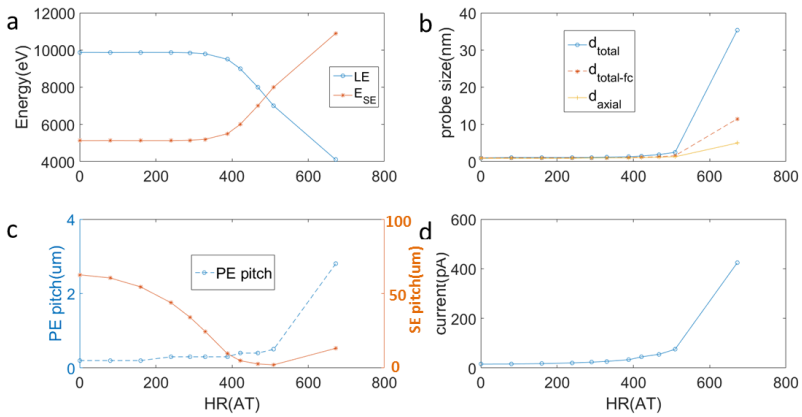

FIG 4. 15 The properties of the MBSEM under the different combinations of the HR lens and the UHR lens combination when the primary beam energy is 15 keV and working distance 3 mm. Plot (a) to (d) show the change of the energies, the spot size, the pitches, and the beam current (the opening angles are optimized to have the smallest axial probe sizes).

4.5 Discussion

Collection efficiency is important in an imaging system. The collection efficiency in the Delft MBSEM1 is defined as: the collected electrons of an SE beam using a one-pitch size detector in the detection plane over all electrons of this SE beam. The collection efficiency firstly matters to the

imaging throughput. A detection system with low collection efficiency needs a long scan dwell time to obtain an image with proper signal noise ratio (SNR), and thus has low imaging throughput. For example, the detection efficiency of an in-lens detector in a single beam SEM can be close to 100% if a strong retarding lens is used to accelerate all SEs into the SEM column. When the SE detection efficiency in the Delft MBSEM1 is 13%, the imaging throughput of our MBSEM only increases 25.5 times, even though there are 196 primary electron beams. The advantage of multiple beams in the column is compromised. Secondly, a collection efficiency of less than 100% in our MBSEM brings crosstalk effect. The secondary electrons that are not collected by their detector fly to other beams' detectors. The study on the influence of the crosstalk effect on SE images needs to be done in the future.

A high electrical field above the sample can improve the collection efficiency, proved in FIG 4. 16, which plots the collection efficiency in the combinations simulated in Section 4.4.2 where the WD varies to gain the flexibility. When the WD is 15 mm, the electric field above the sample is the weakest, only 180 V/mm. Although the pitch of the SE beams in the VA plane is 201 μm, the largest pitch of the SE beams in this chapter, the SE collection efficiency is only 7.2%. When the WD is 1 mm, the electric field is 6880 V/mm above the sample. The SE collection efficiency is 19.4% with a pitch of 34.2 μm in the VA plane.

Here we briefly explain the influence of the electrical field. In the analysis in Sec 4.4.1, the SE virtual source size is largely determined by the electric field above the sample, not by the potential difference between the pole piece of UHR lens and the sample, demonstrated in FIG 4. 17. When the electric field becomes stronger, for example, from 1 kV/mm to 10 kV/mm, the virtual source using FW50 drops from 1.8 μm to 0.18 μm. Such results agree well with the analysis of virtual source size done for the emission microscopy which shows the virtual source size is inversely proportional to the electric field above the sample[24,25]. If the pitch of the primary beams on the sample can be maintained or does not drop as much as the virtual source size does, the collection efficiency will become higher and the crosstalk effect weaker. However, it is difficult or impossible to reduce the SE virtual source size while maintaining the pitch on the sample by only biasing the sample stage.

Adding electrodes between the pole piece of the magnetic objective lens and the sample may ease the difficulty.

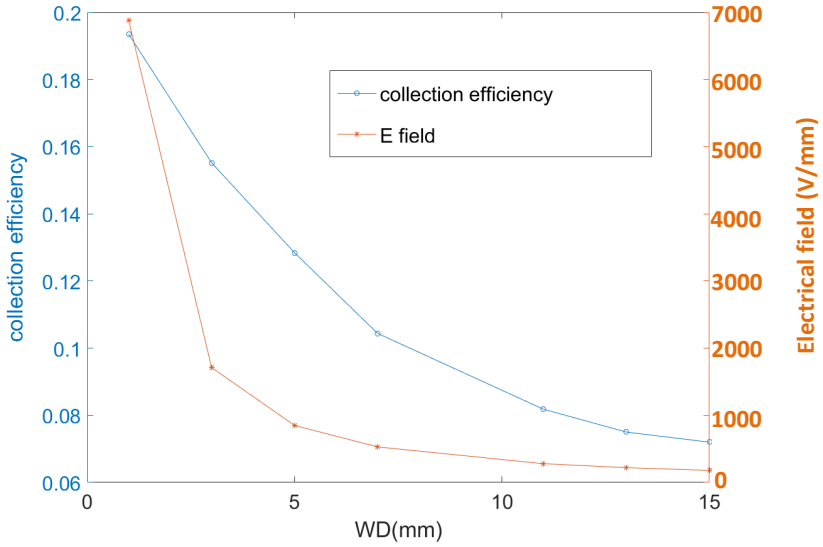

FIG 4. 16 SE collection efficiency and the electrical field above the sample when the working distance is changed to gain the flexibility in the Delft MBSEM1.

If 100% collection efficiency or zero crosstalk is desired, the modified retarding lens with the high electric field above the sample may not be sufficient because the aberrations will show up. In FIG 4. 12, the SE virtual source size contributes 500 μm, and the aberrations add about 200 μm to the SE spot size on the detection plane using the FW50 method while the SE beams' pitch is only 87 μm in the EOD simulation. The contribution of the aberrations evaluated by the FW50 is about 2.2 times the pitch. So, to achieve 100% collection efficiency or zero crosstalk, firstly, the high electric field needs to be used to reduce the SE virtual source size. Secondly, the aberrations in the SE focusing system need to be optimized. If these two steps still cannot make zero crosstalk in the detection system, a new version of the MBSEM with a large primary beams' pitch on the sample will need to be designed.

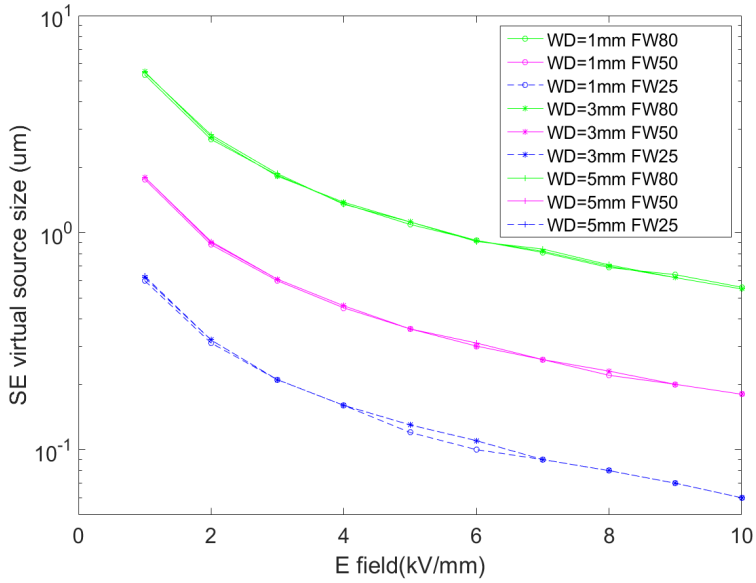

FIG 4. 17 The electrical field above the sample largely influences the SE virtual source size.

4.6 Conclusion and outlook

In this chapter, a SE detection system is proposed for the Delft MBSEM1. In this system, the SE beams are focused separately in a detection plane; meanwhile, the primary beams are focused on the sample. The sample is negatively biased to accelerate the SEs into the column. A proper energy difference between the SE beams and the primary beams allows us to use the same lenses in the SEM column to achieve these two types of focusing simultaneously. This detection system does not need much mechanical modification and keeps the whole column compact.

Theoretical analysis is done to prove the working principle after a few assumptions for simplification. The results of an example simulated in EOD show that the outermost primary beam has a spot size of 1.48 nm and the axial primary beam has a spot size of 1.25 nm, while the SE beams are focused separately in the detection plane with a pitch of 87 μm. The distortion of the SE beams grid in the detection plane is hardly seen. The distribution of the SE beams in the detection plane has a sharp peak and very long tail. The axial SE beam has a spot size of using 20 μm using FW10%M. Its collection efficiency is about 13% by employing a one-pitch size detector. In this example, the crosstalk among the SE

beams exists. The study of the virtual SE source size shows that the crosstalk initially happens among the virtual SE sources inside the sample and cannot be corrected in the SE focusing system. A strong electrical field above the sample is helpful to improve the collection efficiency and the crosstalk effect among the SE beams. Evaluation of the crosstalk effect in SE imaging is not implemented in this chapter, but it needs to be done in the future. If zero crosstalk or 100% collection efficiency are required, we may need to design a new version of MBSEM to have a large pitch of the primary beam on the sample.

The SE imaging system in the Delft MBSEM1 has limited flexibility by varying working distance, the primary beam energy and the combination of the HR lens and the UHR lens separately. It is not recommended to have SE images using low landing energy in the Delft MBSEM1. This limitation originates from the requirement that the same lenses need to focus the primary beams and the SE beams simultaneously.

Notwithstanding these imperfections, the Delft MBSEM1 should get SE images using this detection system for certain working conditions. Our further step is to get SE images of 196 beams in experiments.

4.7 References

[1]O. Kamimura, S. Tanimoto, H. Ohta, Y. Nakayama, M. Sakakibara, Y. Sohda, M. Muraki, S. Gotoh, M. Hosoda, Y. Someda, K. Tamamori, F. Hirose, K. Nagae, K. Kato and M. Okunuki. Journal of vacuum sciences technology B **25**, 140 (2007).

[2]T. H. P. Chang, M. Mankos, K. Y. Lee and L. P. Muray. **58**, 117 (2001).

[3]M. Okunuki, I. Shimoda, M. Miyawaki, T. Tsukamoto, A. Suzuki, T. Kaneko, T. Takeda and M. Seki. Multi-electron-beam pattern drawing apparatus. (1990).

[4]P. Adamec, R. Degenhardt, H. P. Feuerbaum, H. Munack and D. Winkler. Multi beam charged particle device. (2005).

[5]C. W. Lo and X. Jiang. Method and apparatus for multiple charged particle beams. (2007).

[6]E. Platzgummer. Proceedings of SPIE **7637**, 763703 (2010).

[7]M. J. Wieland, G. de Boer, G. F. ten Berge, M. van Kervinck, R. Jager, J. J. M. Peijster, E. Slot, S. W. H. K. Steenbrink, T. F. Teepen and B. J. Kampherbeek. 76370F.

[8]Y. Zhang and P. Kruit. Journal of Vacuum Science & Technology B: Microelectronics and Nanometer Structures **25**, 2239 (2007).

[9]N. W. Parker, A. D. Brodie, G. X. Guo, E. M. Yin and M. C. Matter. Electron optics for multi-beam electron beam lithography tool. (2003).

[10]E. Yin, a. D. Brodie, F. C. Tsai, G. X. Guo and N. W. Parker. Journal of Vacuum Science & Technology B: Microelectronics and Nanometer Structures **18**, 3126 (2000).

[11]M. A. McCord. Journal of Vacuum Science & Technology B: Microelectronics and Nanometer Structures **15**, 2125 (1997).

[12]L. Han and M. A. McCord. Electron beam inspection system using multiple electron beams and uniform focus and deflection mechanisms. (2004).

[13]T. H. P. Chang. Journal of Vacuum Science & Technology B: Microelectronics and Nanometer Structures **10**, 2743 (1992).

[14]M. Enyama, M. Sakakibara, S. Tanimoto and H. Ohta. Journal of Vacuum Science & Technology B, Nanotechnology and Microelectronics: Materials, Processing, Measurement, and Phenomena **32**, 051801 (2014).

[15]A. L. Eberle, S. Mikula, R. Schalek, J. Lichtman, M. L. K. Tate and D. Zeidler. J Microsc-Oxford **259**, 114 (2015).

[16]Casino v. v2.48 (2011).

[17]L. Reimer, *Scanning electron microscopy : physics of image formation and microanalysis* (Springer, 1998).

[18]H. Seiler. Journal of Applied Physics **54**, R1 (1983).

[19]W. Telieps. Applied Physics A **44**, 55 (1987).

[20]G. F. Rempfer and O. H. Griffith. Ultramicroscopy **27**, 273 (1989).

[21]G. F. Rempfer and O. Hayes Griffith. Ultramicroscopy **47**, 35 (1992).

[22]A. Mohammadi-Gheidari and P. Kruit. Nucl Instrum Meth A **645**, 60 (2011).

[23]I. Konvalina and I. Müllerová. Microsc Microanal **9**, 108 (2003).

[24]E. Bauer. Ultramicroscopy **17**, 51 (1985).

[25]H. Liebl and B. Senftinger. Ultramicroscopy **36**, 91 (1991).

Appendix A: Theoretical analysis of two subsystems

In this analysis, the UHR lens is activated as the magnetic objective lens. For simplification, the magnetic field of UHR lens and the electrostatic field above the sample are assumed to be block fields.

The first subsystem is to focus the axial primary beam. As the object distance is much larger than the focal length of the objective lens, the axial primary beam is assumed entering the field parallel to the optical axis with velocity v_2. On the sample, the velocity of the primary beam is v_1.

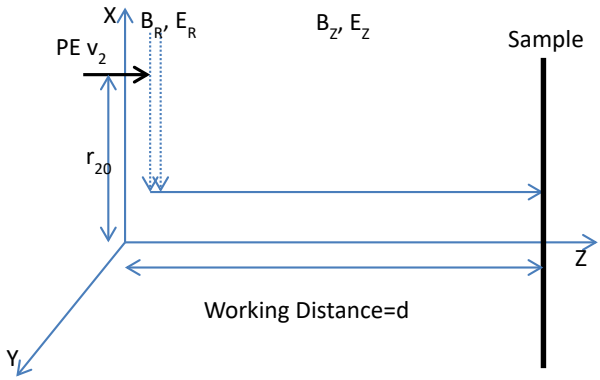

Figure 1 Schematic showing the field distribution above the sample. r_{20} is the primary electron's distance to the optical axis. B_R and E_R are the magnetic field and electrostatic field in R direction; B_Z and E_Z are the magnetic field and electrostatic field in Z direction. d is the working distance.

In the B_r and E_r region, the electrons get extra momentum;

$$P_{2B} = \int ev_2 B_r \cdot dt = e\int B_r \cdot dz = e\int \frac{r_{20}B_z'}{2} \cdot dz = \frac{er_{20}B_z}{2} \quad \text{(A1)}$$

$$P_{2E} = \int eE_r \cdot dt = e\int \frac{E_r}{v_2} \cdot dz = e\int \frac{r_{20}E_z'}{2v_2} \cdot dz = \frac{er_{20}E_z}{2v_2} \quad \text{(A2)}$$

where e and m are the charge and mass of electron; d is the working distance.

The composition is

$$P_{2c}^2 = P_{2B}^2 + P_{2E}^2 = (mv_{2c})^2 \quad \text{(A3)}$$

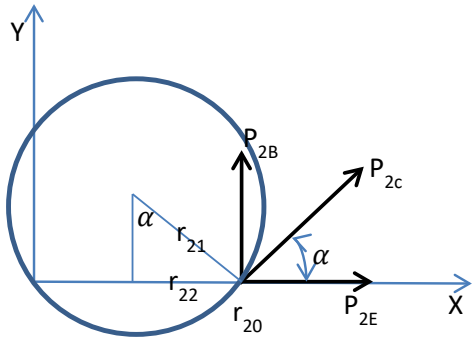

Figure 2 The focusing of the axial primary beam in the field. P_{2B} and P_{2E} are the momentum gained in the B_R and E_R region. P_{2c} is their composition. r_{21} is the radius of the primary electron's rotation; α is the angle between the P_{2c} and P_{2E}.

Because of this composition momentum, the primary electron starts to rotate in the B_z and E_z region. When the primary electron crosses the Z-axis, the primary beam is focused.

Inside the B_z field

$$r_{21} = \frac{mv_{2c}}{eB_z} \qquad \text{(A4)}$$

$$\sin\alpha = \frac{r_{22}}{r_{21}}, \tan\alpha = \frac{P_{2B}}{P_{2E}} = \frac{v_2 B_z}{E_z} \qquad \text{(A5)}$$

These two equations give $r_{22} = 0.5 r_{20}$, which proves that the primary beam gets focused.

The time of primary beam from entering the B_z field to being focused is

$$t_2 = \frac{(2\pi - 2\alpha) r_{21}}{v_{2c}} = \frac{m}{eB_z}(2\pi - 2\alpha) \qquad \text{(A6)}$$

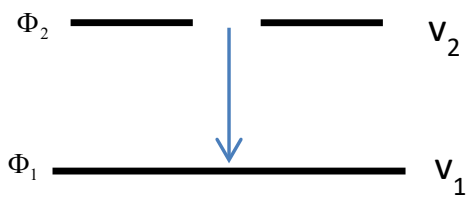

Figure 3 Schematic of the electrostatic lens.

In this time, the primary electrons are decelerated from v_2 to v_1

$$t_2 = \frac{v_2 - v_1}{a_2} = \frac{m(v_2 - v_1)}{eE_z} \qquad \text{(A7)}$$

$$E_z = \frac{(\Phi_2 - \Phi_1)}{d} = \frac{m}{2ed}(v_2^2 - v_1^2) \qquad \text{(A8)}$$

From equation (A7) and (A8), we get

$$\frac{m}{eB_z}(2\pi - 2\alpha) = \frac{m(v_2 - v_1)}{eE_z} \qquad \text{(A9)}$$

Combining equation (A5), equation (A9) can be written as

$$\pi - \frac{B_Z(v_2 - v_1)}{2E_Z} = \arctan(\frac{v_2 B_Z}{E_Z}) \qquad \text{(A10)}$$

The second subsystem is to focus the axial SE beam from the sample to the detection plane (the VA plane). It is assumed that SE in the sample with velocity $v_4 = v_{4x}$ and $v_{4y} = v_{4z} = 0$, considering the trivial initial SE energy compared to the SE velocity v_3 after the electrostatic field.

In the B_z and E_z region, E_z accelerates SE from 0 to v_3 and B_z makes the SE rotate.

$$t_4 = \frac{v_3}{a_4} = \frac{mv_3}{eE_z} \qquad \text{(A11)}$$

$$r_{40} = \frac{mv_{4x}}{eB_z} \qquad \text{(A12)}$$

in which t_4 is the time that the SE travels in the B_z and E_z region; r_{40} is the radius of the SE rotation.

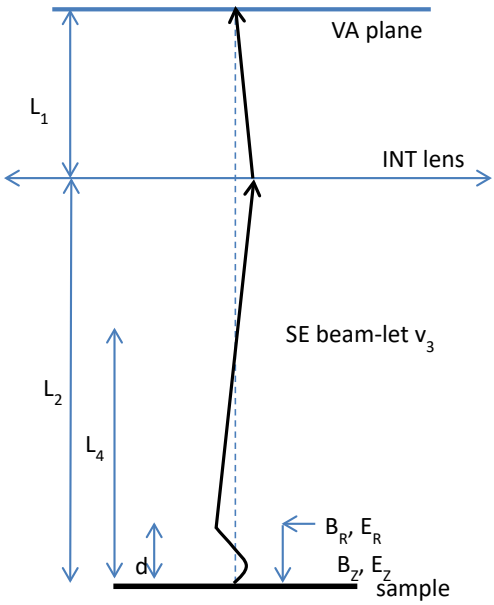

Figure 4 The focusing of the axial SE beam from the sample to the VA plane. L_1 is the distance from the VA plane to the INT lens, L_2 is the distance from the INT lens to the sample and L_4 the distance from the second crossover plane to the sample.

In the B_R and E_R region, the SE gets extra momentum

$$r_{41} = 2 \cdot r_{40} \cdot \cos\beta \qquad \text{A(13)}$$

$$P_{4B} = \frac{er_{41}}{2} B_z = mv_{4B} \qquad \text{A(14)}$$

$$P_{4E} = \frac{er_{41}}{2v_3} E_z = mv_{4E} \qquad \text{A(15)}$$

in which r_{41} is the radial distance when SE enters the B_R and E_R region; β is the angle between r_{41} and the Y-axis, and P_{4E} are the extra momentum SE gained from the B_r and the E_r ; v_{4B} and v_{4E} are the corresponding velocities;

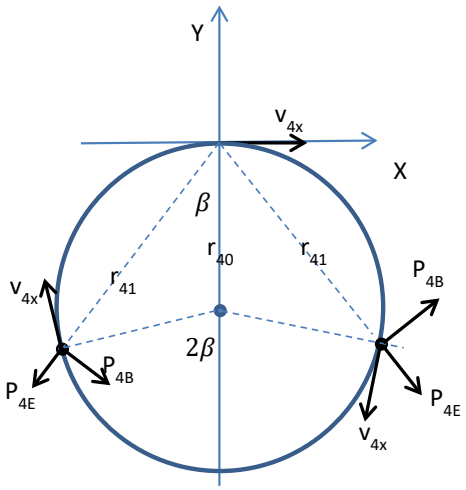

Figure 5 Illustration of two possibilities of the SE entering the B_R and E_R region; the left half shows it is possible to have a composition force pointing to the Z axis and the right side shows impossible.

As SE needs a crossover below INT lens, SE's velocity after the B_R and E_R region should point to the z-axis. As there is a strong field in this region, it is reasonable to assume the SE beam has one crossover. So, the SE needs to rotate 1.5~2 circles inside B_R region, and the extra momentum needs to meet

$$v_{4c} = v_{4x}\sin\beta - v_{4E} \qquad \text{(A16)}$$

$$v_{4x}\cos\beta = v_{4B} \qquad \text{(A17)}$$

$$t_4 = \frac{(3\pi + 2\beta)\cdot m}{eB_z} \qquad \text{(A18)}$$

Combining equation (A11) and (A18), we get

$$\beta = \frac{B_z v_3}{2E_z} - \frac{3\pi}{2} \qquad \text{(A19)}$$

After the block field region, when SE crosses the Z-axis

$$L_4 - d = \frac{r_{41}}{v_{4c}} v_3 \quad \text{(A20)}$$

Combining equation (A16) and (A20),

$$\tan\beta = \frac{E_z}{v_3 B_z} + \frac{2m}{eB_z(L_4 - d)} \qquad \text{(A21)}$$

The INT lens focuses this axial SE beam to the VA plane.

$$\frac{1}{f_S}=\frac{1}{L_1}+\frac{1}{L_2-L_4} \qquad \text{(A22)}$$

in which f_s is the INT lens' focal lengths for SE beam;

Actually L_4 can't be freely chosen. The INT lens also needs to focus all the primary beams from the VA plane to the coma-free plane of the objective lens which is very close to the B_r and E_r region.

$$\frac{1}{f_P}=\frac{1}{L_1}+\frac{1}{L_2} \quad \text{(A23)}$$

in which f_p is the INT lens' focal length for the primary beam.

Both for the primary beam focusing and for the SE beam focusing, the INT lens is treated as a thin lens. Its focal length follows

$$f=\frac{8m\Phi}{eB^2S} \qquad \text{(A24)}$$

in which Φ is the electron beam potential; B and S are the magnetic field strength and the gap size of the magnetic lens.

Then the relationship between f_s and f_p is

$$f_S=\frac{v_3^2}{v_2^2}f_P \qquad \text{(A25)}$$

Also, L_4 can be re-written as

$$L_4=L_2-\frac{L_1f_s}{L_1-f_s} \qquad \text{(A26)}$$

Combining equations (A19)(A21)(A26), the equation for the second subsystem is:

$$\arctan\left(\frac{eE_Z[(L_2-d)(L_1-f_s)-L_1f_s]+2mv_3^2(L_1-f_s)}{ev_3B_Z[(L_2-d)(L_1-f_s)-L_1f_s]}\right)=\frac{B_Zv_3}{2E_Z}-\frac{3\pi}{2} \quad \text{(A27)}$$

Chapter 5 Secondary electron imaging system in the Delft MBSEM1

This chapter introduces the design and implementation of the experimental setup for the secondary electron (SE) imaging system in the Delft MBSEM1 and presents the first experimental result. In the setup, a fluorescent material placed 45° with respect to the optical axis of the column converts the 196 secondary electron beams to 196 photon beams. An optical fiber imaging conduit transmits the photon beams out of the vacuum. An optical system images these 196 photon beams to a camera. An off-line processing program retrieves the intensities of the SE beams and constructs SE images. The focused and separated SE beams are seen in the experiment, and a SE image map is presented. The experimental results prove the working principle of the SE detection. The problems encountered in the experiments are discussed.

5.1 Working principle

The SE imaging system in a MBSEM needs to separately collect the SE beams when the primary beams are focused on a sample, and then uses their intensities to construct SE images. For the separate collection, the SE beams are focused onto a detection plane with a proper pitch.

The strategy used in the Delft MBSEM1 is to introduce a proper energy difference between the SE beams and the primary beams and then to utilize the electromagnetic lenses in the MBSEM column to focus the primary beams on the sample and to focus the SE beams in a detection plane simultaneously. The energy difference is achieved by biasing the sample stage negatively. This strategy needs little mechanical modification to our SEM column and keeps the systeem compact. A detailed description can be found in Chapter 4.

The variable aperture (VA) plane is chosen as the detection plane. There are two reasons. Firstly, the primary beams have a common crossover in the VA plane, shown in FIG 5. 1. The SE detection brings little disturbance to the primary beams. Secondly, there is space to insert a detector into the column. A port sits a few millimeters below the VA,

originally designed for a blanker in the Nova Nano SEM column. It can be used to insert the SE detector.

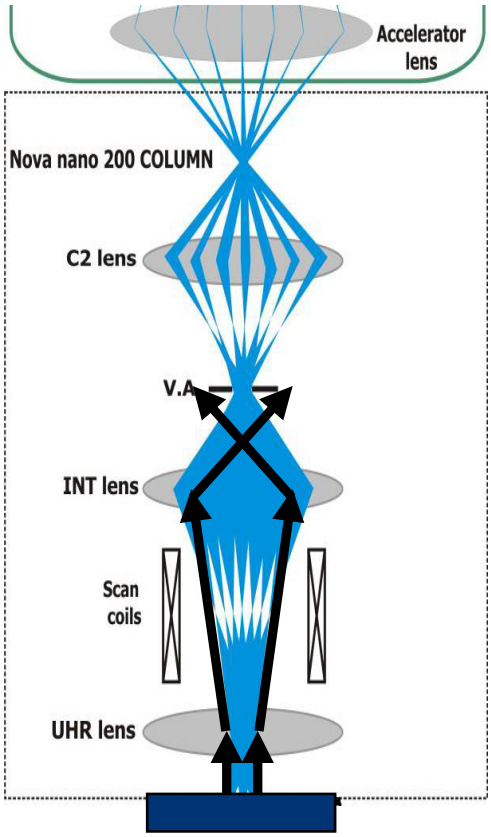

FIG 5. 1 Schematic of the SE detection principle: the primary beams are focused on the sample. Meanwhile, the SE beams are focused on the variable aperture (VA) plane using the same lenses in the SEM column.

5.2 Experimental setup

If we follow this strategy rigidly, a flat detector with a central hole needs to be placed a little below and parallel with the VA plane, shown in FIG 5. 2. A CCD/ CMOS chip is an option for the detector. The chip used for such placement should have a hole in the center, have excellent sensitivity andstand the bombardment from the secondary electrons with energies of a few keV for years. Such chip is hard to obtain. Additionally, the wiring, the electronics control, and the mechanical support need to go through a 10 mm-diameter hole. These two factors make it very challenging to start our experiment using the CCD/CMOS chip. Another

option is to use a fluorescent material to convert electrons to photons and employ a light guide to transfer the photons from the vacuum to the outside. This option is often used in electron microscopy[1,2]. However, it is very difficult to transmit 196 photon beams out with good separation when the fluorescent material is placed parallel with the VA plane. A complicated optical system needs to be designed and implemented in such a limited space. As we have no intention to modify the SEM column greatly, we do not place the detector parallel with the VA although there are options.

Our plan is to put the fluorescent material 45° with respect to the electron optical axis of the SEM column. This plan only needs to insert a few parts into that limited space. Outside the vacuum, an optical system image the photon beams onto a camera. Three potential issues are aroused from this 45° placement. Firstly, the SE beams potentially have different spot sizes on the detector because they hit the fluorescent material in different planes. Secondly, the distances among the adjacent SE beams may be different. Thirdly, the transmission efficiency of the photons from the vacuum to the air may be low.

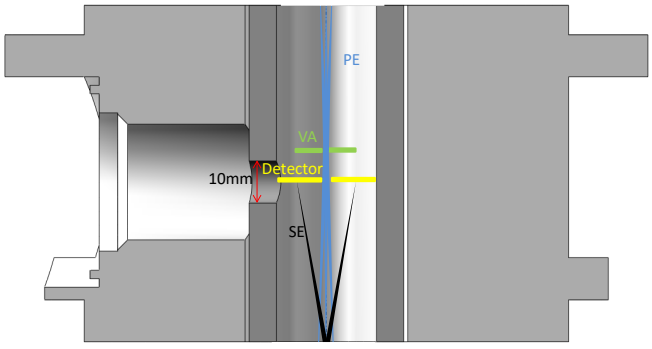

FIG 5. 2 Illustration of the SE beams' detection by placing a flat detector below and parallel with the VA.

Such issues will not bother us in the current development phase. For the first issue, the SE beams have a large depth of focus in the detection plane so that the spot sizes of SE beams change little on the fluorescent material. The example simulated in Chapter 4 has angular magnification

1.5×10^{-4} times. Even if the opening angle of one SE beam is 90° on the sample, it becomes 0.014° on its image plane. When the detection plane is 10 mm away from this image plane, the beam only broadens 2.4 μm, which is negligible compared to the spot size of the SE beams (tens of μm). For the second issue, this is just a technical challenge. A powerful image processing program can calculate the intensities of the SE beams even the SE beam grid is deformed, as long as the SE beams are separate in the detection plane. The third issue causes low throughput. However, in the present phase, we want to prove the working principle of the SE imaging, not to achieve high throughput imaging. The low signal detection efficiency is acceptable at this moment.

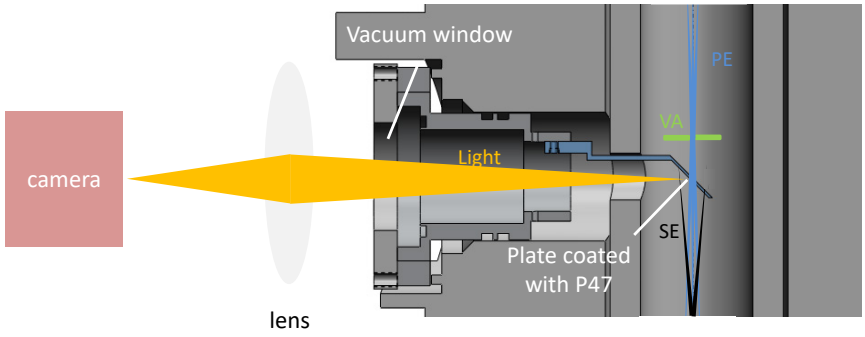

FIG 5. 3 Illustration of the SE beams' detection by inserting a 45o aluminum plate coated with P47 powder below the VA. An optical system is sitting outside the SEM chamber and images the SE detector onto a camera.

Two solutions are tried to guide the 196 light beams out with good separation. The first is to use a vacuum window and glass lenses outside the vacuum to image the 45° fluorescent material plate onto a camera, shown in FIG 5. 3. The long object distance of the optical system, due to the fluorescent material far away from the first glass lens, comforts a little on the issue of the 45° placed object. Two different shapes of the detectors are used, one with a central hole and the other not, shown in FIG 5. 4. They are made of aluminum and coated with fluorescent powder P47. These two images, captured by the CCD camera Prosilica GE680 camera from "Allied Vision Tech," proves that the SE beams in the detection plane can be separate. So the next step is to use such camera

images to construct SE images, similar to what we do in the transmission electron (TE) imaging.

However, this configuration has very low detection efficiency. The long object distance allows only 1% of the photons generated in the P47 entering the optical lens. Besides, the peak wavelength of P47 emission is 400 nm, but the GE680 camera has a maximum quantum efficiency at a wavelength of 500 nm. The camera needs to be set binning 8 (8× 8 camera pixels are combined to be one pixel) and an exposure time of 100 ms to get proper intensities of the SE beams, while in the TE imaging experiments, the setting of the camera is binning 1 and 0.3 ms exposure time. Such comparison indicates the low efficiency of the SE signal detection chain. Additionally, some part of the P47 coating layer on the aluminum plate drops after a few months experiments. All these make us stop using this configuration.

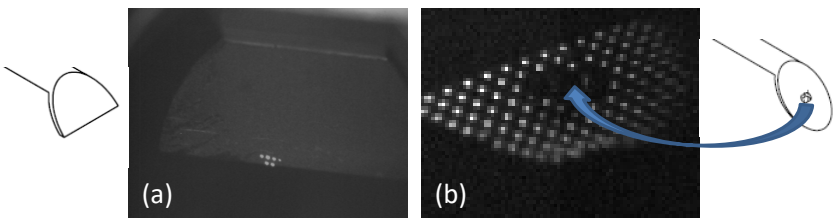

FIG 5. 4 (a) shows 6 separate SE beams landing on an aluminum plate coated with P47. (b) shows almost all 13 x 10 arrays of separate SE beams landing on another aluminum plate with a central hole; some SE beams are missing because of the large central hole.

The second solution is to use an optical fiber imaging conduit to transmit the photons generated in the fluorescent material. The fiber imaging conduit projects all features at one end, even if that is a 45° cut, to the other end with proper transmission efficiency. The difficulty is to drill a small hole in the fiber imaging conduit. It is doable but has technical challenges. We circumvent this challenges temperately by placing the fluorescent material on one side of SEM optical axis, as shown in FIG 5. 5. An optical focusing system images the other end of the fiber conduit onto a camera.

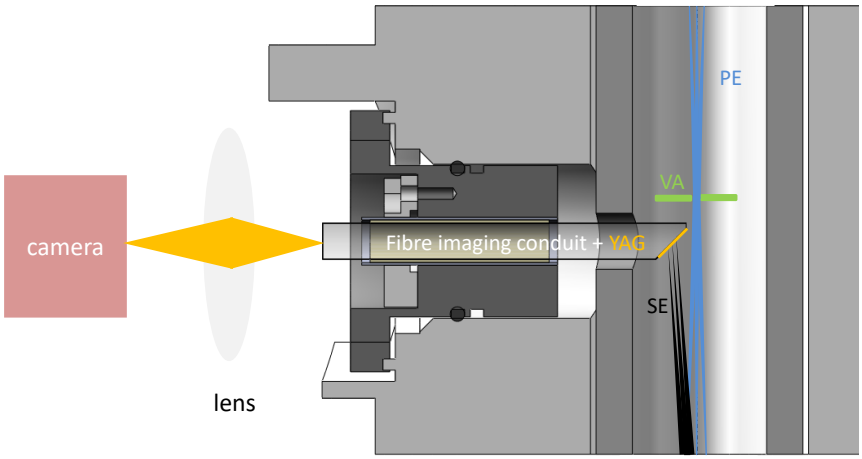

FIG 5. 5 Illustration of SE beams detection by inserting the assembly of the YAG and the fiber imaging conduit below the VA. An optical system sits outside the SEM chamber and images the SE beams' grid onto a camera.

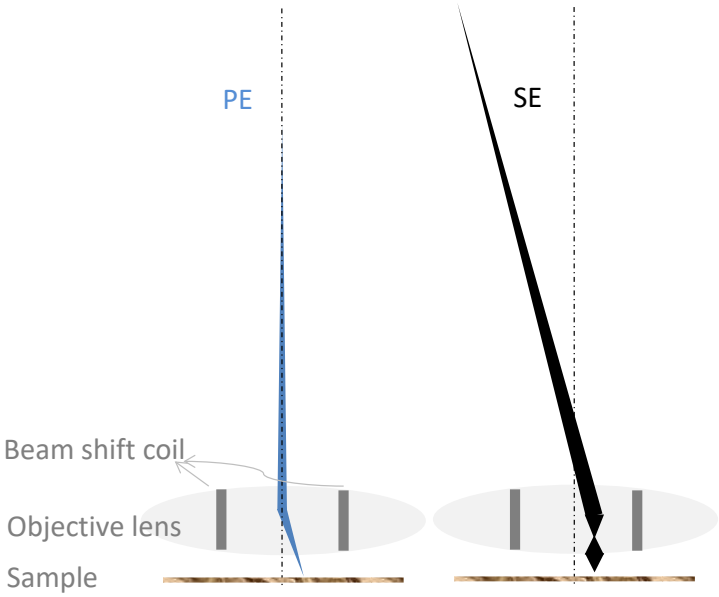

FIG 5. 6 Illustration of extra displacement contributed by beam shift to make all SE beams land on the YAG.

Although the fluorescent material is placed on one side of the optical axis, all the SE beams are possible to land on it by using the beam shift coils in the SEM column. The coils are close to the sample and far away

from the detection plane, illustrated in FIG 5. 6. A weak magnetic force that shifts the primary beams a little on the sample will shift the SE beams much on the detection plane. We are aware that the shift of the primary beams will lead to additional off-axis aberrations and deteriorate the resolution of the primary beams on the sample. The actual influence of using the beam shift coils needs to be investigated in the SE images. It is always an option to compensate the primary beams' deflection by an electrostatic deflector, but we do not add the electrostatic deflector in the experiment because of the limitation of the mechanical structure.

In the experiment, yttrium aluminum garnet [(YAG), $Y_3Al_5O_{12}$] is chosen as the fluorescent material to convert electrons to photons. It has high conversion efficiency (about 21 photons/ keV/ electron for low beam energy) and short decay time (70 ns, which is short enough for the current experiments). A YAG plate with a thickness of 30 μm is glued on the 45° cut end of an optical fiber imaging conduit. The assembly of the YAG and the imaging conduit is coated with 50 nm aluminum, to ensure conductivity and to reflect the photons back to the YAG. The company "Crytur" supplies the YAG plates and the source of the YAG data.

The first assembly of the YAG and the fiber imaging conduit is self-made. A YAG disk is cut to fit the size of the fiber imaging conduit and then is glued on the 45° cut end of the imaging conduit. The glue is EMI Optocast 3505-HM. Three small droplets of the glue are used, aiming to make the gap between the YAG and the imaging conduit as thin as possible. The gap can be barely seen, shown in FIG 5. 7. As the 30 μm thick YAG disk is very fragile, the YAG disk is broken in the process. This assembly is used for a few months. As the gap crack gives difficulty to retrieve the intensities of the SE beams, the second assembly is ordered from "Crytur."

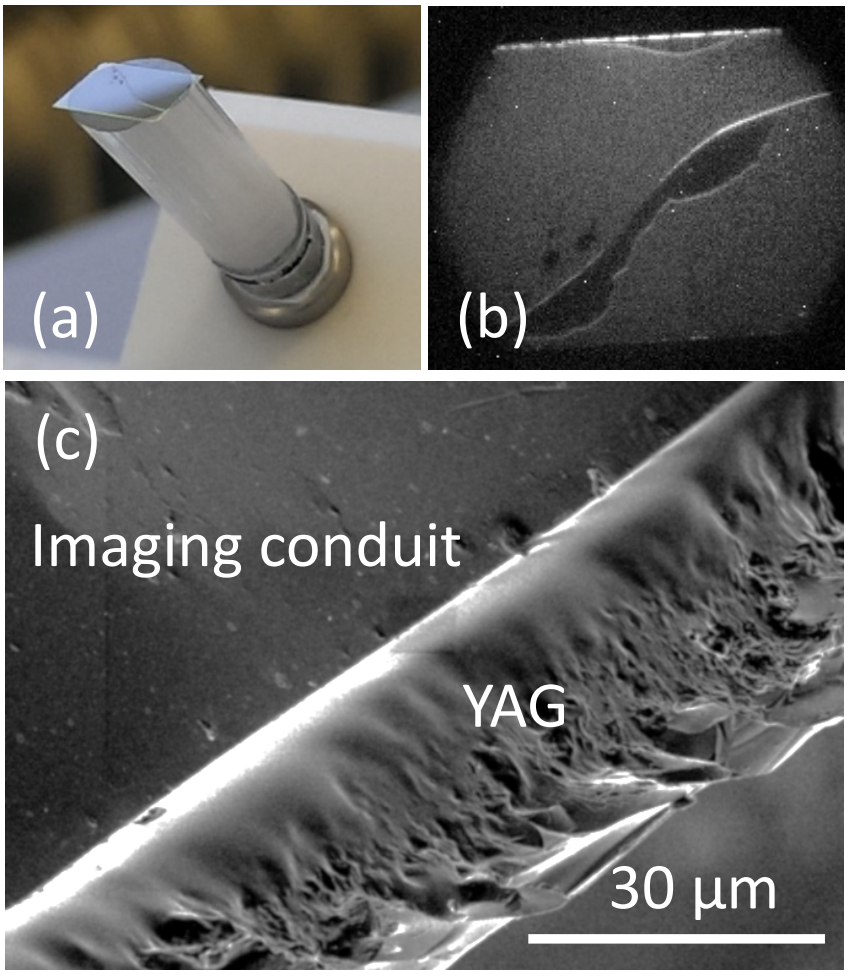

FIG 5. 7 (a) is the self-made assembly of the YAG and the fiber imaging conduit. (b) is the optical image of the YAG. (c) is the SEM image of the assembly, showing the gap between the YAG and the fiber imaging conduit is neglectable.

The choice of the YAG disk's thickness is explained as follows. Firstly, the emission of photons generated in the YAG disk is assumed to be a point source with a 2π distribution, evenly emitting photons to one side of the YAG disk because the YAG disk is coated with aluminum to reflect photons. Besides, the source of the photons is approximately at the surface of the YAG disk, because the penetration depth of electrons with an energy of 5 keV(the SE energy used in the experiment) in the YAG disk is only about 94 nm [3]while the thickness of the YAG disk is tens of micrometer. Then, a 2D model is built to estimate the effect of the YAG disk's thickness. Here the core of the fiber is used to represent the

imaging conduit for simplification. As the refraction index of YAG (1.82) is larger than the index of the core of the fiber (1.58), the photons within the opening angle of 60° can enter the fiber. Inside the fiber, only the photons whose angles are within the full reflection angle of 21°, can be transmitted to the other end of the fiber.[4] The effective size of the photon beam at the entrance plane of the fiber can be calculated, as illustrated in FIG 5. 8 (c) and (d). (c) shows the light path in the plane which is parallel to the axis of the fiber and the short axis of the ellipse due to 45° cut. (d) shows the light path in the plane which is perpendicular to the plane in (c). When the photon beam is about to enter the fiber, the ratio between the thickness of the YAG disk and the effective size of the photon beam is 1.5 in (c) and 1.1 in (d). These two planes are special planes, and the ratio in other planes should be between these two values.

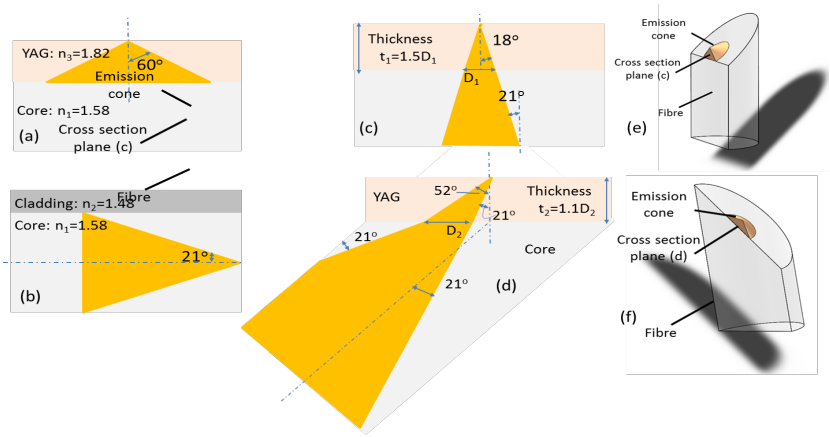

FIG 5. 8 Illustration of the light path in the assembly of the YAG and the fiber imaging conduit. (a) shows the full reflection angle when the photons generated in the YAG go from the YAG to the fiber core. (b) shows the full reflection angle in the fiber. (c) and (d) present the light path in the cross section planes shown in (e) and (f). (e) shows the plane which is parallel to the axis of the fiber and with the short axis of the ellipse due to 45° cut. (f) shows the plane which is perpendicular to the plane in (e). (c) and (d) tell the portion of photons which can be transferred out by the fiber, and the relationship between the effective size(D1 and D2) of photon beam and thickness of the YAG(t1 tan t2); the photons are in yellow.

When the YAG disk is thick, the photon beams expand, and the neighboring beams may overlap inside the YAG disk. When the YAG disk is thin, the size of the photon beam at the entrance of the fiber plane may be even smaller than the size of fiber, leading to uniformity issue, demonstrated in FIG 5. 9. The optical fiber imaging conduit has 50,419

fibers, each with a diameter of 24 µm, claimed by the provider "Edmund Optics." After inspection by an optical microscope, the pitch of the fibers is 24 µm, and the core diameter is about 19 µm. So, the effective size of the photon beam should not be smaller than 24 µm. Then, the thickness of the YAG needs to be between 36 µm and 26.4 µm considering the ratios in FIG 5. 8 (c) and (d). "Crytur" have 20, 30 and 100 µm thick YAG disks in stock. So we choose the thickness of the YAG disk to be 30 µm.

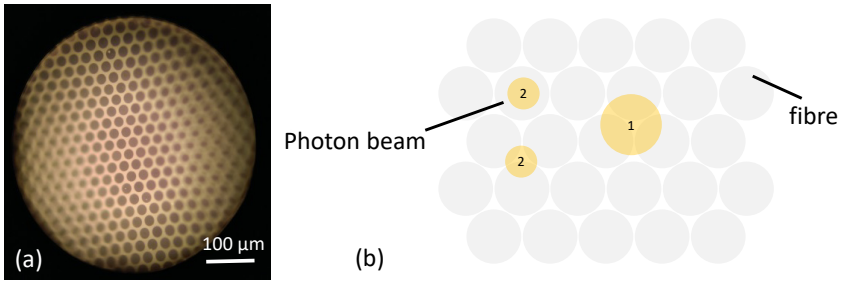

FIG 5. 9 (a) is the image of the fiber imaging conduit obtained via an optical microscope. (b) demonstrates that the size of the photon beam at the entrance of the fiber should be large to reduce the non-uniformity in the detected signal. Beam 2 brings more non-uniformity than beam 1.

FIG 5. 10 The Optical fiber imaging conduit in an aluminum tube to seal vacuum; its 45o cut end is coated with a 50 nm aluminum layer.

As the diameter of the imaging conduit is 6.35 mm with a tolerance of 0.25mm, its surface is too rough to seal vacuum by using O-ring directly. Our solution is to let the imaging conduit go through an aluminum tube whose surface is well polished, shown in FIG 5. 10. The gap between the imaging conduit and the aluminum tube is filled with vacuum gel " STYCAST 1266 A/B" which is a clear, low viscosity, and room temperature curable epoxy encapsulant. Carbon tape and carbon paint are used to keep the connectivity between the fiber imaging conduit and the aluminum tube.

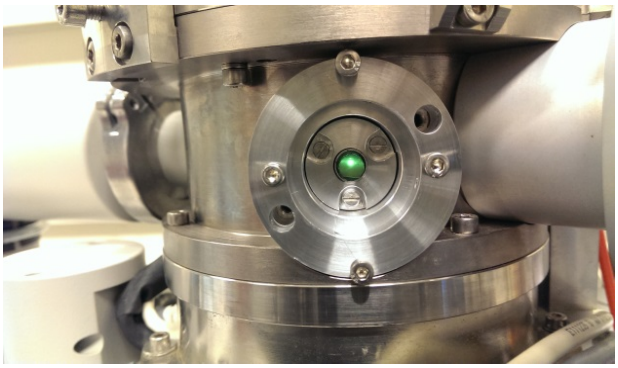

FIG 5. 11 The SE beams grid on the YAG as seen at the exit of the fiber imaging conduit.

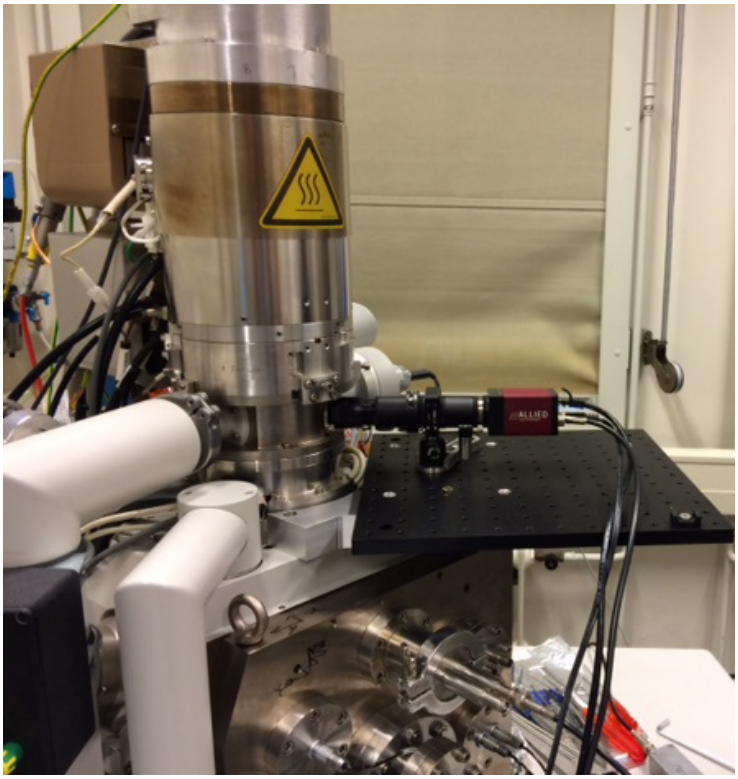

FIG 5. 12 The SE detection system in the Delft MBSEM1; an optical system with 0.5 times magnification is designed to focus the end of the optical fiber imaging conduit to a CCD camera.

FIG 5. 11 shows that the SE beams' grid is seen from the fiber imaging conduit even without any optical system and camera. The whole SE detection system is provided in FIG 5. 12. An optical system with a magnification of 0.5 times is designed to focus the end of the imaging

conduit in the air to a camera. Again, the separated and focused SE beams are recorded in a camera using this configuration.

The separate SE beams prove that the primary beams are separate but cannot tell whether the primary beams are focused on the sample. The focusing condition of the primary beams can only be tested in an imaging system. However, the SE detection efficiency of this YAG and fiber configuration is still too low to adjust the focusing of the primary beams, although it is already much improved. The camera GE680 needs to be set binning 2 (2 × 2 camera pixels are combined to be one pixel) and 20 ms exposure time to have a SE beam grid with proper intensities. So the scan dwell time should be set at least 20 ms, and it will take 8 seconds to get a SE image with 200 × 200 scan pixels. The scan dwell time is too slow to be used to search the best focusing. The TE imaging system is used to speed up the focusing process. The TE imaging system is described in Chapter 3. Here only a brief introduction is given. In the TE imaging system, a thin sample is placed on a YAG plate, which converts the 196 TE beams to 196 photon beams. A high-quality optical microscope, which is integrated inside the SEM chamber (called 'SECOM' platform),[4] focuses the photon beams onto a camera sitting outside the vacuum with a large magnification. In each scan step, the camera records a TE grid image with 196 spots, whose intensities can be retrieved. After one scan period, such signal intensities are gathered together to construct TE images. The TE imaging system is in its first development phase, and an offline image processing mode is utilized. In this mode, the camera images are saved in a computer firstly and then processed to construct TE images. The second development step of the imaging system is to achieve slow real time imaging by utilizing the FPGA technology, and not a part of this thesis. The TE imaging system needs a small modification. The distance between the sample and the high magnification objective lens (for example, 40×) is 0.2-0.3 mm. In the SE imaging experiment, the sample stays at high voltage (a few kV). The objective lens is insulated from ground and connected to the sample to prevent arching between the sample and the objective lens.

Two cameras are used in the experiment, Prosilica GE680 camera and "CoolSNAP EZ" monochrome camera from "Photometrics." One is used to monitor the SE beams grid and the other for the TE beams grid. Only

the camera GE680 is used to do TE/SE imaging because it is fast. These two SE imaging systems share the image acquisition and processing program. In this chapter, the SE image map is obtained via using the off-line image processing.

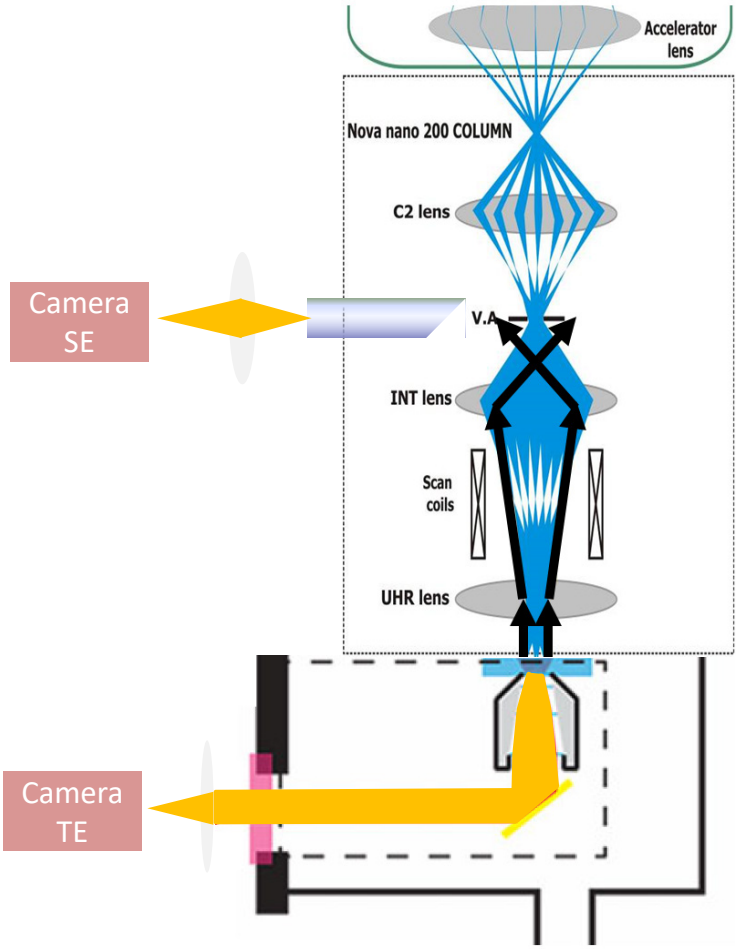

FIG 5. 13 Illustration of the SE imaging system and the TE imaging system in the Delft MBSEM1.

5.3 Experimental results

5.3.1 Sample information

As the electron optical setting in the Delft MBSEM1is entirely different from the original FEI setting, a calibration sample is used to calculate the

scan field of view. The sample is made by depositing tungsten on a YAG plate. The line patterns have a width of 0.5 µm and a pitch of 1.0 µm, and the hole patterns have a diameter of 0.4 µm and a pitch of 0.6 µm.

FIG 5. 14 Patterns in the calibration sample; the color part is electron transparent area, and the white is tungsten. Lines: 0.5µm wide, 1µm pitch; holes: 0.4 µm diameter, 0.6 µm pitch.

5.3.2 Focusing procedure:

In the SE imaging experiment, the energy of the primary beams before the deceleration is 15 keV. The acceleration (ACC) lens forms the primary beams a common crossover in the VA plane, and the C2 lens is off. The combination of the high-resolution (HR) lens and the ultra-high resolution (UHR) lens is used as the magnetic objective lens.

The operation of the SE imaging in the Delft MBSEM1 is different from, and more complicated than in a single beam SEM because the focusing of the primary beams and the focusing of the SE beams need to be achieved simultaneously. The operation procedure is described as follows.

a. Get coarse focusing condition

In this step, the primary beams' grid on the sample and the SE beams' grid on the SE detector should be seen in the TE imaging camera and the SE imaging camera, by adjusting the strengths of the lenses in the SEM column, including the INT lens, the combination of the HR and the UHR lens, and the deceleration field (or called retarding lens). When the primary beams' focusing and the SE beams' focusing are achieved simultaneously, the TE beams and the SE beams in the camera images should have the smallest spot sizes. However, when such camera images are acquired, we can only conclude that the primary beams are coarsely focused on the sample because the point spread function of electrons in the YAG disk and the resolution of the optical system is much larger than the primary beams' resolution.

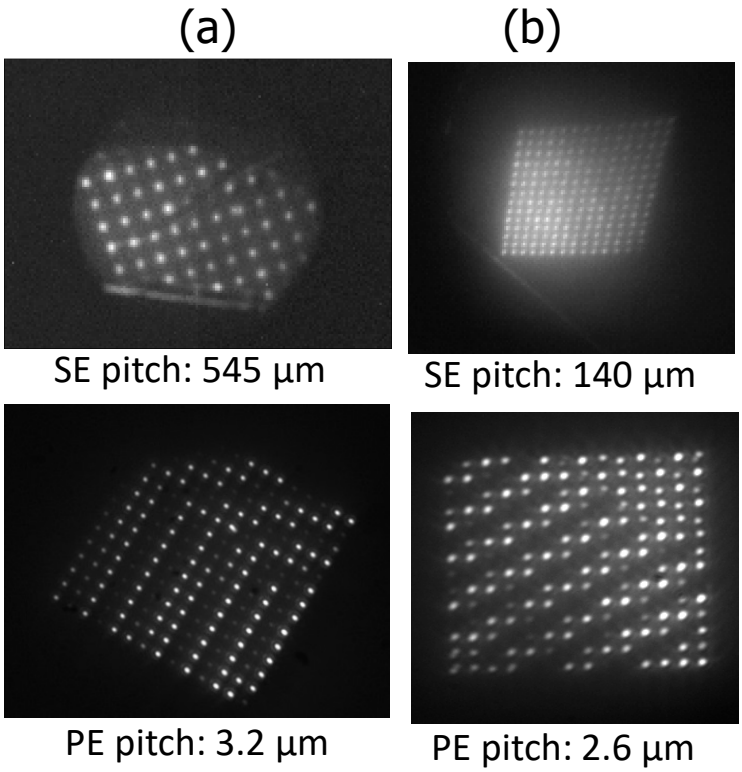

FIG 5. 15 Two examples of the primary beams focusing on the sample and the SE beams focusing on the detector. "PE pitch" means the pitch of the primary beams on the sample and "SE pitch" means the pitch of the SE beams on the detector.

FIG 5. 15 shows two examples. In one example, the pitch of the primary beams is 3.2 µm, and the pitch of the SE beams is 545 µm. In the other example, the values are 2.6 µm and 140 µm. The settings of the INT lens, the HR lens, the UHR lens, the retarding lens and the working distance is 0.76, 1.7537, 4.77(values shown in the FEI user interface), 7.0 kV and 2 mm in the first example. The settings are 0.765, 1.88 and 5.387, 9.8 kV and 2 mm in the second example.

b. Acquire fine focus lenses setting via checking TE images

In this step, the fine focus setting of the objective lens for the primary beams is obtained by checking the TE images. It is much faster to get TE images because the detected TE signal is much stronger than the detected SE signal in the current detection systems. The camera GE680 needs to

be set binning 2 and exposure time 20 ms for the SE detection while binning 1 and 0.5 ms for the TE detection. As the coarse focus is obtained in the first step, it hardly affects the SE beams' focusing during the search the fine focus condition. The SE beams should still be separated well on the detector after the fine focusing.

In the image processing, a Labview program is used to synchronize the camera and the beam scan driver in the SEM. It has a function to select one small region of the camera where one beam stays, and to form images for this beam. The images in FIG 5. 16 show the TE images using the different combinations of the lenses while SE beams are separated on the detector.

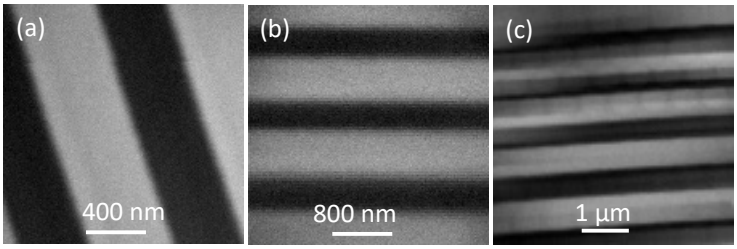

FIG 5. 16 TE images of one single beam with different field of views, 1.6, 3.2 and 5.0 µm, respectively from (a) to (c). The setting of the INT lens, the HR lens, the UHR lens, the retarding lens and the working distance is 0.76, 1.7537, 4.770, 7000 V and 2 mm for (a); 0.65, 1.786, 4.5644, 6600 V and 2 mm for (b); 0.65, 1.72, 2.913, 6600 V and 2 mm for (c).

c. Check SE images

This step is optional, just to verify the focusing condition by the SE imaging. The focusing condition obtained in the second step normally can be directly used to get SE images without any adjustment. FIG 5. 17 presents the SE images saved in different experiments. They are typical SE images, which have bright edges. The image (a) has an FOV 0.8 µm and (b) has an FOV of 1.6 µm. They are acquired by setting the INT lens, the HR lens and the UHR lens 0.76, 1.7537 and 4.77, the retarding lens 7.0 kV and the working distance 2 mm. Image (c) with FOV 2.7 µm is acquired by setting the lenses 0.765, 1.88 and 5.387, 9.8 kV, respectively, and the working distance 2 mm. It is one of the 196 SE images obtained simultaneously shown in FIG 5. 18.

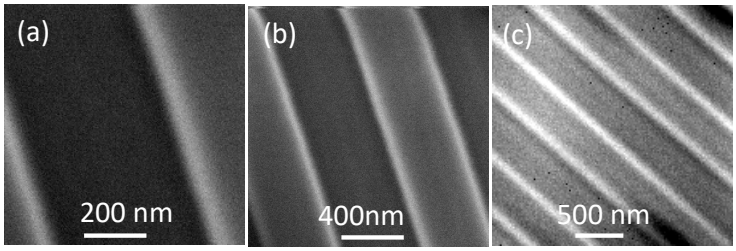

FIG 5. 17 SE images of one single beam with different field of views, 0.8,1.6 and 2.7 μm from the image (a) to (c). The setting of the INT lens, the HR lens, the UHR lens, the retarding lens and the working distance is 0.76, 1.7537, 4.770, 7000 V and 2 mm for (a) and (b); 0.765, 1.88, 5.387, 9800 V and 2 mm for (c).

d. Construct SE images

In this step, the offline image processing is used to construct SE images. The SE beam grid images are saved into a computer via the Labview program. The intensities of the beams are retrieved and used to construct SE images by an image processing program written in Matlab. FIG 5. 18 is a SE image map. It is acquired by setting the INT lens, the HR lens and the UHR lens 0.765, 1.88 and 5.387, the retarding lens 9.8 kV and the working distance 2 mm. This image map has 38 μm FOV and 2100 × 2100 pixels.

5.4 Discussion

5.4.1 Pixel size and intensity uniformity

The pixel size of the image map is 18 nm. Surely this cannot show the fine pattern that is smaller than 18nm. Such result is yet high-resolution imaging in the Delft MBSEM1.

The pixel size is the division of the scan FOV over the scan resolution. The pitch of the primary beams in the Delft MBSEM1 mainly decides the scan FOV. So the pixel size is limited by the scan resolution. In the SE imaging, the Labview program controls the synchronization between the GE 680 camera and the scan and saves the camera images on a computer. In one scan step, although the useful information is just196 intensities and positions, a whole camera image needs to be saved. This program can handle no more than 8 Gbyte data in one scan period. So the camera image size and the Labview program limit the scan resolution and the pixels size.

This issue will be solved in the next development phase of the image processing. In the new phase, FPGA technology is used. In the scan, the camera images are directly sent to a FPGA. The intensities and positions of the beams are calculated by the algorithm in the FPGA and sent to a computer to construct images. So the limitation of the pixel size is gone. More detail explanation can be found in Chapter 3.

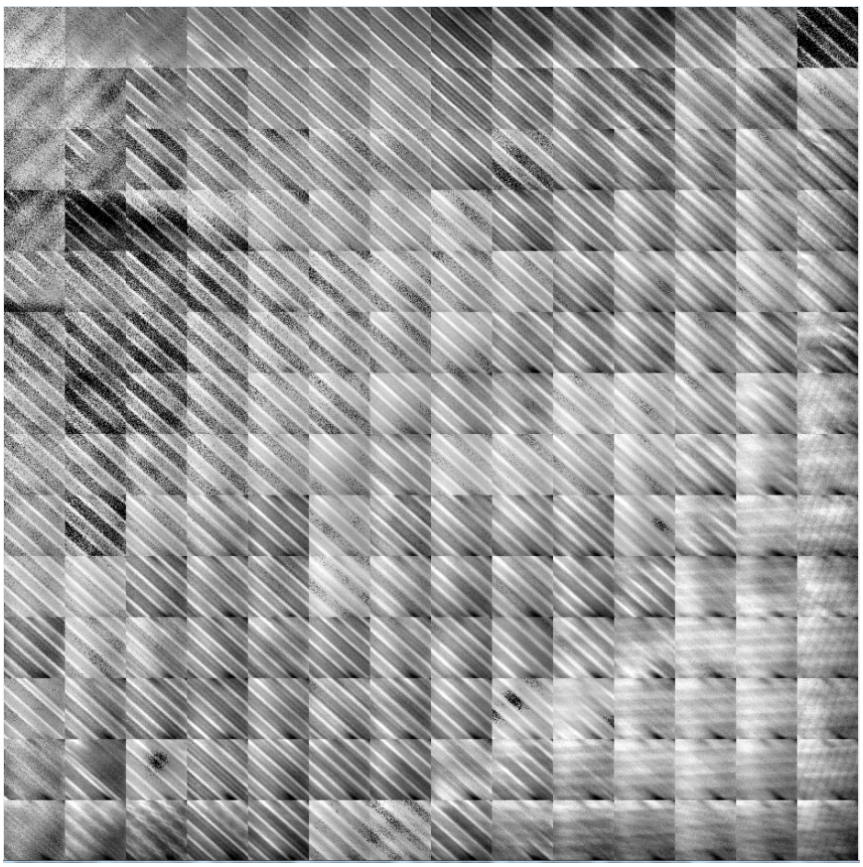

FIG 5. 18 A SE image map using calibration sample, with an FOV of 38μm and 2100 × 2100 pixels. It is acquired using the INT lens, the HR lens and the UHR Lens, 0.765, 1.88 and 5.387, respectively, the retarding lens 9800V and working distance 2 mm. The current of each beam-let is 30pA. The SE beams' grid image is shown in FIG 5. 15(b).

Intensity differences among the beams are clearly shown in FIG 5. 18. The potential causes of this non-uniformity are also discussed in Chapter 3. Additionally, intensity loss happens almost in every sub SE image. When one sub-image is zoomed in, there are many dark pixels in the image, such as the image (c) in FIG 5. 17. The main reason is that the

image processing program cannot accurately recognize each beam's position when the SE grid is much distorted and thus unable to calculate its intensity correctly. The intensity difference is not a fundamental problem and will be fixed in the future.

5.4.2 Imaging resolution

The imaging resolution is 24 nm using 25% to 75% intensity edge method. So the spot size defined by the FW50 is 42nm,[5] which is certainly not our goal. We expect to have better than 10nm resolution. There are a few potential reasons. Firstly, the whole alignment of all lenses in the MBSEM can be improved. In the experiment, the alignment between the objective lens (the combination of the magnetic objective lens and the retarding lens) and the other lenses cannot be fully done even when the control of alignment coils is set to its maximum. More effort should be put into the alignment. Secondly, the beam shift leads to additional off-axis aberrations and misalignment. The beam shift is activated to collect all SE beams in the detector. Unavoidably, the primary beams are pushed before entering the objective lens. The beam shift adds additional off-axis aberrations to the primary beams. This factor needs to be evaluated in the future. If this generates too large off-axis aberrations, we should give up using beam shift to get all SE beams in the detector, and turn to Wien Filter so that the primary beams go straight while the SE beams are deflected. Thirdly, the calibration sample is not suitable for the resolution test. The height of the sample is a few hundred nm. It is too high to be used as a good knife edge to test the resolution close to 10 nm. A resolution test sample, such as gold particles and Tin balls should be used in the future. Last but not least, the current orientation of the HR lens is different from the orientation of the UHR lens. The orientation difference is a big surprise to us. In the simulation result presented in Chapter 4, the current orientations of the HR lens and the UHR lens are assumed the same. When the excitation of the UHR lens became stronger in the combination, the excitation of the HR lens needed to turn weaker to get the primary beams focused on the sample. However, in the experiment, when the excitation of the UHR lens is stronger, the excitation of the HR lens also needed to be stronger, due to the overlap between the magnetic fields of the HR lens and the UHR lens, shown in FIG 5. 20. This orientation difference is unexpected and not

welcomed. In the simulation, the UHR lens with strong strength is usually good to achieve high-resolution images. So in the experiment, the excitation of the UHR lens is preferred to be strong. Then the excitation of the HR lens is also strong. The off-axis aberrations in such combinations will become worse than expected. The current direction of either the UHR lens or the HR lens needs to be changed in the future to improve the image resolution and uniformity.

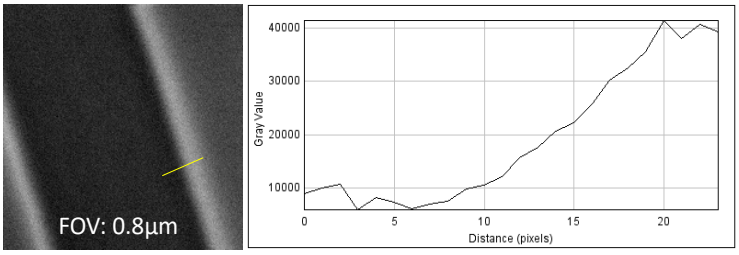

FIG 5. 19 25%-75% intensity method indicates 24 nm resolution; SEM image has 200 x 200 pixels for FOV 0.8 μm.

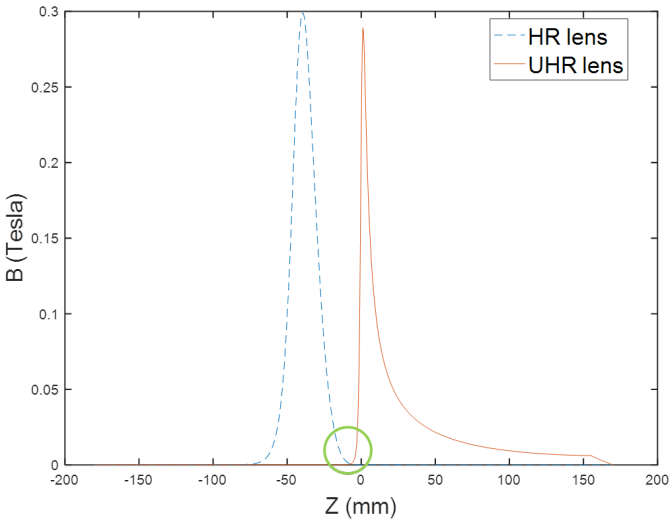

FIG 5. 20 The overlap between the magnetic fields of the HR lens and the UHR lens.

5.4.3 Detection efficiency and detection quantum efficiency

The detection efficiency of SE imaging in the Delft MBSEM1 is low. The scan dwell time is set to be 20 ms when the landing energy is about 5 keV and the current of one primary beam is about 30 pA. The scan dwell time is around 1 μs in a commercial single beam SEM to generate a similar

quality SE image. It is impossible to deliver high throughput imaging in the Delft MBSEM1 with such low detection efficiency.

The detection efficiency of the SE imaging system is estimated as follows with a few simplifications. When the SEs meet the YAG disk and its aluminum coating layer, the backscatter loss is about 20%, simulated by "Casino"[6]. The other 80% SEs are assumed without any energy loss and hit the YAG. In the experiment, the SE energy on the detection plane is about 5 keV. The photon yield of YAG is 21 photons/ keV/ electron, from "Crytur." So one SE generates 105 photons in the YAG. The photon emission of the YAG is simplified to generate the photons only with 550 nm wavelength, the wavelength of the maximum emission in the emission spectrum. In the 2D model to simplify the photon transmission from the YAG to the fiber, about 3.8% of the photons generated in the YAG, can enter the fiber and meet the full reflection criterion between the core and the cladding. The transmission efficiency of the fiber is 35% - 45%.[7] We take 40%. The first lens in the optical system has a diameter of 25.4 mm and a 90% clear aperture, placed 50.9 mm away from the flat end of the imaging conduit. So 11.4% of the photons that can exit the imaging conduit enter the optical system, considering that the photon beam has an opening angle 33.6° which is the full reflection angle due to the fiber optics. As the optical lenses used in the system have an antireflection coating (for the wavelength from 400 nm to 700 nm), giving 0.30% reflection per surface.[8] So the transmission efficiency of the optical system is 98.8%. The conversion efficiency of the camera GE680, or called quantum efficiency, is 0.45 for the photons with 550 nm wavelength, which means that 100 photons generate 45 electron-hole pairs. So in the detection system, 100 secondary electrons lead to 14.4 photons onto the camera and 6.5 electron-hole pairs in the camera.

The real efficiency might be even worse than the estimated value. In the 2D model, the core material is used to replace the combination of the core and the cladding. The difference between the real fiber structure and the simple model may cause 37% more loss on the transmission efficiency of the assembly.

This low detection efficiency will make the detection quantum efficiency (DQE) low, especially when the noise is independent of the intensity of

the signal in the output signal detection chain. DQE in a detection system can be calculated as [2]

$$DQE = \left(\frac{SNR_{out}}{SNR_{in}} \right)^2 \quad (5.1)$$

where SNR_{in} is signal noise ratio of the input signal and SNR_{out} is the signal noise ratio of the output signal.

We do a simple test of the DQE in the SE imaging system. The YAG plate is placed upwards so that the primary beams directly hit the YAG. The combination of the ACC lens and the C2 lens focused all beams on the YAG, illustrated in the image (a) in FIG 5. 21. The camera saves 400 frames of such images. Then the beams are switched off, and the camera uses the same setting to record another 400 images as the background. The beam energy is 15 keV. The total current is 147 nA. The exposure time of the camera is 32 μs. The primary electrons are used as the input signal. Assuming that they follow the Poisson distribution,[2] then

$$SNR_{in} = \sqrt{N_{pe}} \quad (5.2)$$

where N_{pe} is the number of primary electrons. The camera images are the output signal. The SNR_{out} can be calculated by

$$SNR_{out} = \frac{I_{mean}}{I_{std}} \quad (5.3)$$

where I_{mean} is the mean intensities of the signal and I_{std} is the standard deviation of the signal. A window in the camera images is used in the calculation, shown in the image (b) of FIG 5. 21. The selection of the window size influences the result. The maximum DQE in this test is about 1.76% using a window with 40 × 40 pixels. The similar test is also done for the TE imaging system. The DQE of the TE imaging system is about 40% using 15 keV landing energy.

When the contrast of the image (b) in FIG 5. 21 is adjusted, unusual patterns appear, shown in the image (c) in FIG 5. 21. Firstly the small bright dot in the image (b) become a much larger spot with unevenly distributed intensities. Also, there is a weak vertical line pattern. We do

not know why and how these patterns appear. They may be related to the 45° cut in the imaging conduit.

The low detection efficiency still allows us taking SE images slowly in the Delft MBSEM1. However, the SE imaging system needs to be improved much to have high throughput imaging, for example by optimizing the assembly of the YAG disk and the imaging conduit, redesigning the optical system and utilizing a camera with better sensitivity and less noise.

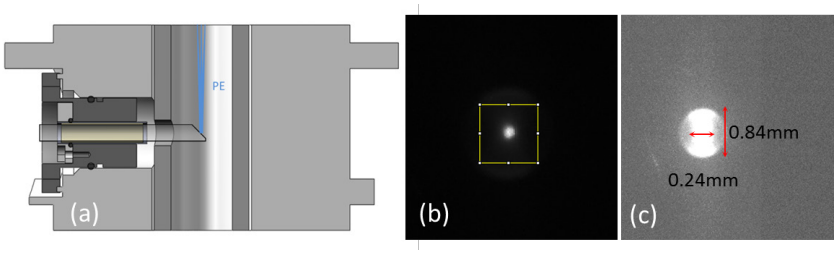

FIG 5. 21 (a) is the configuration for the DQE test. The YAG faces upwards, and the primary beams are focused on the YAG. (b) is the camera image used in the DQE test. The intensities in the yellow window are used in the calculation. (c) shows odd patterns in the camera image when the contrast of the images is adjusted.

5.4.4 Crosstalk

The example in Chapter 4 tells that the SE beam on the detection plane has a sharp peak and a long tail. Such distribution causes the crosstalk. In the experiment, the crosstalk indeed exists in the SE grids on the detector, demonstrated in FIG 5. 22. In the working case (a), the pitch of the primary beams on the sample, the pitch of the SE beams on the detector and the electrical field above the sample are 3.07 μm, 285 μm, and 5667 V/mm. In the case (b), these three values are 2.65 μm, 200 μm and 4490 V/mm. In the case (c), these three values are 2.59 μm, 140 μm and 5444 V/mm.

The amplitude of the peaks divided by the amplitude of the crosstalk is introduced to evaluate the degree of the crosstalk, shown in FIG 5. 23. The higher the result is, the less the crosstalk is. The quotient in the case (a) to (c) are 2.14, 1.55, and 0.20 by averaging a few data sets. The crosstalk in the case (c) is the worst. Such result seems against the

conclusion in Chapter 4. Chapter 4 shows that the SE virtual source size is the dominant factor in the simulated example, and is strongly influenced by the electrical field above the sample. A strong electrical field leads to a small SE virtual source size. The SE virtual source sizes in the sample in these three cases are 0.12 μm, 0.13 μm and 0.12 μm using the FW25 (Full Width containing 25% current) method, respectively. In the detection plane, the magnified SE virtual source sizes by the FW25 method are 11.1 μm, 9.8 μm, 6.5 μm, using the magnifications of the SE focusing 92.8, 75.5, 54.1 times in these three cases. The ratios of the magnified SE virtual source size over the pitch of the SE beams in the detection plane is 0.040, 0.049, 0.046, respectively. If the SE virtual source size was the dominant factor in the spot size of the SE beams in the detection plane, then the crosstalk effect should have been weak, and the case (c) had the less crosstalk than the case (b). However, the reality is that there is strong crosstalk, especially in the case (c). The contradiction means that the aberrations should contribute much to the SE beam size in the experiment.

Additionally, the SE beams' grid in the detection plane is more distorted than the TE beams' grid in the experiment. This fact also proves that the aberrations are strong in the experiments.

The analysis on the crosstalk here and in Chapter 4, shows that there are two ways to reduce the crosstalk effect. One way is to apply a strong electrical field above the sample to suppress the SE virtual source size. The other way is to reduce the aberrations generated in the SE beams' focusing.

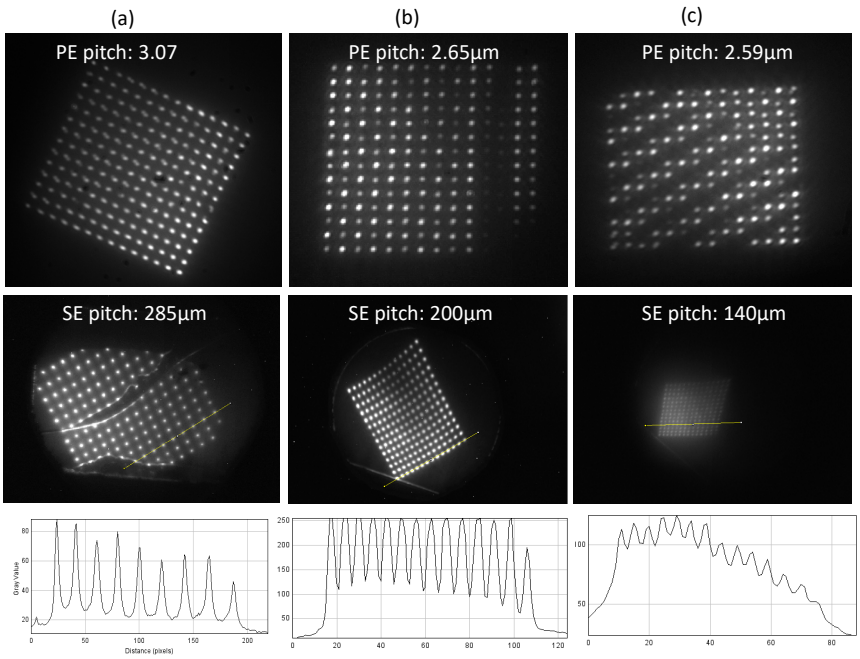

FIG 5. 22 Three different working cases with different primary beams' pitch on the sample and SE beams' pitch on the detector. The intensity profile of lines in the images is plotted to check crosstalk contribution. Case (a) is acquired by set the INT lens, the HR lens, the UHR lens, the retarding lens and the working distance 0.76, 1.7635, 4.975, 8500 V and 1.5mm. Case (b) is got with the setting 0.76, 1.910, 5.4382, 8980 V and 2 mm; case (c) with the setting 0.76, 1.88, 5.3874, 9800 V and 1.8 mm. The values of the INT lens, the HR lens, and the UHR lens are the strengths shown in the FEI user interface. "PE pitch" means the pitch of the primary beams on the sample and "SE pitch" means the pitch of the SE beams on the detector.

5.5 Conclusion and outlook

This chapter describes the experimental setup built for testing the working principle of the SE imaging system in the Delft MBSEM1 and presents the first experimental results.

In the experimental setup, a YAG disk is used to convert the SEs to photons, and an optical fiber imaging conduit guides the light out of vacuum meanwhile keeping the 196 photon-beams signals separated. The YAG disk with a thickness of 30 µm is glued on one end of the imaging conduit, the end with a 45° cut. An optical system outside the vacuum images the other end of the imaging conduit onto a camera. An off-line processing program acquires the intensities of the SE beams from the

camera images and constructs SE images. The TE imaging setup is used to help to get the primary beams' focusing quickly.

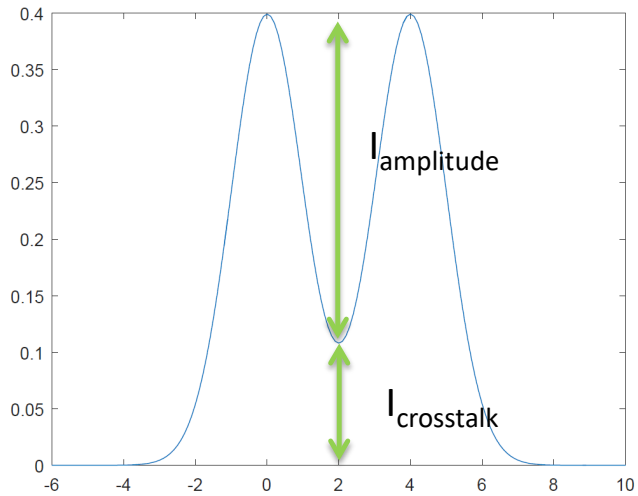

FIG 5. 23 The crosstalk can be evaluated via dividing the amplitude of the signal $I_{amplitude}$ over the crosstalk $I_{crosstalk}$.

In the experimental results, the primary beams are focused on the sample, and the SE beams are focused and separated on the YAG simultaneously. The typical SE images from our MBSEM are obtained using a calibration sample, and the first SE image map is presented. The experiment proves the SE detection working principle. Meanwhile, it also arouses a few issues that need to be improved or solved in next experimental design, listed in the following.

The SE imaging resolution needs to be improved. To achieve this, firstly, the fiber imaging conduit may be kept on the system axis. So a hole must be drilled, or a Wien filter needs to be added in the SEM column. Secondly, the alignment of the electron optical system can be improved. Thirdly, the current orientation of the HR lens and the UHR lens should be set the same.

Crosstalk exists in the SE grids on the detection plane. It can be reduced by applying a strong electrical field above the sample to reduce the SE virtual source size in the sample, and optimizing the SE focusing on

minimizing the aberrations generated. Its influence on the SE images also needs to be evaluated.

The detection efficiency of the SE imaging system in the Delft MBSEM1 needs to be improved. Now the scan dwell time is 20 ms, which is too slow to do high throughput imaging. The goal is to use 100 ns dwell time, which is often used for the fast scan in a single beam SEM. The detection chain, including the fluorescent material, the imaging conduit, the optical system and the camera, needs to be optimized.

After such improvements are made and the real-time image processing system using FPGA technology is developed, the Delft MBSEM1 should deliver high-throughput and high-resolution SE imaging.

5.6 Acknowledgement

I would like to thank Carel Heerkens for the help of cutting the YAG, assembling the YAG and the fiber imaging conduit and coating the assembly, Jan De looff for manufacturing the insulation part, Paul Keijzer for making the Labview program.

5.7 References

[1]L. Reimer, *Transmission electron microscopy : physics of image formation and microanalysis* (Springer, 1997).

[2]L. Reimer, *Scanning electron microscopy : physics of image formation and microanalysis* (Springer, 1998).

[3]Crytur. <https://web.archive.org/web/20151218133536/http:/crytur.com/> (2014).

[4]A. C. Zonnevylle, R. F. C. Van Tol, N. Liv, A. C. Narvaez, A. P. J. Effting, P. Kruit and J. P. Hoogenboom. J Microsc-Oxford **252**, 58 (2013).

[5]M. S. Bronsgeest, J. E. Barth, L. W. Swanson and P. Kruit. J Vac Sci Technol B **26**, 949 (2008).

[6]Casino v. v2.48 (2011).

[7]E. optics. <http://www.edmundoptics.com/optics/fiber-optics/fiber-optic-image-conduits/38303/> (2014).

[8]Thorlabs.<http://www.thorlabs.de/images/TabImages/Achromatic_Doublet_AR_Coatings.xlsx> (2014).

Chapter 6 Conclusion and outlook

Multiple-beam scanning electron microscopy is developed to increase the throughput of electron microscopy dramatically. A multiple-beam scanning electron microscope (MBSEM) with imaging systems will benefit many fields, especially biological research and semiconductor manufacturing.

A MBSEM with 196 beams has been built in TU Delft based on the revision of an FEI Nova Nano 200 SEM, called the Delft MBSEM1. It is a single source and single column system. Before my Ph.D. project started, the current uniformity and the resolution of the electron beams in the Delft MBSEM1 had been tested and an electron beam induced deposition (EBID) experiment had been done using this MBSEM. However, there was no imaging function in the Delft MBSEM1. In my Ph.D. project, a transmission electron (TE) imaging system and secondary electron (SE) imaging system are successfully designed for the Delft MBSEM1.This thesis can be divided into two parts, the TE imaging system design and realization and the SE imaging system design and realization.

In the first part, the operational flexibility of the primary beams in the Delft MBSEM1 is analyzed without taking requirements for SE detection into consideration. The Delft MBSEM has a variable pitch of the primary beams on a sample, and the recommended pitch is smaller than 5μm, otherwise, the off-axis aberrations will spoil the uniformity. The Delft MBSEM1 can work at low landing energies (lower than 15keV) by biasing the sample stage negatively, with good optical performance. The result of this analysis helps to guide the TE imaging system design and experiments.

The TE imaging system in the Delft MBSEM1 uses fluorescent material and an optical microscope to enlarge the pitch of the TE signals. The thin sample is placed on top of the fluorescent material which converts electrons to photons. An optical microscope magnifies the pitch of TE signals by at least 40 times, so the TE signals are easily and separately collected in a detection plane. An additional set of electromagnetic lenses could also have been used to magnify the pith of TE signals. However,

this approach is not chosen considering the interference with the magnetic objective lens. The combination of a fast camera and an image processing program is used to record the intensities of each beam. This method avoids adding a de-scan system to the Delft MBSEM but has high requirement on the camera and the speed of the image processing program.

In the experiments, the TE image maps are obtained by using a calibration sample and biological tissues. Even the outermost beams still deliver quite even imaging quality. Details of 10-20 nm in images of the biological specimen are visible in the TE images.

Such results prove the working principle of the TE imaging design. There are still a few things needed to be done or improved in the future. The imaging resolution has not yet been measured quantitatively. A more advanced technology should replace the current solution for the image acquisition and processing. The intensity difference among sub-images and the stitching program need to be improved.

In the second part, firstly a SE detection strategy is designed for the Delft MBSEM. Its working principle is to use a set of electromagnetic lenses to focus the primary beams on the sample and to focus the SE beams in a detection plane simultaneously. The magnification of the SE focusing should be large so that the SE beams in the detection plane can be collected separately. The simulation result proves that the Delft MBSEM1 with such SE detection system can work in a range of working distance with variable pitch of the primary beams, but has difficulty to work in low landing energy cases.

An experimental setup is built to prove the working principle of this SE detection strategy. An assembly of YAG and fiber imaging conduit converts SEs to photons and transmits the SE signals out of the SEM column chamber. An optical system focuses the photons onto a camera. The camera and image processing program used in the TE imaging is employed to construct the SE images. In the experimental results, the typical SE images from our MBSEM were obtained using the calibration sample, and the first SE image map is presented. Such results prove the SE detection working principle. In the experiments, the imaging

resolution is worse than what we expect. The detection efficiency of the SE detection is too low to achieve high-throughput imaging. The crosstalk among the beams can be clearly seen in the image of the SE beams grid, but not in the SE images.

Both the TE imaging system and the SE imaging system are in the first phase of their development. Many things need to be optimized and improved in the Delft MBSEM1.

Fast real-time imaging should be realized in the TE and SE imaging systems. Now the scan dwell time used in the TE imaging and the SE imaging is 0.5 ms and 20 ms respectively. Our ultimate goal is to use 100 ns scan dwell time in the Delft MBSEM1 to achieve high-throughput imaging. So the image acquisition and image processing for one scan step should be finished in less than 100 ns. To meet the requirement, firstly the detection efficiency in these two systems, especially in the SE detection system, should be improved; secondly the combination of a camera and image processing should be fast. If the combination of a camera and image processing cannot process data this fast, a detector array and a de-scan system can be an alternative plan.

The imaging resolution needs to be improved and tested. The resolution measured in the experiments for the TE imaging and the SE imaging is larger than 10 nm, both worse than the simulated results. The alignment in the MBSEM system can be improved. The way to collect all SE beams in the SE detection system should be evaluated carefully to check whether it results in too large aberrations. The current orientations of two magnetic objective lenses (high-resolution lens and the ultra high-resolution lens) need to be set the same. A proper resolution test sample needs to be prepared, preferably having a few nanometer scale patterns on a fluorescent material.

The influence of the crosstalk among the beams needs to be evaluated. The evaluation may be based on a certain application. In the TE imaging system, the crosstalk will limit the minimum pitch of the primary beams on the sample. In the SE imaging system, the crosstalk needs to be analyzed to find whether it is mainly a result of the SE virtual source size or the aberrations generated in the SE focusing system. If it is mainly

from the SE virtual source size, the pitch of the primary beams on the sample should be increased; if it is mainly from the aberrations, the SE focusing system needs to be optimized.

A good stitching program and good control of the beam scan direction and scan FOV will be helpful in eliminating the intensity difference among sub-images and the sub-images' boundary in the image map.

The TE imaging system and the SE imaging system are designed for the Delft MBSEM, but in principle they can be used in any MBSEM after a little modification.

While this project was under development, in 2015 Zeiss released a commercially available MBSEM whose type is a single source single column. In its source unit, one beam is split into multiple beams (61 or 91) that are de-magnified using the macro magnetic lenses. It has a SE imaging system that allows the early customers to develop ways of working with multiple beams, to find more applications, and to give feedback on the benefits and shortcoming of the first generation MBSEM. The design principle of these two MBSEMs is compared in the thesis, but not the experimental results such as the imaging resolution and the detection efficiency. The imaging systems in the Delft MBSEM are still in the beginning development phase, and many factors can be optimized to improve the imaging properties. It is not the right timing to include the comparison of the imaging properties in this thesis.

Summary

The goal of this Ph.D. research is to develop imaging systems for the multiple beam scanning electron microscope (MBSEM) built in Delft University of Technology. This thesis includes two imaging systems, transmission electron (TE) imaging system, and secondary electron (SE) imaging system. The major conclusions, key results and some suggestions for future improvements are highlighted in this chapter.

Chapter 2 proves that the MBSEM can work for different pitches of the primary beams on the sample. As one pitch can be achieved by using various combinations of the lenses in the MBSEM, two ways are introduced to evaluate these combinations. One is to assess the current and the resolution. The other is to check the uniformity of the beams. We expected that the lens combination generating a big pitch would deliver the large resolution and the large current. However, it is only true when the pitch is smaller than 1 μm, due to the contribution of the axial aberrations and the off-axis aberrations. The uniformity of the beams can be achieved in a large pitch range with the compromise of the beam current. The combination of the lenses usually cannot satisfy both requirements at the same time. The pitch is preferable to be smaller than 5 μm in the Delft MBSEM1; otherwise, the off-axis aberrations would deteriorate the uniformity and/or the current of the beams.

The pitch control under different landing energies is also analyzed. The landing energy can be set freely in this MBSEM. When the landing energy is lower than 15 keV, it is preferred to bias the sample to achieve the target energy. The results in Chapter 2 help to guide the experiments done in chapter 3.

Chapter 3 presents the TE imaging system designed for the Delft MBSEM1 and the experimental results. In this imaging system, a piece of YAG disk is used to convert the 196 TE beams to 196 photon beams; an optical microscope with a high NA and good alignment with the electron optical axis is used inside the sample chamber to focus the 196 photon beams on to a camera with a large magnification. An offline image processing program is used to retrieve each beam's transmission signal and construct images.

In the experiments, the TE images from individual primary beams are obtained, using a calibration sample and biological tissues, and the TE image maps are presented. The beams, regardless of whether from the center or the edge of the e-beam grid, give quite an even imaging quality. The imaging resolution has not been measured because the proper resolution test sample needs to be prepared, preferably having a few nanometer scale patterns on a fluorescent material, but the details of 10-20nm in images of the biological specimen are visible in the TE images. Such results prove the working principle of this method.

The present throughput of the TE imaging system is low, approximately 20 min to finish images of one scan period with low scan resolution (200 × 200). Our second step of TE imaging system development is underway and should deliver relatively fast (a few thousand scan steps per second) real-time imaging. Our ultimate goal is to achieve rapid (100 ns scan dwell time) real-time imaging. Besides, the intensity difference among the beams should be corrected. Additionally, the crosstalk among neighboring beams, and the imaging properties, such as the image contrast and the detection quantum efficiency, should be studied in the future.

Chapter 4 proposes a SE detection system for the Delft MBSEM1. In this system, the sample is biased negatively to introduce a proper energy difference between the SE beams and the primary beams, such that it is possible to use the same lenses in the SEM column to achieve SE beams focusing in the variable aperture plane and primary beams focusing on the sample simultaneously. This detection system does not need much mechanical modification and keeps the whole MBSEM compact.

Theoretical analysis is done to prove the working principle. The results of one example show that the outermost primary beam has a spot size of 1.48 nm while the SE beams are separate with a pitch of 87 μm in the detection plane. The distribution of one SE beam has a sharp peak and long tail. The spot size is 20 μm using the full width of 10% maxima. The long tail causes crosstalk among the SE beams in the detection plane. The study of the virtual SE source size shows that the crosstalk initially happens among the virtual SE sources inside the sample and cannot be corrected in the SE focusing system. The high electrical field above the

sample is helpful to improve the collection efficiency and the crosstalk effect among the SE beams. Evaluation of the crosstalk effect in SE imaging is not implemented but needs to be done in the future. If zero crosstalk or 100% collection efficiency are required, we may need to design a new version of MBSEM to have a large pitch of the primary beam on the sample.

The SE imaging system in the Delft MBSEM1 has limited flexibility. It has difficulty to use low landing energies. This limitation originates from the requirement that the same lenses need to focus the primary beams and the SE beams simultaneously in the SEM column.

Chapter 5 describes the experimental setup built to test the working principle of the SE imaging system in the Delft MBSEM1 and presents the first experimental results. A piece of YAG disk is used to convert the SE to photons, and an optical fiber imaging conduit guides the photons to a camera. An optical system is used to record the 196 SE beams, and an off-line processing program acquires their intensities and constructs SE images. The TE imaging setup is used to help to get the SE focusing quickly.

In the experimental results, the primary beams are focused well on the sample, and the SE beams are focused and separated on the YAG simultaneously. The typical SE images from our MBSEM were obtained using the calibration sample, and the first SE image map is presented. Such results prove the SE detection working principle.

However, the detection efficiency of the SE imaging system is low and needs to be improved. Now the scan dwell time is set to be 20 ms, too slow to do high throughput imaging in the Delft MBSEM1. The detection chain, including the fluorescent material, the imaging conduit, the optical system and the camera, needs to be optimized. The SE imaging resolution should be improved when all the SE beams land on the detector by modification of the detector or the implementation of a Wien filter in the column. The crosstalk among the beams exists in the SE grids in the detection plane. It can be reduced by applying a strong electrical field above the sample to reduce the SE virtual source size in the sample and

optimizing the SE focusing on minimizing the aberrations. Its influence on the SE images needs to be evaluated in the future.

In the experiment, it is found that the current orientations of two magnetic objective lenses (high-resolution lens and the ultra high-resolution lens) are different. I assumed that they were the same in the simulation. The current orientation difference makes that the simulation results do not match well with the experimental results (including the TE and SE imaging results). In the future, it is better to make the current orientations of these two lenses the same.

To conclude, this thesis discusses the control of the primary beams' pitch on the sample and the landing energy in Chapter 2, introduces the SE detection system in chapter 4, and proves the working principles of the TE imaging system and SE imaging system via the experiments in Chapter 3 and Chapter 5. As the TE imaging system and SE imaging system are both in the first phase of their development, many things need to be optimized and improved. Once they are done, the Delft MBSEM1 will deliver high-throughput and high-resolution TE and SE imaging.

Samenvatting

Het doel van dit promotieonderzoek is het ontwikkelen van een beeldvormingssysteem voor de multi-bundel raster scanning elektronen microscoop (MBSEM) ontwikkeld binnen de Technische universiteit Delft. In deze scriptie worden twee beeldvormingsystemen besproken, gebruikmakend van transmissie elektronen (TE) en secondaire elektronen (SE) detectie. De voornaamste conclusies, resultaten en suggesties voor doorontwikkeling worden in dit hoofdstuk besproken.

In hoofdstuk 2 wordt aangetoond dat de MBSEM werkt voor verschillende bundel afstanden van de primaire elektronen bundels op het preparaat. Omdat deze afstand kan worden gerealiseerd met verschillende lens excitaties, worden twee methodes geïntroduceerd om dit te analyseren. Een methode is om de stroom en resolutie te bepalen, de ander om de uniformiteit van de bundels te evalueren. De verwachting is dat de lenscombinatie die de grootste bundel afstand creëert, ook de combinatie is waarbij de stroom in elke bundel het grootst is en de resolutie het slechts. Uniformiteit in de resolutie kan alleen worden gehaald bij een hoge stroom als de bundel afstand kleiner is dan 1µm, wat wordt veroorzaakt door elektron optische aberraties. Uniformiteit kan ook behaald worden bij grotere bundelafstand maar hierbij wordt stroom opgeofferd. De combinatie van lenzen staat over het algemeen niet toe dat er een goede resolutie, hoge stroom, uniformiteit en grote bundelafstand tegelijkertijd is. In de MBSEM gaat de voorkeur uit naar een bundel afstand van beneden de 5 µm, anders wordt de uniformiteit of stroom van de bundels te veel aangetast door de “off-axis” aberraties.

De bediening van de bundel afstand voor verschillende versnelspanningen is ook geanalyseerd in het hoofdstuk. De landingsenergie kan vrij gekozen worden in de MBSEM maar wanneer deze lager wordt dan 15keV wordt het afremmen van de elektronen door het preparaat onder spanning te zetten, verkozen. De resultaten in hoofdstuk 2 hebben geholpen de experimenten in hoofdstuk 3 uit te voeren.

Hoofdstuk 3 introduceert de transmissie elektronen detectie ontworpen voor de MBSEM en een aantal experimentele resultaten. In dit

beeldvormingssysteem wordt een YAG:CE kristal gebruikt om de 196 TE bundels te converteren naar 196 lichtbundels. Een objectief lens met een hoog numeriek apertuur en een goede uitlijning met de elektron-optische as in de preparaat kamer wordt gebruikt om de 196 lichtbundels met een grote vergroting op een camera af te beelden. Een offline beeldverwerkings programma wordt gebruikt om van elke bundel het transmissie signaal te meten en te verwerken tot een beeld.

Er worden experimentele resultaten getoond met van een kalibratie preparaat en biologisch weefsel verkregen beelden. Dit zijn beelden verkregen met enkele bundels en samengestelde beelden. De bundels geven een uniforme beeldkwaliteit onafhankelijk van de positie in het elektronbundel rooster. De uiteindelijk verkregen resolutie is niet gemeten door de afwezigheid van een preparaat met structuren op de nanometer schaal, geschikt voor het meten van de kleinste resoluties. In de biologische preparaten waren echter details tussen 10nm en 20nm zichtbaar met het transmissie beeldvormingssysteem. Deze resultaten laten de achterliggende principes van deze methode duidelijk zien.

De huidige snelheid waarmee een beeld verkregen kan worden in de transmissie modus is vrij laag, er is ongeveer 20 minuten nodig om een beeld met een lage scan resolutie te verkrijgen (200x200). De volgende stap in de ontwikkeling van het transmissie beeldvormingssysteem nadert de eindfase, waarbij het mogelijk is om snel een "real-time" beeld te vormen (een camera met een paar duizend beelden per seconde) .Het uiteindelijke doel is het behalen van een integratietijd van 100ns. Daarnaast moet ook het intensiteitsverschil tussen de bundels worden verholpen. Om een volledig beeld te krijgen moet ook de kruisspraak, het contrast, de signaal-ruis verhouding en kwantum efficiëntie in de toekomst worden onderzocht.

In hoofdstuk 4 wordt een beeldvormingssysteem met secondaire elektronen gepresenteerd. In dit systeem wordt er een negatief potentiaal op het preparaat gezet wat er voor zorgt dat het energie verschil tussen de primaire elektron bundels en de secondaire elektron bundels zodanig is dat ze tegelijkertijd gefocust kunnen worden. De primaire bundel is zoals gewoonlijk gefocust op het preparaat en de secondaire bundels op een YAG:CE scherm ter hoogte van het variabel apertuur. Deze detectie

modus heeft weinig mechanische aanpassingen nodig aan de kolom en houdt de MBSEM compact.

Om een het principe van deze methode aan te tonen is een theoretische analyse uitgevoerd. In een voorbeeld wordt een spot grootte van 1.48nm van de primaire bundels en een bundel afstand van 87µm van de secondaire bundels op de detector aangetoond. De grootte van de spots op de secondaire electron detector is 20µm als de breedte van 10% van het maximum wordt aangenomen, met lange staarten, wat kruisspraak tussen de bundels veroorzaken. Door naar de virtuele bron grootte van de secondaire elektronen te onderzoeken wordt geconcludeerd dat de kruisspraak reeds gebeurt in het preparaat en niet gecorrigeerd kan worden in het focus systeem. Het hoge elektrisch veld boven het preparaat helpt het verkleinen van de kruisspraak en het vergroten van de detectie efficiëntie. Het onderzoeken van de kruisspraak effecten moet nog in de toekomst onderzocht worden. Om een hoge detectie efficiëntie (richting 100%) te krijgen en kruisspraak te voorkomen dient de MBSEM opnieuw ontworpen te worden met een grotere afstand tussen de primaire bundels.

Het secondaire elektronen beeldvormingssysteem in de MBSEM is gelimiteerd in flexibiliteit doordat het lastig is lage landingsenergieën te gebruiken. Deze limitatie wordt veroorzaakt doordat voor het focussen de primaire en secondaire elektronen, dezelfde lenzen worden gebruikt.

Hoofdstuk 5 beschrijft de experimentele opstelling die is gebouwd om het principe van SE detectie aan te tonen. Een YAG:CE kristal schijfje wordt gebruikt om de secondaire elektronen om te zetten naar fotonen. Deze worden dan door middel van een optische fiber naar een camera geleid. Een optisch systeem detecteert het licht van de 196 bundels en het beeld wordt offline gecreëerd door een verwerkingsprogramma. Tegelijkertijd wordt de transmissie detectie gebruikt om snel gefocuste bundel te vormen.

De resultaten van uitgevoerde experimenten laten zien dat er tegelijkertijd goed gefocuste bundels op het preparaat zijn en goed gefocuste en gescheiden bundels op de secondaire elektron detector. De typische SE

beelden worden getoond welke zijn verkregen van een kalibratie preparaat. Deze resultaten bewijzen het SE detectie principe.

De detectie efficiëntie van de SE detectie is echter laag en deze dient hoger gemaakt te worden. Op dit moment is de integratietijd van deze modus 20ms, wat te laag is voor praktische toepassing van de MBSEM. De detectie keten van het YAG:CE scherm, de optische fiber en het beeldvormingssysteem dienen verbeterd te worden om dit te versnellen. De resolutie verkregen me de SE detectie moet verbeterd worden door het aanpassen van de detector of het implementeren van den een Wien filter in de kolom. Er bestaat wel kruisspraak tussen de bundels in op de detector. Deze kruisspraak kan worden verminderd door een sterk elektrisch veld tussen het preparaat en de poolvoet van de MBSEM, waardoor de SE virtuele brongrootte wordt verkleind. Daarnaast kan ook het focussen van de SE bundels verbeterd worden door aberraties te verminderen. De invloed van deze zaken moet beter worden onderzocht in de toekomst.

Doordat stroom richting in de twee magnetische objectief lenzen verschilt en ik aannam dat ze dat de dezelfde richting hebben, kwamen de simulaties niet overeen met de experimentele resultaten. In de toekomst is het beter om de richting van de stroom in beide lenzen gelijk te maken.

Ter conclusie, in hoofdstuk twee van deze scriptie wordt de landingsenergie en de controle van de primaire bundels en de bundel afstand op het preparaat besproken. In hoofdstuk 3 wordt het principe van de TE detectie getoond, in hoofdstuk 4 wordt de SE detectie getoond en bewezen door experimenten in hoofdstuk 5. Omdat de TE en SE beeldvormingssystemen zich nog in de eerste fase van ontwikkeling bevinden, moet er nog veel verbeterd worden. Als dit geslaagd is, zal de Delft MBSEM1 een hoge doorvoersnelheid en hoge resolutie met TE en SE detectie mogelijk maken.

Acknowledgements

It was my great honor to work in the charged particle group for years. Here I have many people to give my acknowledgment.

I would like to start from my promoter, Prof. Pieter Kruit. Thank you for bringing me back to electron optics and electron microscopy in 2011. In theses year, I benefited a lot from every discussion with you, and every lecture from you. You have such good insight into science, and such magic power to turn the complex to the simple. You guide me through the research with great patience and enthusiasm. I really enjoy doing research under your supervision.

I should give my sincere thanks to Kees and Jacob for mentorship. You not only help me to solve scientific problems but also my personal issues. Anjella, thank you for always helping me out.

Jan, Alix, and Ruud, thank you for helping me to solve the mechanical challenge. Frans, Han and Paul Keijzer, you are the people I turned to when I have problems with the electronics and software. Carel, you make me worry nothing on the MEMS manufacture. Without all your help, my project cannot achieve so many results!

It was my honor to know and work with fellow researchers in the CPO group. Ali, it is my pleasure to work as your successor. Your advice saved me quite a lot of time on my work and my job hunting. Christiaan, you are a talented electron optical scientist. I like the way that you do everything full of confidence. Nalan and Angela, thanks for your concern when I encountered challenges in my experiments. Takashi told me you were worried about me. I felt very lucky to be in the same group with you! Sangeetha, definitely, you are the best badminton player in our group! Marijke, you are a marathon runner, a marathon runner, a marathon runner! I need to repeat three times to show how I admire you. Thomas, I never thought that a gym coach could turn to be a Ph.D. You are special! Gerward, I will never forget the time we played badminton together and your help to us no matter when we asked for it. Takashi, I never forget that we drove to Berlin, sleeping in the car for two days. I know whom I should contact if I go to Japan. Leon, I am so amazed that

you are a guitarist in a band. Robert, thanks for sharing your life with us. You are a trustworthy friend. Wilco, as my successor in this project, thanks for helping me translate my summary chapter and my propositions. Good luck for your Ph.D. life! Additionally, I need to give my thanks to Ben, David, who helped me to have an easy start in the CPO group; my thanks to Lennard, Josey, Shammi, Maurice, Gaudhaman, Aditi, and Conny. It was my pleasure to work with you.

Jianfei and Shaoying, Zhenpei and Dan, Changlin and Honglin, Eric and Xin, Kai and Ming, Zhang Li, Wenbo, and many others, I cannot forget so many happy times that we had dinner together, BBQ together, and celebrated New Year together. You made my life in Delft more colorful and joyful. You are priceless!

Heartfelt thanks go to my wife, Ting. You always support and trust me, telling me that I am the best every moment when I feel down. After the birth of our daughter Eileen Jiayu(Niuniu), you stopped working for one and half years to take care of the family. You are my soul mate!

Niuniu, you brought me enormous happiness. You are my angel!

Last but not the least, I would like to express my deepest gratitude to my parents and my parents-in-law for all their love and support in my life.

Curriculum Vitae

Yan Ren, was born in July 1981, Qinyang, Henan province, China. Yan received his Bachelor degree on electronics from Xi'an Jiaotong University in July 2003, and obtained his Master degree on Physical electronics from Xi'an Jiaotong University in June 2006. From July 2006 to September 2010, Yan worked in Hermes Microvision Inc. (HMI, now acquired by ASML), focusing on the design and manufacture of the electron optical column. From September 2010 to May 2011, Yan was a consultant in CPC Pinnacle Consulting Co., working on data analysis and information extraction. In September 2011, Yan started his Ph.D. project in Charged Particle Optics group, TU Delft, the Netherlands. His Ph.D. project was to design transmission electron and secondary electron imaging systems for the Delft Multi-Beam Scanning Electron Microscope 1.